NUMERICAL MODELS FOR SCOUR AND LIQUEFACTION AROUND OBJECT UNDER CURRENTS AND WAVES

BY

XIAOFENG LIU

B.Eng., Tsinghua University, 2000
M.Eng., Peking University, 2003
M.S., University of Illinois at Urbana-Champaign, 2007

DISSERTATION

Submitted in partial fulfillment of the requirements
for the degree of Doctor of Philosophy in Civil Engineering
in the Graduate College of the
University of Illinois at Urbana-Champaign, 2008

Urbana, Illinois

Doctoral Committee:

Professor Marcelo H. García, Chair
Professor Gary Parker
Professor Albert Valocchi
Associate Professor Arif Masud
Dr. Robert R. Holmes, Jr., USGS Illinois Water Science Center

Abstract

Local scour and liquefaction are two of the most important processes which affect the interactions between fluid, object and sediment when an object (such as bridge pier, offshore foundation, etc.) is exposed to currents and waves. In the present study, numerical models are developed to understand these complicated processes.

For the local scour process, two-dimensional and three-dimensional models are developed respectively. In the two-dimensional model, shallow water equations with finite volume method on unstructured mesh are used. The two-dimensional model uses the Godunov scheme and approximate Riemann solvers. Hydrodynamics and sediment transport equations are coupled and solved simultaneously. Asymptotic analysis of the system eigenvalues is given and the approximation is compared with the numerical results. The model developed in this thesis can deal with wetting and drying automatically. Discontinuity of the flow, such as a hydraulic jump, can be captured. For the three dimensional model, free water surface and automatic mesh deformation for the bed are incorporated in the model. The Reynolds Averaged Navier-Stokes (RANS) turbulence model is used to simulate the turbulent flow field. The turbulence model used is k- ϵ Model. Two interfaces (water and air, water and sediment) present in the domain are captured with different approaches. The free surface of the flow is captured by Volume of Fluid (VOF) scheme which is an Eulerian approach. A new method for the VOF scheme is proposed to reduce the computational time while retaining relatively good accuracy. The water-sediment interface (bed) is captured with a moving mesh method which is a Lagrangian approach. Unlike the two-dimensional model, the flow field is coupled with sediment transport (both bed load and suspended load) using a quasi-steady approach. Numerical simulations are carried out and compared with experimental results. Good

results are obtained with the proposed model. The flow field compares well with the experimental observations. Scour patterns are similar to the experimental data. Long computational time is needed for morphological simulation and parallel computation is used to accelerate this process. Three-dimensional model can capture the detailed flow structure around an object and predict the scour process more accurately. However, the two-dimensional model can be used as a fast assessment tool for large computational domains.

For the liquefaction process, two different mechanisms (momentary and residual) are considered. For momentary liquefaction, a three-dimensional numerical model for the sea bed response under free surface water waves is constructed. Free water surface is modeled by volume of fluid (VOF) method and water waves are generated by numerical wave-maker boundary condition. An iterative numerical scheme is proposed to solve the Biot consolidation equation using a finite volume method (FVM). The coupling between water wave and sea bed is through both pressure and stress conditions on common boundaries. For residual liquefaction, the solutions to the one-dimensional model equation of the period-averaged pore pressure buildup are listed. The accumulation of pore pressure is modeled as the effect of the source term in the storage equation. Corrections to the solutions in the literature are provided. For deep soil condition, an asymptotic solution is proposed to estimate the pore pressure. A numerical model is also developed to solve the one-dimensional period-averaged pore pressure buildup equation. Good agreement between the results of numerical model and analytical model are found. These results also agree with the experiment data. A tentative step is also made to model the phase-resolved pore pressure. The basic idea of adding a source term to the governing equation is explored. The source term has the same form as that of the period-averaged residual pore pressure model. Test case shows that this model gives good results comparing to the one-dimensional period-averaged model.

To My Family.

Acknowledgments

This thesis would not have been possible without the support of many people. Firstly, I would like to thank my advisor Professor Marcelo H. Gracía for his support and valuable advices. Throughout my doctoral work, he continually encouraged me to develop independent research skills. Special thanks to the exceptional committee, Professors Gary Parker, Albert J. Valocchi, Arif Masud and Robert R. Holmes Jr., who provided valuable suggestions regarding the topic of this dissertation. Also, I extend many thanks to my colleagues and friends, especially Michael (Xuejun) Yang, Jorge Abad, Javier Ancalle, Mariano I. Cantero, Robert Haydel, Blake Landry, Arturo S. Leoń, Francisco Pedocchi and Octavio Sequeiros. I am grateful to Andy Waratuke for helping me with lab issues. Finally, thanks to my family for their constant support and love; without them, it would be very difficult to complete this thesis.

This research was funded by the Coastal Geosciences Program of the U.S. Office of Naval Research through the Grants N00014-01-1-0337. Supercomputer time was provided by the National Center for Supercomputing Applications (NCSA) at UIUC. This support is gratefully acknowledged.

Table of Contents

List of Tables

List of Figures

List of Abbreviations

CFD	Computational Fluid Dynamics.
CICSAM	Compressive Interface Capturing Scheme for Arbitrary Meshes.
FVM	Finite Volume Method.
FEM	Finite Element Method.
LSM	Level Set Method.
MAC	Marker and Cell.
NCSA	National Center for Supercomputing Applications.
PDE	Partial Differential Equation.
RANS	Reynolds Averaged Navier-Stokes.
SIMPLE	Semi-Implicit Method of Pressure Linked Equation.
SWE	Shallow Water Equation.
TVD	Total Variation Diminishing.
PISO	Pressure Implicit Splitting of Operators.
VOF	Volume of Fluid.

List of Symbols

A coefficient in Grass sediment transport formula.

c_{b*} equilibrium sediment concentration at bed.

c_ν coefficient of consolidation.

$C_\mu, C_1, C_2, \sigma_k, \sigma_\epsilon$ coefficients for turbulence model.

d sediment grain diameter; soil depth.

D, E sediment deposition rate and erosion rate.

D_* particle size parameter.

f Coriolis parameter; source term for residual liquefaction equation.

f_r ramp function for wave generation.

F_r Froude number.

F_{lift}, F_{drag} lift and drag forces

$\mathbf{g}, g$ gravity vector, gravity constant.

G shear modulus

h bed elevation; total water depth.

h_s still water elevation.

k turbulence kinetic energy; wave number.

K surface curvature; soil permeability coefficient.

K_C Keulegan-Carpenter number.

K' bulk modulus of elasticity of water.

L wave length.

m	coefficient in Grass sediment transport formula.
M	transformation matrix.
n	sand porosity.
$\vec{n}$	bed surface normal vector.
N, N_l	number of cyclic loading, number of cycles to liquefaction.
p	pressure.
p_0	wave-induced pressure in the soil.
p_b	wave pressure amplitude.
$\overline{p}$	period-averaged pore pressure.
P	dimensionless pore pressure.
q^*	dimensionless bed load transport rate.
q_0, q_i	dimensional bed load transport flux, dimensional bed load transport flux component.
q_{sx}, q_{sy}	sediment transport flux in x and y directions.
R	specific gravity of sediment.
S	surface of the domain of interest.
$\mathbf{S}$	strain rate tensor.
$\vec{S}$	steepest slope.
S_{ox}, S_{oy}	friction coefficients in x and y directions
t	time.
T	motion period or wave period.
u, v	depth-averaged velocity in x and y directions.
$\mathbf{u}$	fluid velocity vector.
$\mathbf{v}$	mesh motion velocity; soil skeleton displacement vector.
v_s	sediment fall velocity.
x, y, z	Cartesian coordinates.
$\mathbf{x}^k$	grid point position at time step k.
α	fluid volume fraction.

γ mesh motion diffusion coefficient; specific weight of water.

Δ discriminant.

ϵ turbulence energy dissipation rate; small perturbation parameter.

ϵ_0 sand porosity.

θ, θ_c Shields number, critical Shields number.

$\lambda, \tilde{\lambda}$ dimensional and dimensionless wave speed

μ, μ_t fluid dynamic viscosity, turbulence viscosity.

ν Poisson ratio.

ξ free surface elevation above the still water.

ρ, ρ_1, ρ_2 mixture density, fluid density, air density.

σ surface tension coefficient; stress tensor.

$\sigma_0^{'}$ initial soil effective stress.

τ_0 wave-induced shear stress in the soil.

τ_b, τ_i bed shear stress, bed shear stress component.

ϕ internal friction angle of sediment.

Φ wave phase.

ψ nondimensional excess bed shear stress.

ω wave frequency.

Ω domain of interest.

Chapter 1

Introduction

1.1 Motivations

When an object (bridge pier, offshore structure foundation, sea mine etc.) is placed in the river or in the ocean, the flow field will be affected, and the capacity of water for carrying sediment will also be changed (see Figure 1.1). One or more of the following will happen (Sumer and Fredsøe 2002): contraction of flow, vortices formed in the front of or in the lee-wake of the object, turbulence generation, reflection and diffraction of waves, wave breaking, and high pressure gradient in the adjacent sediment. These will cause scour around the object, and sometimes it will make the structure fail. It is important for engineers to understand the process of scour and to make better designs to prevent or mitigate the damage. Scour around objects in rivers and oceans has been a continuous research interest because of its importance (Breusers et al. 1977; Breusers and Raudkivi 1991; Dey 1997; Melville 1997; Melville and Sutherland 1988; Melville and Coleman 2000; Raudkivi 1986). It is still an open subject since many problems have not yet been solved. These problems include the free surface effect on the scour process, changing the computational mesh when the bed is deformed, etc. New numerical techniques and improved models should be used to improve our understanding of scour problem.

Another important fact which is closely related to scour is liquefaction. Figure 1.2 shows an experiment done in the Ven Te Chow Hydrosystems Laboratory at the University of Illinois at Urbana and Champaign where a short cylinder sunk into the sediment when liquefaction took place (Cataño-Lopera 2005). The figure also shows the sediment movement and scour around the object. Liquefaction could be due to earthquake or wave action (ocean storm). Much experimental work

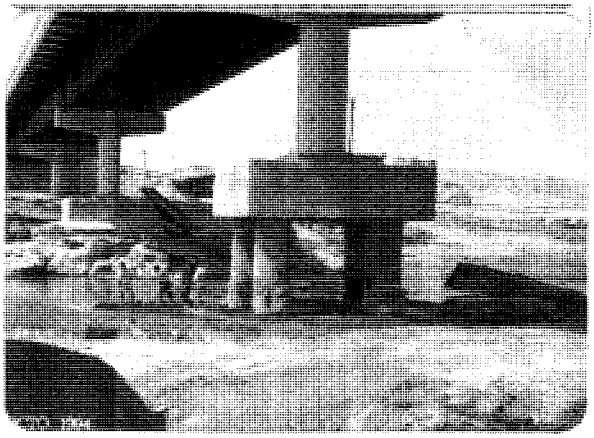

(a)

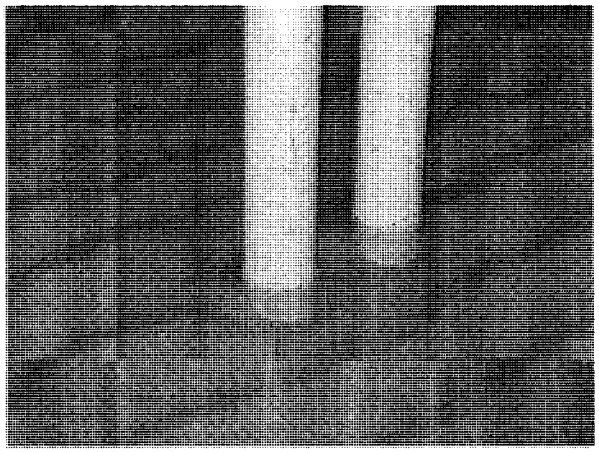

(b)

Figure 1.1: Scour around Piles: (a) Bridge Pier (www.ifh.uni-karlsruhe.de) (b) Scour Experiment in Hydrosystems Laboratory, University of Illinois

has been done (Sakai et al. 1994; Sumer et al. 1999), and numerical models have been developed (Magda 1996; Jeng and Lin 1999; Gao et al. 2003) to understand this complicated process. There are also many analytical models which describe the sea bed response and give fairly good results (Yamamoto 1977; Mei and Foda 1981; Jeng and Hsu 1996; Yuhi and Ishida 2002). Although there exists many numerical models on sea bed response under waves, most of them simply estimate wave pressure distribution on the water-bed interface using wave theory. This is true if there are only water waves and sea bed interactions. However, for the case when there are extra objects in the system (such as pile, semi-buried foundation, etc.), the water flow around the object will be highly three-dimensional, therefore making it difficult to get an analytical solution from wave theory. With the use of computational fluid dynamics (CFD), the flow field can be solved and used as an input for the numerical modeling of liquefaction.

Other mechanisms, as pointed out in Bennett and Dolan (2001), such as impact penetration, gravity settlement, bedform migration, shakedown, sliding, even biological activity will also have important effects on the interactions between object, fluid and sea bed. These mechanisms are not completely understood (Cataño-Lopera 2005). They are closely related and affect each other. The whole process is governed by the joint action of all these mechanisms even though some of them might be dominant. In this research, only scour and liquefaction will be investigated.

1.2 Objectives of This Research

The main goal of this research is to use numerical models to predict the effect of scour and liquefaction around objects.

For the scour process, two-dimensional and three-dimensional models are developed respectively to predict scour under different temporal and spatial scales. The 2D model will utilize the Godunov scheme and approximate Riemann solvers. Other depth-averaged 2D numerical models in the literature for sediment transport and river morphology have obtained good results with this approach, for example Duan and Nanda (2006) and Wu (2004) among many others. These models

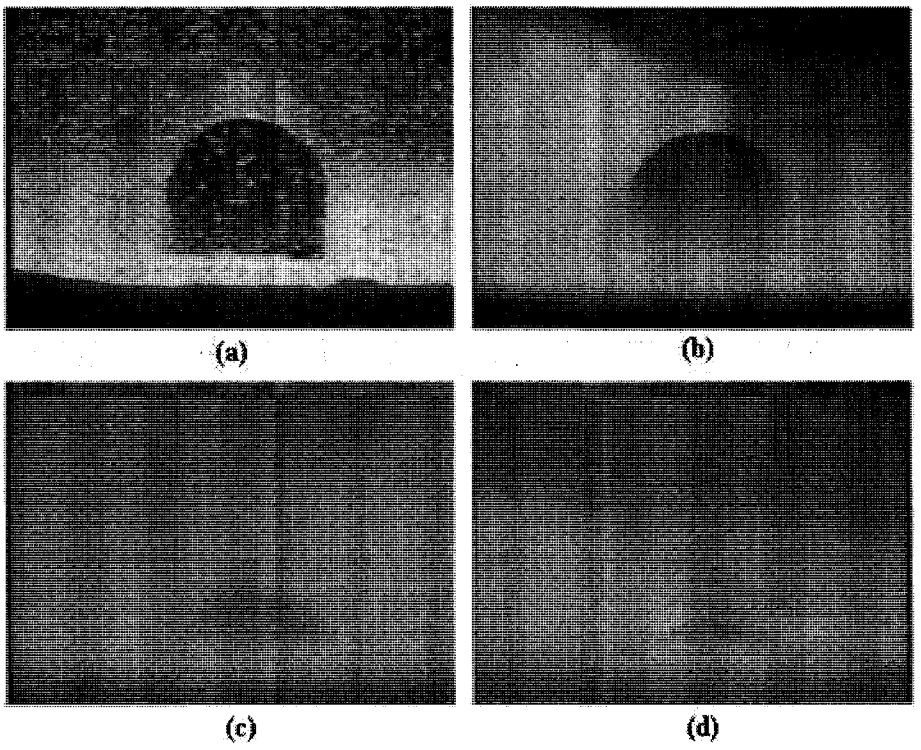

Figure 1.2: Scour and Liquefaction Effect around a Cylinder Sitting on the Bed

usually assume that the time scale of sediment transport is much larger than that of the flow field. Based on this assumption, the quasi-steady approach is used most of the time. However, this assumption is not always true when the bed morphological change is fast. In this thesis, a coupled two-dimensional model for both hydrodynamics and sediment transport will be developed. Also, the computational domain for a real world case is complicated, and an unstructured mesh is necessary. Numerical calculation of the system wave speeds when using unstructured mesh is slow and inefficient. Asymptotic expansion is used to estimate such wave speeds. The model developed in this research can deal with wetting and drying automatically. Discontinuity of the flow can be captured. In the 3D model, since there are at least three phases (water, object and sediment), the interfaces between these phases need to be captured. Although different interface capturing methods can be used, each interface has its own characteristics and appropriate methods should be chosen for each of them. For the free water surface, an Eulerian approach is used while for the bed interface, a Lagrangian approach is chosen. To take into account the deformation of the fluid domain, a mesh deformation method should be used to smoothly move each grid point in the domain.

For the liquefaction process, two different mechanisms (momentary and residual) will be considered. For momentary liquefaction, a three-dimensional numerical model for the sea bed response under free surface water waves will be developed. Free surface is modeled by the volume of fluid (VOF) method, and water waves are generated by numerical wave maker boundary condition. An iterative numerical scheme is proposed to solve the Biot consolidation equation using the finite volume method (FVM). The coupling between water wave and sea bed is through pressure and stress condition on common boundaries. For residual liquefaction, the solutions to the one-dimensional model equation of the period-averaged pore pressure buildup are listed. A source term is added to the storage equation to model the pore pressure buildup. Corrections to the solutions available in the literature are provided. For deep soil, an asymptotic solution is proposed to estimate the pore pressure. In addition, a tentative step is made to model the phase-resolved residual pore pressure.

The numerical models developed in this study can be used in engineering practice as a tool to guide the design, construction, and operation of structures in rivers and oceans. These models can also be used as a research tool to further understand the complete mechanisms of scour and liquefaction.

1.3 Methodology

This study is mainly based on numerical models. For scour problem, two-dimensional and three-dimensional numerical models are developed to simulate the flow field and sediment transport processes. Both codes are based on the finite volume method. The two-dimensional code solves the shallow water equations on unstructured meshes. It is suitable for large scale and long term simulations. This is an in-house research code developed in the Ven Te Chow Hydrosystems Laboratory at UIUC. The three-dimensional code is developed on the platform of an open source computational fluid dynamics (CFD) code named OpenFOAM (OpenCFD 2006). The fluid flow solver is adapted from the original turbulence flow solver and a sediment transport solver is added to it. For liquefaction potential simulation, the numerical model is also based on OpenFOAM since it provides a platform for the numerical solution of partial differential equations. Coupled solver of free surface flow and consolidation is developed to simulate the sea bed response under waves. Numerical test cases are selected from the literature for the purpose of validation and testing of the capabilities of the model.

Most of the simulations are done in the supercomputers in National Center for Supercomputing Applications (NCSA) at University of Illinois at Urbana and Champaign. Parallel computations are used (especially the three dimensional model of scour and liquefaction) extensively to reduce the required computer time.

1.4 Outline of the Dissertation

In chapter 2, the two-dimensional numerical model for scour is introduced. The finite volume method solver for the non-linear shallow water equations is described. Two-dimensional Riemann problem approximate solvers used in the code are briefly described. Numerical simulations of scour problems in a large domain and for long evolution time are carried out. In Chapter 3, the three-dimensional scour model with free water surface and automatic mesh deformation is elaborated. Free surface capturing methods and bed surface resolving methods are described. A novel mesh deformation method is used to automatically move the mesh for the scour problem. Discussions on the merits and shortcomings of different interface capturing methods are given at the end of the chapter. Chapter 4 describes the three-dimensional, coupled model for the liquefaction evaluation. Fluid field solver is similar to that of three-dimensional scour model while consolidation solver is written based on the new iterative algorithm using finite volume method. Chapter 5 introduces the one-dimensional period-averaged residual pore water buildup model. Corrected solutions and a new asymptotic estimation for deep sediment deposits are given. Numerical model is also developed for the period-averaged pore pressure. A tentative step is made to model the phase-resolved pore pressure numerically. Chapter 6 is a summary of the thesis findings. In the appendixes, the derivations of some of the equations used in this thesis are given.

Chapter 2

Two Dimensional Model for Scour Around Object Using Shallow Water Equations on Unstructured Mesh

2.1 Introduction

Scour due to sediment transport has been one of the most important engineering problems because it will endanger the stability of structures such as bridges (Sumer and Fredsøe 2002). Many two-dimensional and three-dimensional numerical models have been developed to simulate the scour process (Beek and Wind 1990; Olsen and Melaaen 1993; 1999; Brørs 1999; Li and Cheng 2001; Neyshabouri et al. 2003; Duc et al. 2004; Wu 2004; Roulund et al. 2005; Duan and Nanda 2006). While three-dimensional models can give more detailed information on the flow and turbulence structure, they require considerable computational efforts (Liu and García 2006a). Two-dimensional models can give quick assessment of the scour pattern and relatively accurate maximum scour depth. The fast evaluation of these scour parameters are important for the design, construction and operation of hydraulic structures. It is of critical importance in the case of scour due to dam failure or dike break flow. In this paper, a two-dimensional model coupling hydrodynamic and scour processes will be developed.

The hydrodynamic component of many two-dimensional models is the depth averaged shallow water equations (SWEs) in which the hydrostatic assumption is implied. Higher order finite volume methods on unstructured triangular grids for shallow water equations have been developed and have achieved high accuracy (Anastasiou and Chan 1997; Yoon and Kang 2004). The unstruc-

*This chapter, as a manuscript, is under review for possible publication in Coastal Engineering

tured mesh makes the application of SWEs for complex geometries easier. However, the treatment of the pressure and bed-slope terms should be compatible with other terms in the equations when discretizing on an unstructured mesh (Farshi and Komaei 2005). Special care should be taken to make the scheme compatible and conservative. Otherwise, non-physical results will be observed after several time steps (Nujić 1995).

For finite volume methods (FVM) solving shallow water equations, one of the most important properties is called the C-property which describes the stationary state when the flux gradients balance the slope source term (Bermudez and Vazquez 1994). LeVeque (1998) developed a wave-propagation algorithm by solving the Riemann problem at the cell center and canceling the source term with the flux difference exactly. Another important contribution in dealing with this problem is the surface gradient method (SGM) (Zhou et al. 2001; 2002). The basic assumption is that the water surface is smoother than the bottom. Instead of conservative variables, the surface gradient method uses the water surface level to reconstruct the Riemman states at the cell interfaces. Rogers et al. (2003) proposed a novel method which reformulates the conservation laws in terms of the deviations from equilibrium. This mathematical reformulation introduces extra physical information and avoids the conventional numerical treatment of the imbalance. Another method of equation reformulation is to rewrite the bed slope term in divergence form. An exact balance between flux gradient and source term is achieved when both terms are discretized by compatible schemes (Valiani and Begnudelli 2006; Liu and García 2007b). For the hyperbolic system which is expanded by adding sediment transport equation in this chapter, the divergence form is not suitable for the source term.

Godunov scheme with an appropriate Riemann solver can capture the steep water surface elevation gradient even discontinuities. For the coupled system of hydrodynamics and sediment transport, it can be used where a dramatic water surface change occurs, e.g. scour due to dam break flow and strong transient flow. Based on the hyperbolic nature of the coupled system, DeVriend (1987a) and DeVriend (1987b) analyzed the waves and their interactions, although the analysis was on the system of primitive variables. Since then, the coupled system of shallow water

and bed sediment conservation equations has been studied by many researchers. Lyn (1987) and Lyn and Altinakar (2002) identified the different scales of the one-dimensional system and gave the asymptotic approximation of the wave speeds in different flow regimes. For one-dimensional system under some simplifications, the wave speeds can be expressed explicitly (Hudson and Sweby 2003; Hudson et al. 2005). On a structured mesh, the waves associated with the two-dimensional system can also be analyzed by splitting the system into different directions (Hudson and Sweby 2005). On a unstructured mesh, the equation system is more complicated and difficult to analyze. This is one of the problems which will be dealt with in this paper.

There is still a debate on the characteristic of the coupled system of SWEs and sediment conservation equation (i.e., Exner's equation). Cao et al. (2002) emphasized on the hyperbolicity of the coupled system while Cui et al. (2005) argued that the evolution of the sediment waves can be dominated by dispersion. Different interpretation of the equations is most often due to the different flow regimes. In different regimes, the dominant terms in the governing equations will change. Cui and Parker (1997) did some linear stability analysis and found the conditions for the dispersive domination are that the Froude number should not be too far from unity, the sediment transport rate should be low, and the wavelength of the bed forms should be long. In the author's opinion, the question of which term is dominant is only relevant for analysis. Since for a numerical model all the terms are included, the nature of the coupled system will reveal itself through the simulation results.

In this chapter, the hydrodynamics and sediment transport are coupled and solved together in one step. Special treatment of the source term on unstructured grid will make the scheme stable and physically balanced (conserving both mass and momentum). The methodology of expanding the SWEs with sediment transport can also be used to expand the system with other equations (such as scalar transportation). Asymptotic analysis of the system eigenvalues will be given and the approximation will be compared with the numerical results. Finally, test cases will be used to verify the numerical model. The hydrodynamic part of the model is tested against the experiment of dam break flow in an 90° bend. Then, the coupled model is tested on the scour problem around a

spur dike by surge waves. The result from the coupled model will be compared with the traditional model with a quasi-steady approach.

2.2 Governing Equations

2.2.1 Shallow Water Equations

The governing equations are the non-linear shallow water equations

$$\frac{\partial \xi}{\partial t} + \frac{\partial (uh)}{\partial x} + \frac{\partial (vh)}{\partial y} = 0 \tag{2.1}$$

$$\frac{\partial (uh)}{\partial t} + \frac{\partial (u^2 h)}{\partial x} + \frac{\partial (uvh)}{\partial y} - \nu \left(\frac{\partial (hu_x)}{\partial x} + \frac{\partial (hu_y)}{\partial y} \right) = \frac{\tau_{wx} - \tau_{bx}}{\rho} - gh\frac{\partial \xi}{\partial x} + hfv \tag{2.2}$$

$$\frac{\partial (vh)}{\partial t} + \frac{\partial (uvh)}{\partial x} + \frac{\partial (v^2 h)}{\partial y} - \nu \left(\frac{\partial (hv_x)}{\partial x} + \frac{\partial (hv_y)}{\partial y} \right) = \frac{\tau_{wy} - \tau_{by}}{\rho} - gh\frac{\partial \xi}{\partial y} - hfu \tag{2.3}$$

where ξ is the free surface elevation above the still water level h_s, h is the total water depth $(= h_s + \xi)$, u and v are the depth-averaged velocities in the x and y directions respectively, t is time, τ_{wx} and τ_{wy} are wind shear stresses, τ_{bx} and τ_{by} are bottom friction forces, ν is the viscosity, g is the gravity constant, and f is the Coriolis parameter.

In order to obtain the hyperbolic formulation, the $gh\frac{\partial \xi}{\partial x}$ and $gh\frac{\partial \xi}{\partial y}$ terms are split according to

$$gh\frac{\partial \xi}{\partial x} = \frac{1}{2}g\frac{\partial (\xi^2 + 2\xi h_s)}{\partial x} + g\xi S_{ox} \tag{2.4}$$

$$gh\frac{\partial \xi}{\partial y} = \frac{1}{2}g\frac{\partial (\xi^2 + 2\xi h_s)}{\partial y} + g\xi S_{oy} \tag{2.5}$$

Using this splitting approach, the shallow water equations (Eqns. 2.1,2.2,2.3) can be rewritten as

$$\frac{\partial \xi}{\partial t} + \frac{\partial (uh)}{\partial x} + \frac{\partial (vh)}{\partial y} = 0 \tag{2.6}$$

$$\frac{\partial(uh)}{\partial t} + \frac{\partial(u^2h + \frac{1}{2}g(\xi^2 + 2\xi h_s))}{\partial x} + \frac{\partial(uvh)}{\partial y} - \nu\left(\frac{\partial(hu_x)}{\partial x} + \frac{\partial(hu_y)}{\partial y}\right) = \frac{\tau_{wx} - \tau_{bx}}{\rho} - g\xi S_{ox} + hfv \tag{2.7}$$

$$\frac{\partial(vh)}{\partial t} + \frac{\partial(uvh)}{\partial x} + \frac{\partial(v^2h + \frac{1}{2}g(\xi^2 + 2\xi h_s))}{\partial y} - \nu\left(\frac{\partial(hv_x)}{\partial x} + \frac{\partial(hv_y)}{\partial y}\right) = \frac{\tau_{wy} - \tau_{by}}{\rho} - g\xi S_{oy} - hfv \tag{2.8}$$

2.2.2 Sediment Conservation and Transport Equations

Only bed load is considered in this work. There are many bed load transport rate formulas in the literature in which most of them relate bed load transport rate with bed shear stress. However, an alternative simple formula, the Grass formula (Grass 1981), which relates the bed load to flow velocities is often used in many sediment transport numerical models (Cao et al. 2002; Hudson and Sweby 2003; Hudson et al. 2005). The Grass formula has the form

$$q_{sx} = Au\left(u^2 + v^2\right)^{\frac{m-1}{2}} \tag{2.9}$$

$$q_{sy} = Av\left(u^2 + v^2\right)^{\frac{m-1}{2}} \tag{2.10}$$

where A and m are parameters determined by the properties of the sediment. In this paper, $A = 0.001$ and $m = 3$ are chosen which correspond to fine sand. q_{sx} and q_{sy} are the sediment transport rate in the x and y directions respectively.

The conservation law of the sediment is described by the Exner equation (García 1999)

$$\frac{\partial z}{\partial t} + \frac{1}{1 - \epsilon_0}\left(\frac{\partial q_{sx}}{\partial x} + \frac{\partial q_{sy}}{\partial y}\right) = 0 \tag{2.11}$$

where z is the bed elevation, ϵ_0 is the sediment porosity.

2.3 Numerical Method of the Model

Integrating the governing equations over the domain Ω and using Green's theorem, the integral form of the governing equation can be written as

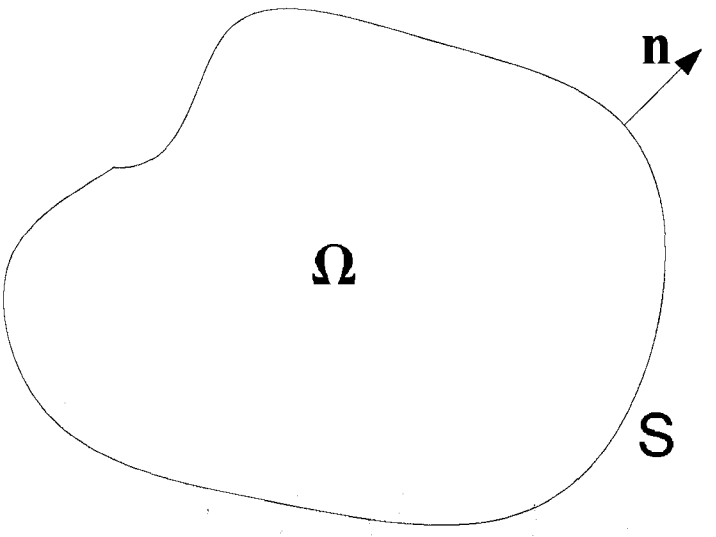

Figure 2.1: Scheme of the Computational Domain

$$\frac{\partial}{\partial t}\iint_{\Omega}\mathbf{Q}\,\mathrm{d}\Omega+\oint_{S}\mathbf{F}\cdot\mathbf{n}\mathrm{d}S=\iint_{\Omega}\mathbf{H}\mathrm{d}\Omega \tag{2.12}$$

where Ω is the domain of interest, S is the boundary of Ω (see Figure. 2.1), $\mathbf{n}$ is the outward surface normal vector of S, $\mathbf{Q}$ is the conservative variables vector, $\mathbf{F}$ is the flux vector, and $\mathbf{H}$ is the source term vector. The forms of $\mathbf{Q}$, $\mathbf{F}$, and $\mathbf{H}$ will be listed in the following sections. $\mathbf{F}$ can be split into viscous and inviscid flux components as follows:

$$\mathbf{F}\cdot\mathbf{n}=F^{I}-F^{V}=\left(f^{I}-\nu f^{V}\right)n_{x}+\left(g^{I}-\nu g^{V}\right)n_{y} \tag{2.13}$$

where n_x and n_y are the Cartesian components of the normal vector ($\sqrt{n_x^2+n_y^2}=|\mathbf{n}|$=1), and superscripts I and V denote invicid and viscous components respectively.

2.3.1 Quasi-Steady Approach

For quasi-steady approach, the SWEs are analyzed separately from the Exner equation. Just for the SWEs, $\mathbf{Q}$, $\mathbf{F}$ and $\mathbf{H}$ have the forms

$$\mathbf{Q} = \begin{bmatrix} \xi \\ uh \\ vh \end{bmatrix} \quad f^I = \begin{bmatrix} uh \\ u^2h + g(\xi^2 + 2\xi h_s)/2 \\ uvh \end{bmatrix} \quad g^I = \begin{bmatrix} vh \\ uvh \\ v^2h + g(\xi^2 + 2\xi h_s)/2 \end{bmatrix}$$

$$f^V = \begin{bmatrix} 0 \\ h\frac{\partial u}{\partial x} \\ h\frac{\partial v}{\partial x} \end{bmatrix} \quad g^V = \begin{bmatrix} 0 \\ h\frac{\partial u}{\partial y} \\ h\frac{\partial v}{\partial y} \end{bmatrix} \quad \mathbf{H} = \begin{bmatrix} 0 \\ \frac{\tau_{wx} - \tau_{bx}}{\rho} - g\xi S_{ox} + hfv \\ \frac{\tau_{wy} - \tau_{by}}{\rho} - g\xi S_{oy} - hfu \end{bmatrix} \tag{2.14}$$

The Exner equation is also descretized using the FVM and Green theorem as Eqn. 2.12. However, the Godunov scheme is not used here simply because the sediment transport rate is not a function of the bed elevation z and therefore the Jacobian matrix (only one element in this case) can not be evaluated. The fluxes across the cell interfaces are calculated using the variable values at the edges. For the Exner equation, $\mathbf{Q}$, $\mathbf{F}$, and $\mathbf{H}$ have the forms

$$\mathbf{Q} = z \quad \mathbf{F} \cdot \mathbf{n} = \frac{1}{1 - \epsilon_0}(q_{sx}n_x + q_{sy}n_y) \quad \mathbf{H} = 0.$$

2.3.2 Coupled Approach

For the coupled approach, the SWEs and Exner equation form an expanded system. **Q**, **F**, and **H** have the forms

$$\mathbf{Q} = \begin{bmatrix} \xi \\ uh \\ vh \\ z \end{bmatrix} \quad f^I = \begin{bmatrix} uh \\ u^2h + g(\xi^2 + 2\xi h_s)/2 \\ uvh \\ \frac{1}{1-\epsilon_0} q_{sx} \end{bmatrix} \quad g^I = \begin{bmatrix} vh \\ uvh \\ v^2h + g(\xi^2 + 2\xi h_s)/2 \\ \frac{1}{1-\epsilon_0} q_{sy} \end{bmatrix}$$

$$f^V = \begin{bmatrix} 0 \\ h\frac{\partial u}{\partial x} \\ h\frac{\partial v}{\partial x} \\ 0 \end{bmatrix} \quad g^V = \begin{bmatrix} 0 \\ h\frac{\partial u}{\partial y} \\ h\frac{\partial v}{\partial y} \\ 0 \end{bmatrix} \quad \mathbf{H} = \begin{bmatrix} 0 \\ \frac{\tau_{wx} - \tau_{bx}}{\rho} - g\xi S_{ox} + hfv \\ \frac{\tau_{wy} - \tau_{by}}{\rho} - g\xi S_{oy} - hfu \\ 0 \end{bmatrix} \tag{2.15}$$

2.4 Evaluation of Numerical Fluxes

The fluxes **F** across the interface between each two triangles are separated into inviscid and viscous fluxes. The numerical treatment of these two fluxes are different. For the inviscid fluxes, the one-dimensional Riemann problem is extended to two dimensions. Analytical or approximate solvers of the Riemann problem can be used to evaluate the fluxes. While for the viscous fluxes, the evaluation of the velocity gradient is taken at the edge's center which can be used to calculate the viscous fluxes.

2.4.1 Inviscid Fluxes

The analytical solver of Riemann problem is slow comparing with the approximate solvers. Among many choices of approximate solvers, Roe's approach (Roe 1981; 1986) is used in this work. The

inter-cell inviscid flux $\mathbf{F}^I_{i,j}$ by Roe's solver can be written as

$$\mathbf{F}^I_{i,j} = \frac{1}{2}\left[\mathbf{F}^I(Q^+_{i,j}) + \mathbf{F}^I(Q^-_{i,j}) - |A|\,(\mathbf{Q}^+_{i,j} - \mathbf{Q}^-_{i,j})\right] \tag{2.16}$$

$$|A| = R\,|\Lambda|\,L \tag{2.17}$$

where $\mathbf{Q}^+_{i,j}$ and $\mathbf{Q}^+_{i,j}$ are reconstructed Riemann state variables on the right and left sides, respectively. A is the flux Jacobian matrix defined by

$$A = \frac{\partial \mathbf{F}\cdot\mathbf{n}}{\partial \mathbf{Q}} \tag{2.18}$$

Quasi-Steady Approach

Since the uncoupled approach will be compared with the coupled approach, the flux Jacobian of the two-dimensional SWEs system without the Exner equation takes the form:

$$A = \frac{\partial \mathbf{F}\cdot\mathbf{n}}{\partial \mathbf{Q}} = \begin{bmatrix} 0 & n_x & n_y \\ (c^2-u^2)n_x - uvn_y & 2un_x + vn_y & un_y \\ -uvn_x + (c^2-v^2)n_y & vn_x & un_x + 2vn_y \end{bmatrix} \tag{2.19}$$

The three distinct eigenvalues of A (by hyperbolicity of the system) are

$$\lambda^{(1)} = un_x + vn_y, \quad \lambda^{(2)} = un_x + vn_y - c, \quad \lambda^{(3)} = un_x + vn_y + c \tag{2.20}$$

while the left and right eigenvector matrices are

$$R = \begin{bmatrix} 0 & 1 & 1 \\ n_y & u - cn_x & u + cn_x \\ -n_x & v - cn_y & v + cn_y \end{bmatrix} \tag{2.21}$$

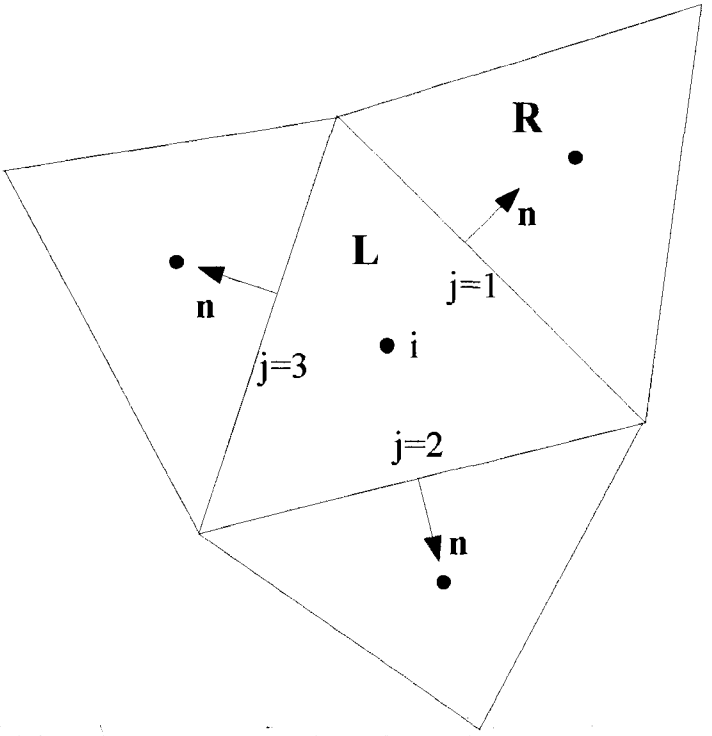

Figure 2.2: Control Volume Scheme

$$L = \begin{bmatrix} -(un_y - vn_x) & n_y & -n_x \\ \frac{un_x+vn_y}{2c} + \frac{1}{2} & \frac{-n_x}{2c} & \frac{-n_y}{2c} \\ -\frac{un_x+vn_y}{2c} + \frac{1}{2} & \frac{n_x}{2c} & \frac{n_y}{2c} \end{bmatrix} \tag{2.22}$$

The Riemann state variables u, v, and c on the face boundaries which are needed to calculate the flux are given by Roe's average as

$$u = \frac{u^+\sqrt{h^+} + u^-\sqrt{h^-}}{\sqrt{h^+} + \sqrt{h^-}}, \quad v = \frac{v^+\sqrt{h^+} + v^-\sqrt{h^-}}{\sqrt{h^+} + \sqrt{h^-}}, \quad c = \sqrt{\frac{g(h^+ + h^-)}{2}} \tag{2.23}$$

and the superscripts $+$ and $-$ refer to the right and left side of the edge.

Coupled Approach

The coupled approach needs further reformulation of the H vector in Eqn. 2.15. The slope term in H is split and written in matrix form as

$$H = \begin{bmatrix} 0 \\ \frac{\tau_{wx}-\tau_{bx}}{\rho} - g\xi S_{ox} + hfv \\ \frac{\tau_{wy}-\tau_{by}}{\rho} - g\xi S_{oy} - hfu \end{bmatrix} = \underbrace{\begin{bmatrix} 0 \\ \frac{\tau_{wx}-\tau_{bx}}{\rho} + gh_s S_{ox} + hfv \\ \frac{\tau_{wy}-\tau_{by}}{\rho} + gh_s S_{oy} - hfu \end{bmatrix}}_{(1)} + \underbrace{\begin{bmatrix} 0 \\ -ghS_{ox} \\ -ghS_{oy} \end{bmatrix}}_{(2)} \tag{2.24}$$

Term (2) in Eqn. 2.24 will be moved to the left hand side of the governing equation and combined with the Jacobian matrix of the SWEs fluxes. The purpose of this reformulation is to get a non-singular Jacobian matrix. This approach is also used in Hudson and Sweby (2003) and Hudson et al. (2005). But their governing shallow water equations are in different forms from those in this research.

The invicid fluxes on the unstructured mesh for the coupled approach can not be expressed explicitly as for the quasi-steady approach since the 4×4 Jacobian matrix is far more complicated than the 3×3 Jacobian matrix of the quasi-steady approach. In this paper, an asymptotic analysis, instead of an analytical expression, is used to approximate the eigenvalues of the Jacobian matrix of the coupled approach. This is shown in the next section.

2.5 Asymptotic Analysis of the Wave Speeds

In order to give the asymptotic analysis of the two-dimensional system, it is necessary to consider the approximation for the one-dimensional system since they are closely related to each other.

2.5.1 One-Dimensional System

The analysis for one-dimensional system is similar to Lyn (1987) and Lyn and Altinakar (2002). The general procedure of solving an algebraic equation using asymptotic approximation can be found in Nayfeh (1981). The Jacobian matrix for one-dimensional system has the form

$$J_{1D} = \frac{\partial \mathbf{F}(\mathbf{Q})}{\partial \mathbf{Q}} = \begin{pmatrix} 0 & 1 & 0 \\ -u^2 + gh & 2u & gh \\ -k\frac{u^3}{h} & k\frac{u^2}{h} & 0 \end{pmatrix} \tag{2.25}$$

where $k = 3A/(1-\epsilon_0) > 0$. The eigenvalues are the roots of the equation

$$\tilde{\lambda}^3 - 2u\tilde{\lambda}^2 + \tilde{\lambda}\left(u^2 - gh - kgu^2\right) + kgu^2 = 0 \tag{2.26}$$

where $k \mapsto 0^+$. Eqn. 2.26 has three distinct roots because the discriminant

$$\begin{aligned} \Delta &= -g\left[4hu^4 + 4g^2\left(h+ku^2\right)^3 + g\left(-8h^2u^2 + 20hku^4 + k^2u^6\right)\right] \\ &= -g\left[4hu^4 + 4g^2h^3 - 8gh^2u^2 + \left(12g^2h^2u^2 + 20ghu^4\right)k + O(k^2)\right] \\ &= -g\left[\underbrace{4g^2h^3\left(Fr^2-1\right)^2}_{\geq 0} + \underbrace{\left(12g^2h^2u^2 + 20ghu^4\right)k}_{>0} + O(k^2)\right] \\ &< 0 \end{aligned}$$

where $Fr = u/(gh)$. Let $\epsilon = kg$ and $\lambda = \tilde{\lambda}/u$, then the characteristic Eqn. 2.26 becomes

$$\lambda^3 - 2\lambda^2 + \lambda\left(1 - \frac{1}{Fr^2} - \epsilon\right) + \epsilon = 0 \tag{2.27}$$

The results are listed here and the details of the asymptotic analysis are in Appendix A. Since the regular expansion is not uniform when the flow is near critical, a change of scale is used to achieve an uniform expansion. When the flow is far away from critical state, i.e. $1 - 1/Fr^2 \gg 0$,

the three eigenvalues are given by

$$\lambda^{(1)} = \frac{\epsilon}{\frac{1}{Fr^2} - 1} \tag{2.28}$$

$$\lambda^{(2)} = 1 + \frac{1}{Fr} + \frac{\epsilon}{2\left(\frac{1}{Fr} + 1\right)} \tag{2.29}$$

$$\lambda^{(3)} = 1 - \frac{1}{Fr} - \frac{\epsilon}{2\left(\frac{1}{Fr} - 1\right)} \tag{2.30}$$

When the flow is near critical, i.e. $\left(1 - \frac{1}{Fr^2}\right) \sim \left(\epsilon^{\frac{1}{2}}\right)$, the three eigenvalues are

$$\lambda^{(1)} = \frac{2}{3} + \frac{1}{2Fr^2} \tag{2.31}$$

$$\lambda^{(2)} = \frac{1}{4}\left[1 - \frac{1}{Fr^2} + \sqrt{\left(1 - \frac{1}{Fr^2}\right)^2 + 8\epsilon}\right] \tag{2.32}$$

$$\lambda^{(3)} = \frac{1}{4}\left[1 - \frac{1}{Fr^2} - \sqrt{\left(1 - \frac{1}{Fr^2}\right)^2 + 8\epsilon}\right] \tag{2.33}$$

2.5.2 Two-Dimensional System

For a two-dimensional system, the Jacobian matrix is

$$J_{2D} = \frac{\partial F(\mathbf{Q}) \cdot \mathbf{n}}{\partial \mathbf{Q}} = An_x + Bn_y \tag{2.34}$$

where

$$A = \begin{pmatrix} 0 & 1 & 0 & 0 \\ -u^2 + gh & 2u & 0 & gh \\ -uv & v & u & 0 \\ -3k\frac{u\left(u^2+v^2\right)}{h} & k\frac{\left(3u^2+v^2\right)}{h} & 2k\frac{uv}{h} & 0 \end{pmatrix} \tag{2.35}$$

and

$$B = \begin{pmatrix} 0 & 0 & 1 & 0 \\ -uv & v & u & 0 \\ -v^2 + gh & 0 & 2v & gh \\ -3k\frac{v(u^2+v^2)}{h} & 2k\frac{uv}{h} & k\frac{(u^2+3v^2)}{h} & 0 \end{pmatrix} \tag{2.36}$$

Direct calculation of the eigenvalues/vectors of matrix J_{2D}, which is in the original global $x-y$ coordinate system, is difficult. In this work, the calculation of the Roe's fluxes is done in a local $\xi - \eta$ coordinates of each cell-to-cell interface where one of the coordinates coincides with the outward normal vector (see Fig. 2.3). This will simplify the calculation. The following theorem gives the relationship between the fluxes in the global and local coordinate systems.

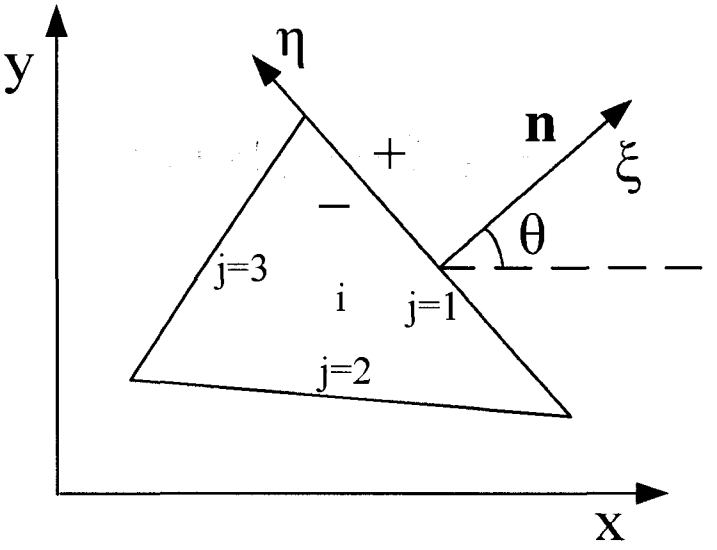

Figure 2.3: Local Coordinate at the Cell Interface

Theorem 2.5.1. *In the global and local coordinates shown as in Fig. 2.3, for the two-dimensional coupled system, suppose the interfacial Roe's flux defined in Eq. 2.16 are $F_{ij,g}$ and $F_{ij,l}$ respectively, where each flux is a vector with 4 components. Also define the transformation matrix M as*

$$M = \begin{pmatrix} \cos(\theta) & \sin(\theta) \\ -\sin(\theta) & \cos(\theta) \end{pmatrix} \tag{2.37}$$

Define sub-vectors $F_{sub,g} = [F_{ij,g}(2) \quad F_{ij,g}(3)]^T$ *and* $F_{sub,l} = [F_{ij,l}(2) \quad F_{ij,l}(3)]^T$. *Then*

1. $F_{ij,g}(1) = F_{ij,l}(1)$ *and* $F_{ij,g}(4) = F_{ij,l}(4)$

2. $F_{sub,g} = M \cdot F_{sub,l}$

Proof. The mass fluxes of water and sediment are invariant of the coordinate rotation. This means the water and sediment across the cell interface will not change under different coordinate references. The first and fourth components of the flux vector are the mass fluxes for water and sediment respectively. Then, the components can be written as

$$F_{ij,g}(1) = F_{ij,l}(1) \quad \text{and} \quad F_{ij,g}(4) = F_{ij,l}(4)$$

For the momentum fluxes of water (the second and third components of the flux vector), they follow the rule of rotational transformation stated below since they are two-dimensional vectors in the plane.

$$F_{sub,g} = M \cdot F_{sub,l}$$

□

The alternative approach of the proof is to use the Jacobian matrixes in the global and local coordinates and calculate the eigenvalues/vectores respectively. Calculation of the Roe's flux vector in the two coordinate systems will verify the conclusion of the theorem. However, the difficulty of this proof strategy is the calculation of the eigenvalues/vectors of the global Jacobian matrix. From the authors' experience, it is hard to find an explicit expression of eigen-system for the global Jacobian. Even with some simplifications, the explicit expression is lengthy and not practically useful. Thus, this complication motivates the use of the coordinate transformation so that the fluxes can be evaluated in the local coordinates which is simple and easy to analyze.

In the local coordinate, since $n_\xi = 1$ and $n_\eta = 0$ (where n_ξ and n_η are the outward normal vector component in ξ and η directions), the Jacobian matrix in terms of the transformed velocity

vectors has the form of

$$J_{2D,l} = \begin{pmatrix} 0 & 1 & 0 & 0 \\ -u_\xi^2 + gh & 2u_\xi & 0 & gh \\ -u_\xi v_\eta & v_\eta & u_\xi & 0 \\ -3k\frac{u_\xi\left(u_\xi^2+v_\eta^2\right)}{h} & k\frac{\left(3u_\xi^2+v_\eta^2\right)}{h} & 2k\frac{u_\xi v_\eta}{h} & 0 \end{pmatrix} \tag{2.38}$$

This Jacobian matrix is similar to that in Hudson and Sweby (2005) in which their analysis is for structured mesh. One of the eigenvalues of $J_{2D,l}$ is u_ξ, while the other threes are the solution of the polynomial equation

$$\tilde{\lambda}^3 - 2u_\xi\tilde{\lambda}^2 + \tilde{\lambda}\left[u_\xi^2 - gh - kg\left(3u_\xi^2 + v_\eta^2\right)\right] + kgu_\xi\left[3u_\xi^2 + v_\eta^2\right] = 0 \tag{2.39}$$

Eqn. 2.39 has three distinct roots because the discriminant is negative.

$$\begin{aligned} \Delta &= g\left[-4hu_\xi^4 - 4g^2\left(h + k\left(3u_\xi^2 + v_\eta^2\right)\right) - gu_\xi^2\left(-8h^2 + 20hk\left(3u_\xi^2 + v_\eta^2\right) + k^2\left(3u_\xi^2 + v_\eta^2\right)\right)\right] \\ &= -g\left[4hu_\xi^4 - 8gh^2u_\xi^2 + 4g^2h^3 + gh\left(12gh + 20u_\xi^2\right)\left(3u_\xi^2 + v_\eta^2\right)k + O(k^2)\right] \\ &= -g\left[\underbrace{4h\left(u_\xi^2 - gh\right)^2}_{\geq 0} + \underbrace{gh\left(12gh + 20u_\xi^2\right)\left(3u_\xi^2 + v_\eta^2\right)k}_{>0} + O(k^2)\right] \\ &< 0 \end{aligned}$$

If $u_\xi = 0$, the three roots of Eqn. 2.39 are 0, $\sqrt{gh + kgv_\eta^2}$, and $-\sqrt{gh + kgv_\eta^2}$. The eigensystems for the cases of $u_\xi = 0$ are list in Appendix A.2. For the general case of $u_\xi \neq 0$, defining $\epsilon = kg\left(3u_\xi^2 + v_\eta^2\right)/u_\xi^2$ and $\lambda = \tilde{\lambda}/u_\xi$, Eqn. 2.39 can be written as

$$\lambda^3 - 2\lambda^2 + \lambda\left[1 - \frac{1}{Fr^2} - \epsilon\right] + \epsilon = 0$$

where $Fr = u_\xi/gh$. This is the same as the form for one-dimensional case and the eigenvalues can be approximated using perturbation analysis as in Eqns. 2.28 to 2.31. In summary, the eigenvalues

λ_i and right eigenvectors $\mathbf{R}_i$ for the two-dimensional system in the local coordinate are listed below. The right eigenvector matrix is

$$R = \begin{bmatrix} -2kv_\eta & -gh & -gh & -gh \\ -2ku_\xi v_\eta & -gh\tilde{\lambda}^{(2)} & -gh\tilde{\lambda}^{(3)} & -gh\tilde{\lambda}^{(4)} \\ h-2kv_\eta^2 & -ghv_\eta & -ghv_\eta & -ghv_\eta \\ 2kv_\eta & gh-\left(\tilde{\lambda}^{(2)}-u_\xi\right)^2 & gh-\left(\tilde{\lambda}^{(3)}-u_\xi\right)^2 & gh-\left(\tilde{\lambda}^{(4)}-u_\xi\right)^2 \end{bmatrix} \tag{2.40}$$

and the left eigenvector matrix is

$$L = \begin{bmatrix} -\frac{v_\eta}{h} & 0 & \frac{1}{h} & 0 \\ \frac{a_1-a_2\tilde{\lambda}^{(4)}-\tilde{\lambda}^{(3)}\left(a_2+a_3\tilde{\lambda}^{(4)}\right)}{gh^2b_1} & \frac{-2u_\xi+\tilde{\lambda}^{(3)}+\tilde{\lambda}^{(4)}}{ghb_1} & \frac{-2kv_\eta\left(u_\xi-\tilde{\lambda}^{(3)}\right)\left(u_\xi-\tilde{\lambda}^{(4)}\right)}{gh^2b_1} & \frac{-1}{b_1} \\ \frac{a_1-a_2\tilde{\lambda}^{(4)}-\tilde{\lambda}^{(2)}\left(a_2+a_3\tilde{\lambda}^{(4)}\right)}{gh^2b_2} & \frac{-2u_\xi+\tilde{\lambda}^{(2)}+\tilde{\lambda}^{(4)}}{ghb_2} & \frac{-2kv_\eta\left(u_\xi-\tilde{\lambda}^{(2)}\right)\left(u_\xi-\tilde{\lambda}^{(4)}\right)}{gh^2b_2} & \frac{-1}{b_2} \\ \frac{a_1-a_2\tilde{\lambda}^{(3)}-\tilde{\lambda}^{(2)}\left(a_2+a_3\tilde{\lambda}^{(3)}\right)}{gh^2b_3} & \frac{-2u_\xi+\tilde{\lambda}^{(2)}+\tilde{\lambda}^{(3)}}{ghb_3} & \frac{-2kv_\eta\left(u_\xi-\tilde{\lambda}^{(2)}\right)\left(u_\xi-\tilde{\lambda}^{(3)}\right)}{gh^2b_3} & \frac{-1}{b_3} \end{bmatrix} \tag{2.41}$$

where $a_1 = -gh^2+hu_\xi^2+2ku_\xi^2v_\eta^2$; $a_2 = 2ku_\xi v_\eta^2$, $a_3 = \left(h-2kv_\eta^2\right)$; $b_1 = \left(\tilde{\lambda}^{(2)}-\tilde{\lambda}^{(3)}\right)\left(\tilde{\lambda}^{(2)}-\tilde{\lambda}^{(4)}\right)$; $b_2 = \left(\tilde{\lambda}^{(3)}-\tilde{\lambda}^{(2)}\right)\left(\tilde{\lambda}^{(3)}-\tilde{\lambda}^{(4)}\right)$; and $b_3 = \left(\tilde{\lambda}^{(4)}-\tilde{\lambda}^{(2)}\right)\left(\tilde{\lambda}^{(4)}-\tilde{\lambda}^{(3)}\right)$.

The eigenvalues of the two-dimensional system can also be calculated using a numerical method. For comparison, the four eigenvalues from both the asymptotic approximation and the numerical method are plotted in Fig. 2.4 with ϵ equal to 0.01. The figures are similar to those in Lyn and Altinakar (2002). Fig. 2.4(a) shows the four eigenvalues for Fr between 0.2 and 2. For $Fr > 1.2$ or $Fr < 0.8$, the regular expansion formula is used, while for $0.8 < Fr < 1.2$, the re-scaled expansion formula is used. Both asymptotic approximation and numerical results are shown in the figure. Results from both methods are nearly identical. Major part of the error occurs when the flow is near critical. where the relative error is within 1%.

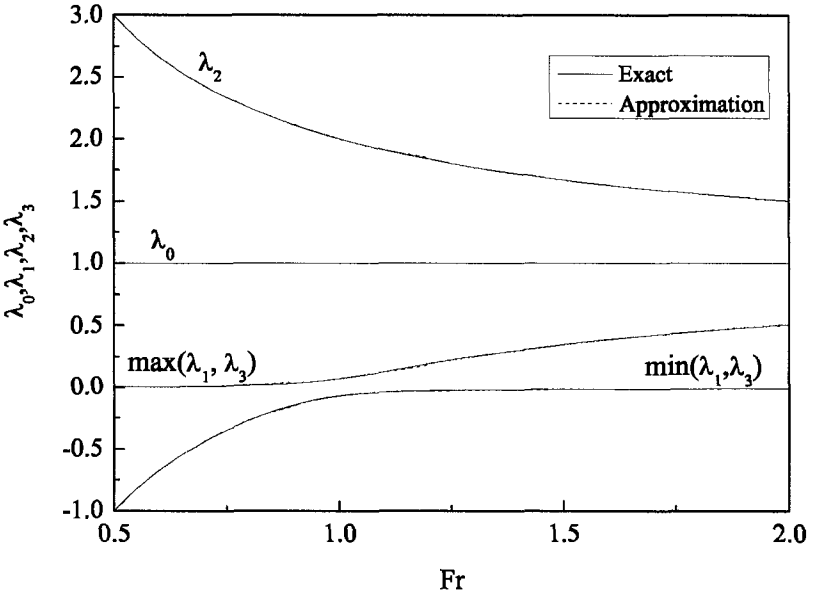

(a)

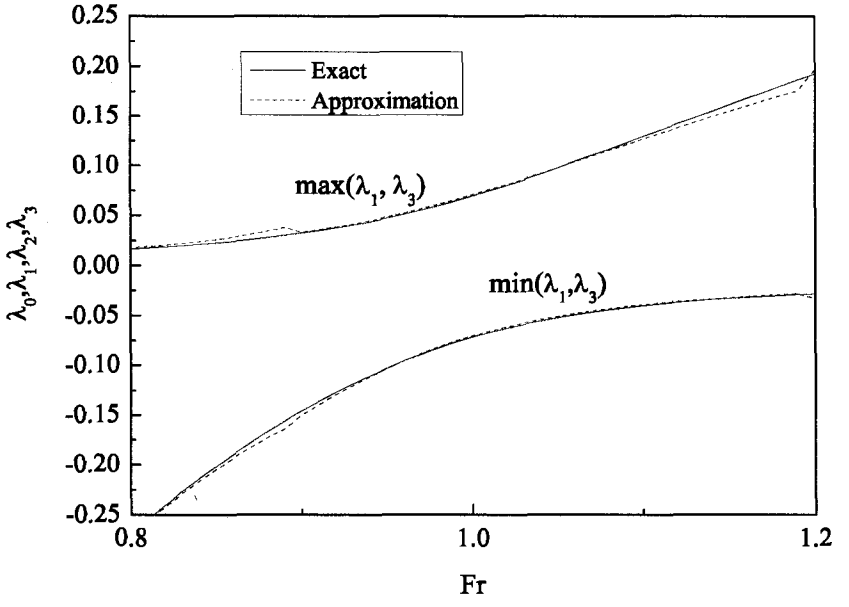

(b)

Figure 2.4: Eigenvalues of Two-Dimensional System: (a) $0.5 < Fr < 2$ (b) Zoom-In View around $Fr = 1$

2.5.3 Viscous Fluxes

Viscous fluxes are not evaluated via Roe's flux function. Instead, the viscous fluxes are calculated directly using the velocity gradient at the boundary. By Gauss's theorem, the velocity gradient term in the cell center can be estimated by closed line integral over the boundary of that cell (Anastasiou and Chan 1997).

2.6 Limiter for High Order Schemes

The evaluation of the Riemann states on both sides of the cell interface needs interpolation since all the conservative variables are stored at the cell center. This step is usually called variable reconstruction. The following equation is the relation between the interpolated variable at an arbitrary location (x, y) and the value at the cell center

$$Q(x, y) = Q_c + \nabla Q \cdot \mathbf{r} \tag{2.42}$$

where Q_c is the variable value at cell center, ∇Q is the gradient of Q, and $\mathbf{r}$ is the vector from cell center to (x, y). This is a piecewise linear interpolation which has second order accuracy. Second and higher order schemes will introduce numerical oscillations. In order to maintain monotonicity, non-linear limiters are introduced to eliminate oscillations in high gradient areas while keeping high accuracy in smooth areas. The limited version of the reconstruction equation has the form

$$Q(x, y) = Q_c + \Phi(r_f)\nabla Q \cdot \mathbf{r} \tag{2.43}$$

where Φ is a function of r_f, which is the upwind ratio of consecutive gradients of the variable. For the structured mesh, r_f is easy to calculate because the topological relation of upwind and down-wind is clear. For the unstructured mesh, it becomes difficult. The so-called exact r formulation in Darwish and Moukalled (2003) is used in this work. Fig. 2.5 shows the layout of the cells. For

face f, C and D are defined as the upwind and downwind cells according to the direction of the flow velocity. U is defined as the virtual upwind cell of C. The formulation of r_f is

$$r_f = \frac{(2\nabla Q_c \cdot \mathbf{r}_{CD})}{Q_D - Q_C} - 1 \tag{2.44}$$

where $\mathbf{r}_{CD}$ is the vector connecting node C and D. After the ratio r_f is calculated, it can be used

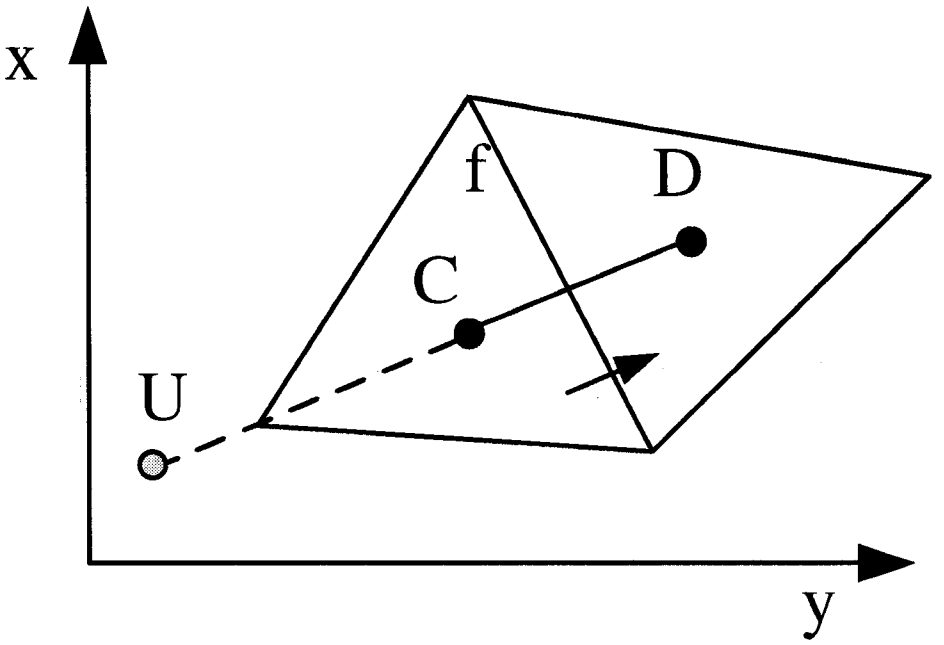

Figure 2.5: Exact r Formulation of the Limiter Function

in the limiter functions. In this paper, the MINMOD Total Variation Diminishing (TVD) scheme is used which has the following form

$$\Phi(r_f) = \max(0, \min(1, r_f)) \tag{2.45}$$

2.7 Time Integration

The time integration used in the paper is similar to the method proposed by Anastasiou and Chan (1997).

$$\left.\frac{\partial(VQ)}{\partial t}\right|_i^{n+1} = -\oint_{S_i} \mathbf{F}_i^n \cdot \mathbf{n} dS + V_i^n H_i^n \tag{2.46}$$

$$Q_i^{n+1} = Q_i^n + \frac{\Delta t}{V_i^n}\left(\alpha \left.\frac{\partial(VQ)}{\partial t}\right|_i^{n+1} + (1-\alpha)\left.\frac{\partial(VQ)}{\partial t}\right|_i^{n}\right) \tag{2.47}$$

when $\alpha = 0$, it becomes the Euler explicit scheme, while $\alpha = 1$ results in a first order Euler implicit method. For the explicit scheme, the time step is restricted by the Courant-Friedrichs-Lewy (CFL) condition. As in Yoon and Kang (2004), the following formula is used to determine the maximum time step allowed

$$\Delta t \leq \min\left(\frac{R_i}{2\max_j(\sqrt{u^2+v^2}+c)_{ij}}\right) \tag{2.48}$$

where R_i is the distance between the centroids of triangle i and j. The minimum is taken for all the triangles in the computational domain while the maximum is take for the three neighboring triangles of triangle i.

2.8 Boundary Conditions

Boundary conditions are applied to the cell faces on the domain boundary. For the hydrodynamic part of the model, the boundary conditions are the same as in Anastasiou and Chan (1997) and Rogers et al. (2001). Those boundary conditions are briefly listed below. Sediment conditions on the boundary are also discussed.

2.8.1 Walls

No-slip condition is applied to walls, i.e., $(u, v) = (0, 0)$. For sediment transport, the flux through the wall is also set to be zero which means no sediment particle will go through the solid boundary.

2.8.2 Open Boundaries

Conditions for the open boundaries, including inlet and outlet, are specified using the Riemann invariants

$$(u, v)_I \cdot \mathbf{n} + 2\sqrt{gh_I} = (u, v)_B \cdot \mathbf{n} + 2\sqrt{gh_B} \tag{2.49}$$

where subscripts I and B refer to the interface and the boundary, respectively.

For subcritical flow, if water depth h_B is specified, then

$$(u, v)_B \cdot \mathbf{n} = 2\sqrt{gh_B}(u, v)_I \cdot \mathbf{n} + 2\sqrt{gh_I} - 2\sqrt{gh_B} \tag{2.50}$$

and if velocity is specified, then

$$h_B = \frac{\left[(u, v)_I \cdot \mathbf{n} + 2\sqrt{gh_I} - (u, v)_B \cdot \mathbf{n}\right]^2}{4g} \tag{2.51}$$

Sometimes, the water discharge $q_w = h_B \left[(u, v)_B \cdot \mathbf{n}\right]$ is specified. For this case, Eqn. 2.49 can be rewritten as

$$(u, v)_I \cdot \mathbf{n} + 2\sqrt{gh_I} = \frac{q_w}{h_B} + 2\sqrt{gh_B} \tag{2.52}$$

A numerical method can be used to solve h_B and then $(u, v)_B \cdot \mathbf{n} = \frac{q_w}{h_B}$.

For the supercritical inlet, both the velocity vector and water depth should be specified. For the supercritical outlet, no boundary condition is needed to specify and the velocity vector and water depth on the boundary is the same as those in the adjacent interior.

For the sediment transport rate, the sediment flux on the inlet is specified as the sediment feed rate. On the outlet, the sediment flux is set as having a zero gradient.

2.9 Test Problems

In this section, the proposed numerical model is tested. The first test problem is just for the hydrodynamics where the bed is kept fixed. This is used to test the model capability to capture shocks as well as the robustness of the model for complicated flow conditions. The second test problem is for both the hydrodynamics and sediment transport. The flume bed is not fixed and a scour hole develops due to the flow. Both coupled and uncoupled approaches are used to simulate the process and the results are compared.

2.9.1 Dam Break Flow in Channels with 90° Bend

In this section, the hydrodynamics part of the model is tested against experimental observations. Sharp bends appear in rivers very frequently and the effects of these bends on catastrophic flooding waves are extremely important. Experiments for dam-break flood in a channels with a 90° bend were done in the laboratory of the Civil Engineering Department of the University Catholique de Louvain, Belgium. The details of the experiment can be found in S.Soares-Frazão and Zech (2002). The layout of the experiment is shown in Fig. 2.6. The channel bed is 0.33 m above the reservoir bed. The initial water surface level in the reservoir is 0.25 m above the channel bottom while the channel bed is initially dry. The dam-break flood wave is generated by a sudden release of the control gate. S.Soares-Frazão and Zech (2002) also developed a two-dimensional numerical model to capture the flood wave. Good agreement of results between the experiment and numerical model has been reported.

One of the most important factors which affect the extent of damage by dam-break floods is the shock front and free water surface. In Fig. 2.7, the modeled free water surface elevation contours at time t = 3 s, 5 s, 7 s, and 14 s are plotted. At t = 3 s, the flood wave has just reached the bend which agrees with the experiment. The bend has at least two effects on the flood wave. One is the reflection traveling upstream to the reservoir. The other effect is the reflection wave on the downstream portion of the channel which can be seen in Fig. 2.7(d).

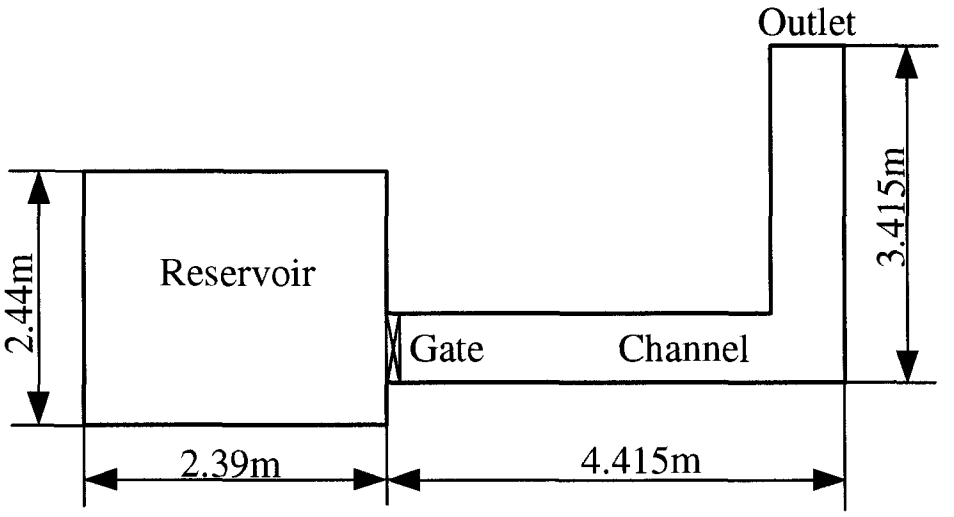

Figure 2.6: Layout of the Dam Break Experiment in Channels with 90° Bend

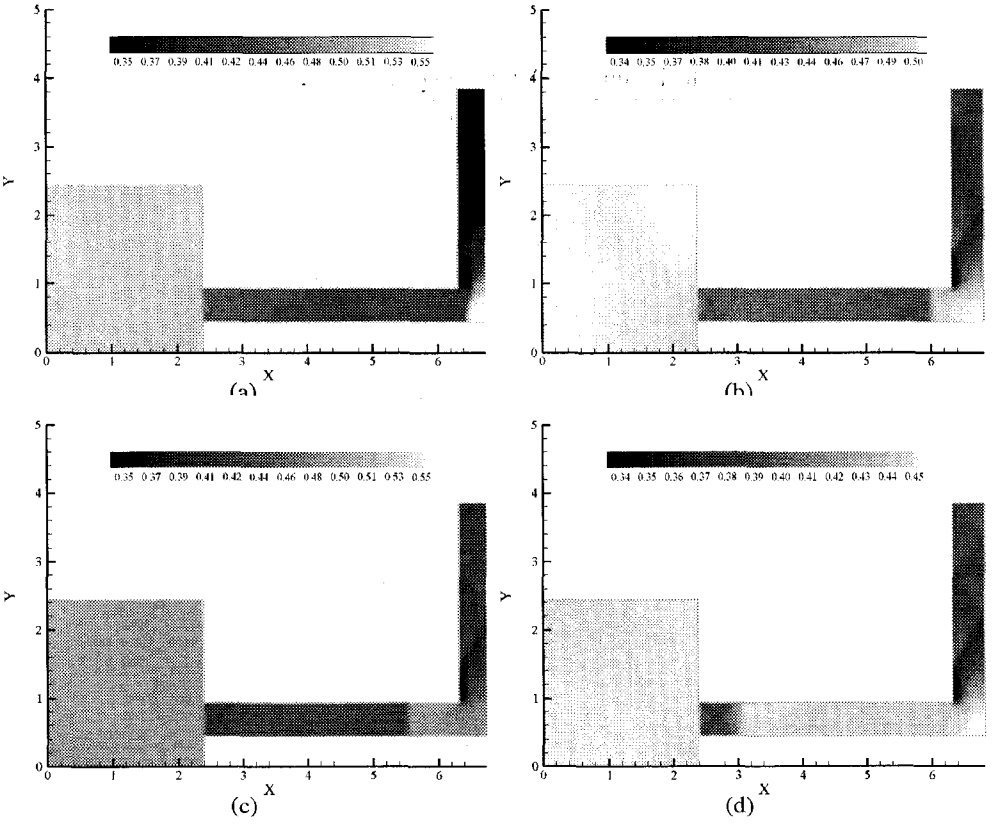

Figure 2.7: Numerical Results for Dam Break Flow in Channels with 90° Bend: (a) t = 3 s (b) t = 5 s (c) t = 7 s (d) t = 14 s

The modeled profiles of the water surface around the bend at different times are plotted in Fig. 2.8. The numerical results from S.Soares-Frazão and Zech (2002) are also plotted. The results from both numerical models agree well with the experiment. From this figure, it is clear that the upstream traveling reflection bore reaches the reservoir at around t = 14 s and after that the water level recedes. The results from this test case show the capability of the model to capture the complicated flow process and it is the basis of the coupled model simulation.

2.9.2 Scour Around the Spur Dike During a Surge Pass

The test case for the coupled model is the scour around a spur dike experiment from Mioduszewski and Maeno (2003). The experiment was done in a laboratory flume at Okayama University, Japan. Fig. 2.9(a) shows the plane view of the flume. The flume is 15 m long, 0.6 m wide, and 0.4 m deep. The sand has d_{50} = 1.28 mm. The spur dike is not submerged. It is 6 cm thick and 15 cm wide. Case 1 of the experiment is chosen for comparison. The water discharge was set to the value of Q = 0.005 m^3/s. The initial water depth is 20 cm and a surge wave is generated by opening the gate at the downstream end of the flume at t = 0 s. The unstructured mesh for this test case is shown in Fig. 2.9(b). The mesh around the spur dike is refined in order to capture the scour details. The experiment also investigated the pore pressure in the sand due the pass of the surge wave. This is also very important since the flow field and pressure distribution inside the sand will affect the stability of the dike structure and scour process around it (Liu and García 2007a). However, the pore pressure in the sand is beyond the scope of this paper and therefore it is not considered.

The velocity field around the spur dike at t = 20 s is plotted in Fig. 2.10. A recirculation zone is formed behind the spur dike. Also because of the blocking effect of the dike, the flow velocity is higher around the tip area. These flow characteristics are the cause of the sediment movement and will affect the scour pattern. The free water surface around the spur dike at t = 20 s is plotted in Fig. 2.11. Water elevation is higher in front of the spur dike and lower behind it.

In Fig. 2.12, the final scour patterns from the experiments, the quasi-steady simulation, and the coupled approach simulation are shown. The basic scour pattern from the experiment is that

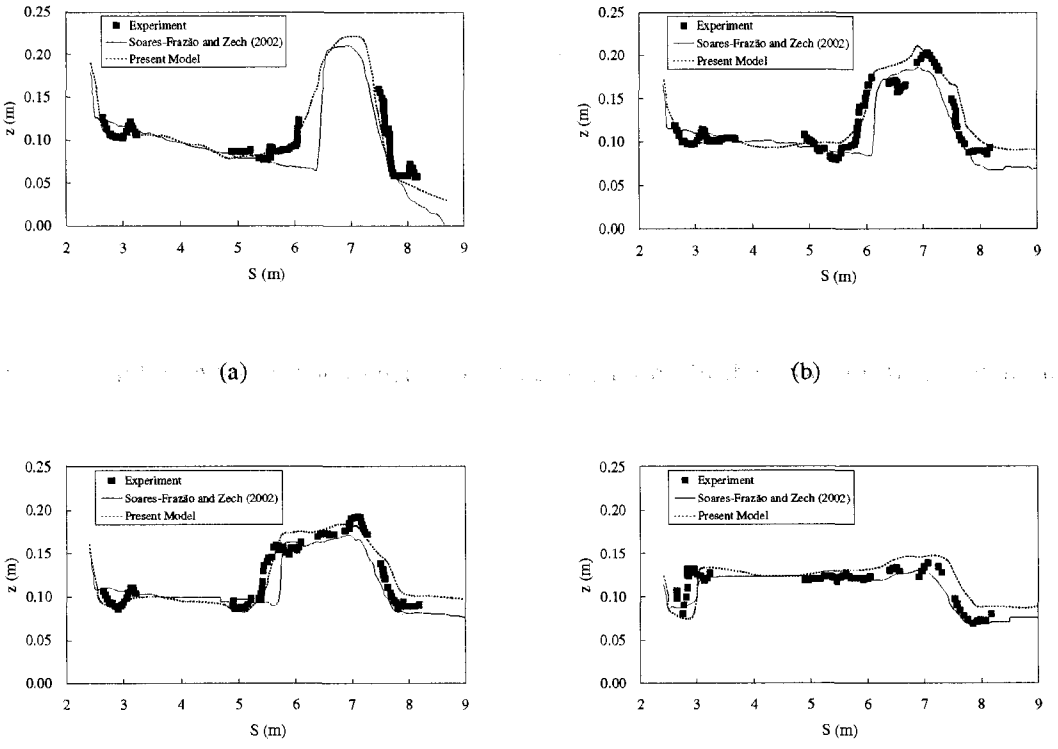

Figure 2.8: Numerical Results for the Free Surface Profiles in Channels with 90° Bend: (a) t = 3 s (b) t = 5 s (c) t = 7 s (d) t = 14 s

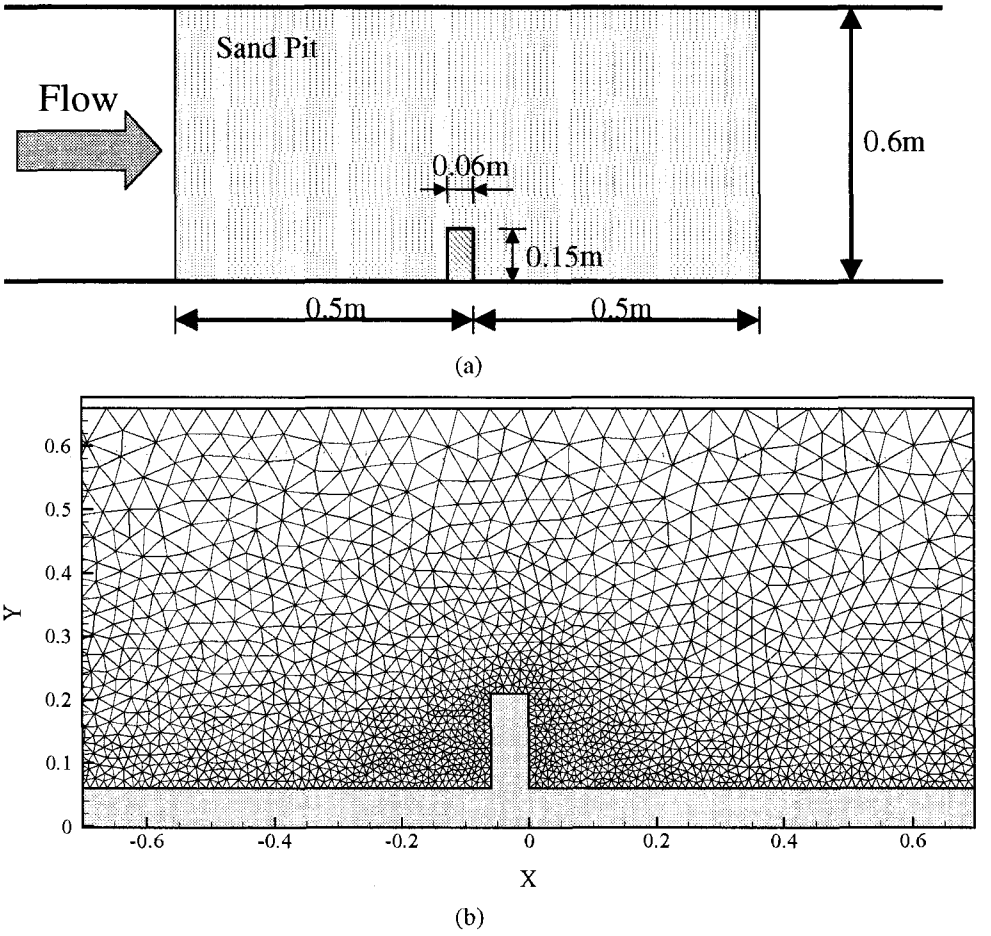

Figure 2.9: Scour around the Spur Dike During a Surge Pass Experiment: (a) Experiment Layout (b) Unstructured Mesh around the Spur Dike

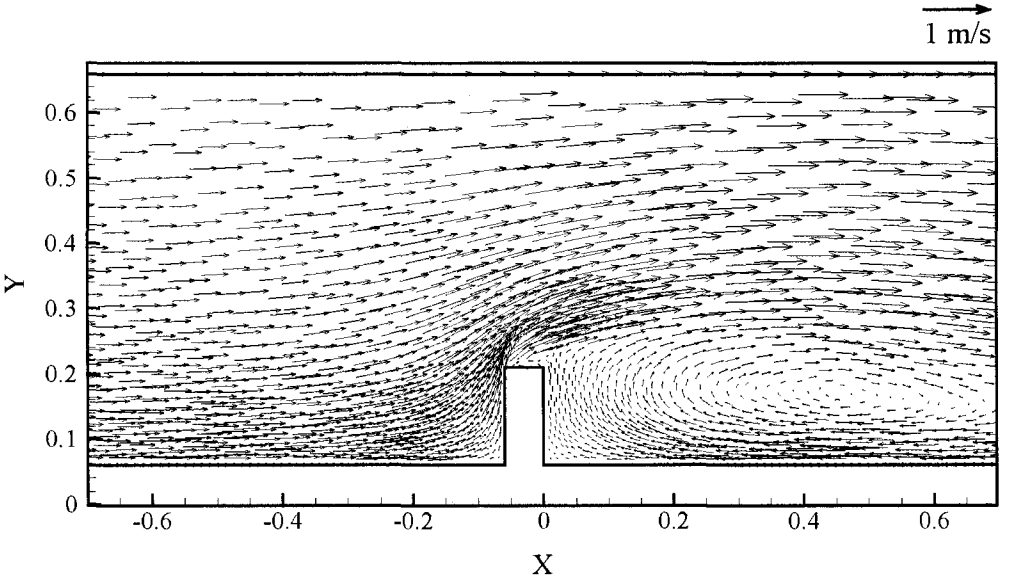

Figure 2.10: Velocity Field around the Spur Dike at t = 20 s

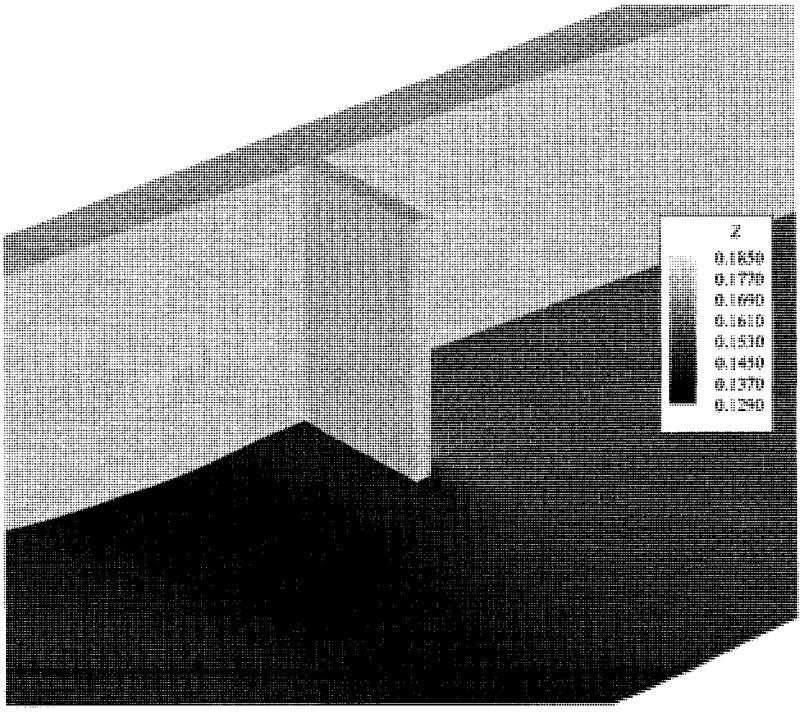

Figure 2.11: Water Surface around the Spur Dike

the sediment is scoured away from the tip of the spur dike and deposited on the back of it. From the comparison, the coupled approach gives a more accurate result than that from the quasi-steady approach. For the coupled approach, the maximum scour is about 8 mm and is located at the upstream tip of the spur dike. This agrees with the experiment. For the quasi-steady approach, the maximum scour is about 6 mm, which is a little less than the experiment. The deposition behind the spur dike comes from the sediment scoured away upstream and it is retained there by the recirculation zone. The maximum deposition height is about 3 mm which is captured by both approaches. The locations of the maximum deposition for both approaches are a little further downstream when compared to the experiment. The reason could be that both approaches are two-dimensional models and the three-dimensional phenomena are not captured (such as horse shoe vortex, non-hydrostatic pressure distribution, etc.). In order to give more accurate results, three-dimensional scour model with a free water surface should be used (Liu and García 2006a).

The asymptotic analysis of the eigenvalues not only gives an insight on the functional relationship between the wave speeds and control parameters, such as Fr and sediment properties, but it also increases the efficiency of the numerical model and reduces simulation time. Other than asymptotic analysis, numerical iteration can be used to evaluate the eigenvalues. However, numerical evaluation is slower comparing with asymptotic analysis. For numerical eigenvalue evaluation, the computational cost is $25n^3$, where n is the dimension of the Jacobian matrix (Heath 1996). While for asymptotic approximation, since all eigenvalues and eigenvectors are explicitly expressed, the computational cost is only a function of n^2. In order to demonstrate the efficiency of the asymptotic approximation method, the test problem is run for different mesh sizes with both numerical eigenvalue evaluation and asymptotic approximation. For numerical eigenvalue evaluation, the numerical routine DGEEV for general non-symmetric matrix in LAPACK (Anderson et al. 1999) is used. For this test case, four different mesh sizes (2541, 1306, 915 and 670 triangles) are used for both methods. For the same mesh size, the simulation results are the same. But the computation time by asymptotic approximation method is far less than the numerical eigenvalue evaluation method. The computational time on a computer with Intel Pentium 4, 3.2GHz CPU,

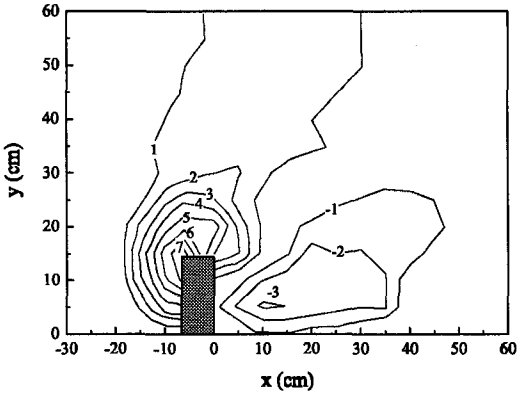

(a)

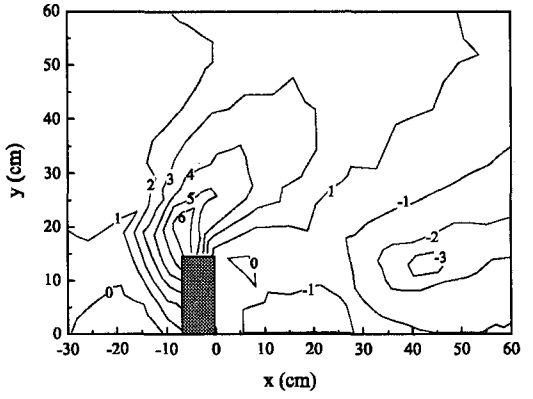

(b)

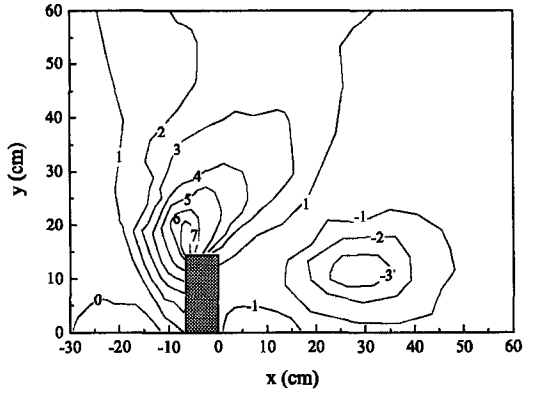

(c)

Figure 2.12: Scour around the Spur Dike: (a) Experiment (b) Quasi-Steady Approach (c) Coupled Approach

and 4G RAM is listed in Table 1. For all the four mesh sizes, the ratio between the simulation times by numerical method (T_n) and asymptotic method (T_a) is about the same (2.7 in this case). The reason for the similarity is due to the fact that the majority of the computational time is spent on the calculation of the eigen-system. For both methods, the computational cost of the eigen-system is a linear function of the mesh size. Therefore the total computational time of the model is also a linear function of the mesh size. The ratio T_n/T_a slightly increases with the increase of the mesh size. This means for larger cases, the asymptotic method is even more efficient. In conclusion, the proposed asymptotic method reduced the computational time by about 64% (this number might vary depending on the test case and model implementation), making this an attractive alternative to previous methods.

Table 2.1: Computational Time by Different Eigenvalue Evaluation Methods (Unit: s)

Mesh Size	Time Step (s)	Computational Time		Ratio T_n/T_a
		Asymptotic T_a	Numerical T_n	
2541	0.002	1497	4179	2.79
1306	0.002	759	2069	2.73
915	0.002	525	1430	2.72
670	0.01	79	207	2.62

2.10 Discussion and Conclusions

The coupled model of 2D SWEs and sediment transport on unstructured mesh can be implemented for scour problems on complex domains. It is recognized by many authors that when the scour process is rapid (such as scour caused by dam/dike break, surge waves, etc.), the coupled model approach is needed. When the scour process is slow (such as long term aggradation/degradation of natural rivers), both the usual quasi-steady approach and the coupled approach can give good results (Hudson and Sweby 2003; Hudson et al. 2005; Cao et al. 2002). However, as pointed out by Cao et al. (2002), the numerical stability of the quasi-steady approach will present a difficulty. High order discretization of the Exner equation may lead to non-physical oscillations which could be

incorrectly interpreted as ripples and sand waves. Low order discretization of the Exner equation may under-estimate the amplitude of the real sand wave or even smear it out. The hyperbolic nature of the Exner equation (even though there is dispersion effect in the equation) makes it possible to couple it with SWEs and to use Godunov schemes. The coupled model with the higher order Godunov scheme proposed in this paper can capture the real wave accurately while control the growth of non-physical oscillations.

The asymptotic analysis gives insight into the wave speed structure and helps to construct an explicit expression for the Roe's flux. It also gives a fast and accurate evaluation of the eigenvalues/vectors. Comparing to the numerical iteration method for the eigen-system, the asymptotic approximation is far more efficient. For the test case used in this paper, the average computational time can be reduced by around 64%. This efficiency could be very important when the numerical model proposed in this paper is applied for real cases where people's lives and property are in danger.

The interpolation method of the TVD scheme used in current numerical model for the upwind ratio of consecutive gradients is based on the virtual upwind node. The basic assumption is the gradient from upwind node to downwind node is the same as that from center node to downwind node. This assumption simplifies the calculation and reduces the computational stencil. Future research is needed on the comparison of different interpolation methods and TVD schemes.

Chapter 3

Three Dimensional Simulation of Local Scour with Free Water Surface and Mesh Deformation

3.1 Introduction

Local scour problems have been studied for many years both experimentally and numerically. In this paper, a new numerical model is proposed to simulate the scour process in the presence of a free surface and allowing for automatic mesh deformation. In the scour problem, there are at least two sharp interfaces: water-air and water-sediment. In this work, these two interfaces are captured using different methods. The water-air interface is captured with an Eulerian method, namely volume of fluid (VOF) method. The water-sediment interface behavior is captured with a Lagrangian method, namely moving-mesh method (Liu and García 2006a).

In numerical simulations of open channel flow, free water surface is usually replaced by a rigid lid. This is valid only if the free surface does not change too much along the channel. For rapidly changing water surface (e.g., hydraulic jump), the rigid lid approximation will introduce nonphysical errors. There are many surface tracking or capturing methods available to simulate the free surface, e.g., marker and cell (MAC) method, volume of fluid (VOF) method, level set method (LSM). MAC method is based on a Lagrangian approach and a set of marker particles whose position at any time step are used to reconstruct the interface. VOF method is based on the Eulerian point of view instead. The widely used VOF method was first proposed by Hirt and Nicholls (1981) which used a donor-acceptor formulation. VOF method has been used by several

*This chapter, as a manuscript, has been accepted for publication in Journal of Waterway, Port, Coast and Ocean Engineering, ASCE

researchers to capture the free water surface when the scour process is investigated. Among many others, Richardson and Panchang (1998) used commercial code $Flow-3D^{®}$, which implemented the VOF method on structured mesh, to simulate the flow field around the scour holes. The flow field compared well with the experiments and the particle tracking in the resulting free surface flow field revealed some of the characteristics of the scour process. Level set method divides the domain into grid points which hold the value of level set function (Sethian 1996). The contour of zero level set gives the interface. Level set method has a more rigorous mathematical basis and it is easier to calculate the curvature on the surface which is important for the surface tension force. In this work, a high resolution VOF method proposed by Ubbink and Issa (1999) is chosen to track the free surface. The CICSAM (Compressive Interface Capturing Scheme for Arbitrary Meshes) scheme treat the whole domain as the mixture of two liquids. Volume fraction of each liquid is used as the weighting factor to get the mixture properties, such as density and viscosity.

In the scour problem, the bed deformation needs to be coupled with the transient flow field. Brørs (1999) used a structured grid to model the scour under pipelines. The grid on the bed and the corresponding grids above were moved according to bed elevation changes. This method for structured grids is similar to manually moving each grid point at each time step and is not efficient. Another alternative is to use the so called blocking method. The downside of the method is that the accuracy depends on the mesh size around the interface.

In unstructured grids, it is more complicated to move the grid points on the bed and in the domain. Arbitrary movement of the points may invalidate the grid. Herein, an automatic grid movement algorithm is used to avoid these problems. There are many mesh deformation methods developed in the past years, such as spring analogy and Laplacian operator smoothing. The latter is chosen in this work because it is more robust and easy to implement in unstructured grid for complex domain. The Laplacian operator smoothing method is used here to solve the Laplacian equation with the deformation condition at the boundary. With this approach, the inner grid deforms smoothly and the computations are stable.

3.2 Governing Equations

3.2.1 Fluid Flow Model

The governing equations for the fluid flow are the Reynolds-averaged Navier-Stokes equations:

$$\nabla \cdot \mathbf{u} = 0 \tag{3.1}$$

$$\frac{\partial \rho \mathbf{u}}{\partial t} + \nabla \cdot (\rho \mathbf{u}\,\mathbf{u}) - \nabla \cdot ((\mu + \mu_t)\mathbf{S}) = -\nabla p + \rho \mathbf{g} + \sigma K \frac{\nabla \alpha}{|\nabla \alpha|} \tag{3.2}$$

where $\mathbf{u}$ is the velocity vector field, p is the pressure field, μ_t is the turbulent eddy viscosity,α is the volume fraction function for the two fluids defined by

$$\alpha = \begin{cases} 0 & \text{volume occupied by air} \\ 1 & \text{volume occupied by water} \end{cases} \tag{3.3}$$

$\mathbf{S}$ is the strain rate tensor defined by $\mathbf{S} = \frac{1}{2}(\nabla \mathbf{u} + \nabla \mathbf{u}^T)$. σ is surface tension, K is the surface curvature. Surface tension is not so important in the scour problem but it is included for completeness. The density ρ and viscosity μ in the domain are given by

$$\rho = \alpha \rho_1 + (1 - \alpha)\rho_2 \tag{3.4}$$

$$\mu = \alpha \mu_1 + (1 - \alpha)\mu_2 \tag{3.5}$$

The volume fraction α is transported by the fluid velocity field. The equation for the volume fraction scalar α is

$$\frac{\partial \alpha}{\partial t} + \nabla \cdot (\mathbf{u}\alpha) = 0 \tag{3.6}$$

Numerical diffusion will spread out the sharp interface between water and air. A compressive interface capturing scheme is used to resharpen the interface. Details about the present free surface modeling algorithm and CICSAM scheme can be found in Ubbink and Issa (1999).

Table 3.1: Constants in $k-\epsilon$ Model

C_μ	C_1	C_2	σ_k	σ_ϵ
0.09	1.44	1.92	1.0	1.3

3.2.2 Turbulence Model

Turbulence in the fluid flow model is estimated by the conventional k-ϵ two-equation model (Rodi 1993)

$$\mu_t = C_\mu \rho \frac{k^2}{\epsilon} \tag{3.7}$$

$$\frac{\partial k}{\partial t} + \nabla \cdot (\mathbf{u}k) = \frac{1}{\rho}\nabla(\frac{\mu_t}{\sigma_k}\nabla k) + 2\frac{\mu_t}{\rho}|\nabla \mathbf{u}|^2 - \epsilon \tag{3.8}$$

$$\frac{\partial \epsilon}{\partial t} + \nabla \cdot (\mathbf{u}\epsilon) = \frac{1}{\rho}\nabla(\frac{\mu_t}{\sigma_\epsilon}\nabla \epsilon) + 2\frac{C_1 \mu_t}{\rho}|\nabla \mathbf{u}|^2 \frac{\epsilon}{k} - C_2 \frac{\epsilon^2}{k} \tag{3.9}$$

where k is the turbulent kinetic energy and ϵ is the turbulent energy dissipation rate. The constants in Eqs. 3.7, 3.8 and 3.9 take the values given in Table 3.1.

For wave driven orbital motion, the two equation turbulence models (such as $k-\epsilon$ model) will become unstable under some conditions. From the authors' experience, when the wave is strong or the wave is breaking, instabilities will be observed. Mayer and Madsen (2000) carried out analytical stability analysis to investigate the erroneous behavior of the turbulence model ($k-\omega$ model in their case) under waves. It turns out that the turbulent eddy viscosity will grow unbounded and therefore make the model unstable. It seems that no general purpose turbulence model has been developed especially for unsteady wave driven flows. Most models rely on the tuning of empirical parameters. For the numerical code used in this research, the values of turbulence parameters are bounded when they grow out of range (e.g., k and ϵ become negative). Fortunately, for all the test cases considered in this work, instability of the turbulence model did not arise. The modified two-equation turbulence model for wave flows proposed by Mayer and Madsen (2000) or other modified models can be used when the wave is strong or even breaking and instabilities are expected.

3.2.3 Sediment Transport Model

The scour problem is caused by the erosion movement of sediment. In this numerical model, both bed load and suspended load are considered. Exner equation is used to update the bed elevation (García 1999).

Bed Load Transport

There are many bed load transport rate formulas in the literature. Most of them relate bed load transport rate with shear stress. The formula of Engelund and Fredsøe (1976) is chosen for the current model

$$q^* = \begin{cases} 18.74(\theta - \theta_c)\left[\theta^{1/2} - 0.7\theta_c^{1/2}\right] & \text{if } \theta > \theta_c \\ 0 & \text{otherwise} \end{cases} \tag{3.10}$$

where q^* is a dimensionless bed load transport rate known as the Einstein number which is given by

$$q^* = \frac{q_0}{\sqrt{Rgdd}}$$

Here q_0 is the bed load transport rate for flat bed. θ and θ_c are the Shields number and the critical Shields number for initiation of motion respectively, where θ is defined as:

$$\theta = \frac{\tau_b}{\rho g R d}$$

Here τ_b is the bed shear stress calculated with the fluid flow model, ρ is the density of water, g is the gravitational acceleration, R is the submerged specific gravity of sediment(=1.65 for quartz) and d is the sediment grain diameter.

The critical Shields number for particular sediment is given for flat bed and should be adjusted according to the local slope of the bed and local shear force direction. The critical Shields number for a flat bed, θ_{c0}, is a function of flow intensity and sediment properties. θ_{c0} is given as a constant in most numerical models. The approach used here to account for the slope effect is similar to that

used by Roulund et al. (2005). It considered the slope effect and followed the approach suggested by Engelund and Fredsøe (1976) to use the flow velocity at the particle position and the steepest slope to adjust the critical Shields number. In this research, the shear stress vector, instead of velocity near the bed, is used. Fig. 3.1 shows the scheme employed for the adjustment of the bed shear stress, where **n** is the surface normal vector, **R** is the steepest-slope unit vector, and τ is the wall shear stress vector acting on the bed. The critical Shields number is adjusted according to

$$\theta_c = \theta_{c0}\left(\cos\beta\sqrt{1-\frac{\sin^2\phi\tan^2\beta}{\mu_s^2}}-\frac{\cos\phi\sin\beta}{\mu_s}\right) \tag{3.11}$$

where ϕ is the angle between the velocity vector and the bed steepest slope direction, β is the slope angle of the bed. μ_s is the static friction coefficient and has the value of 0.63 for this work. From Eq. 3.11, when the wall shear stress tries to move sediment up slope, the critical Shields number θ_c increases, and vice versa.

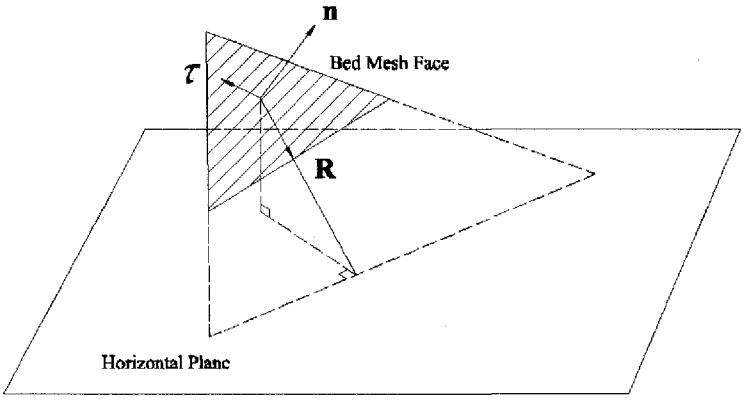

Figure 3.1: Slope Effect on Sediment Transport

Eq. 3.10 only gives the total bed load. The bed load transport rates in different directions are given by

$$q_i = q_0\frac{\tau_i}{|\tau|} - C|q_0|\frac{\partial\eta}{\partial x_i}, i = 1,2 \tag{3.12}$$

where η is the bed elevation, C is a constant in the range of 1.5-2.3 which is used to reflect the slope effect on the sediment flux (Brørs 1999).

Suspended Load

The governing equation for suspended load is a standard convection diffusion equation. Sediment must be fine enough to ignore the inertial effect of the particle.

$$\frac{\partial c}{\partial t} + \nabla \cdot (\mathbf{u} - v_s \frac{\mathbf{g}}{|\mathbf{g}|})c = \nabla \cdot (\nu_t \nabla c) \tag{3.13}$$

Here c is the sediment concentration, $\mathbf{u}$ is fluid velocity vector, v_s is sediment fall velocity. ν_t is the diffusivity which is taken as the same value as turbulence eddy viscosity.

Bed Morphology Model—Exner Equation

Bed elevation changes are based on the continuity of sediment. The Exner equation, which describes the sediment continuity, is

$$\frac{\partial \eta}{\partial t} = \frac{1}{n-1}[-\nabla \cdot \mathbf{q}_b + D - E] \tag{3.14}$$

where η is the bed elevation, n is the porosity of the bed, $\mathbf{q}_b$ is the bed load transport rate vector whose components are given by Eq. 3.12. D is the deposition rate and E is the entrainment rate. The deposition rate D at the bed is

$$D = v_s c_b \tag{3.15}$$

where c_b is the sediment concentration very near the bed. In the current model, the concentration at the nearest cell center is used. The entrainment rate E, unlike the deposition rate D, needs some empirical model. E can be written in dimensionless form as

$$\widetilde{E} = \frac{E}{v_s} \tag{3.16}$$

Many models are available in the literature for estimating the entrainment rate of sediment into suspension $\widetilde{E}$. García and Parker (1991) performed a detailed comparison of eight such relations

Table 3.2: Sediment Entrainment Models

Authors	Model	Parameters
García and Parker (1991)	$\widetilde{E} = \frac{AZ_u^5}{1+\frac{A}{0.3}Z_u^5}$	$A = 1.3 \times 10^{-7} \quad Z_u = \frac{U_{*s}}{v_s} R_{ep}^{0.6}$
van Rijn (1984)	$\widetilde{E} = 0.015 \frac{d_{50}\Psi^{1.5}}{Z_b D_*^{0.3}}$	$D_* = d_{50}\left[\frac{R-1}{g}\mu^2\right]^{1/3} \quad \Psi = (\frac{\theta}{\theta_c} - 1)$
		$Z_b = 0.05H$
Smith and McLean (1977)	$\widetilde{E} = \frac{0.65\gamma_0\left(\frac{\theta}{\theta_c}-1\right)}{1+\gamma_0\left(\frac{\theta}{\theta_c}-1\right)}$	$\gamma_0 = 2.4 \times 10^{-3}$

against data. Three of the many existing sediment entrainment models are listed in Table 3.2. The entrainment rate is given at some reference level Z_b very near the bed to avoid singularity. The reference level in García and Parker (1991) is five percent of the water depth from bed while in Smith and McLean (1977), the reference level is defined as

$$Z_b = 26.3\left(\frac{\theta}{\theta_c} - 1\right) d + k_s \tag{3.17}$$

where k_s is the equivalent roughness height of the bed.

All of these three empirical models in Table 3.2 all perform well against data (García and Parker 1991). In this work, the model in van Rijn (1984) is used. Some simpler models for E also exist in the literature. Brørs (1999) and Liang et al. (2005) used the concept of turbulence diffusivity and set the vertical sediment entrainment flux as $E = -\sigma_t \frac{\partial C}{\partial y}$. This formula will simplify the numerical model while still give reasonable results.

3.2.4 Mesh Deformation Solver—Laplacian Equations

As mentioned before, the automatic mesh deformation is implemented by a Laplacian smooth operator. Governing equations for the mesh motion equation is the Laplacian equation (Jasak and

Tuković 2007). Let **v** be the grid motion velocity field, then the equation becomes

$$\nabla \cdot (\gamma \nabla \mathbf{v}) = 0 \tag{3.18}$$

where γ is the diffusion coefficient chosen to control the mesh motion. γ can be a constant or a variable defined by other properties in the domain. The selection of variable γ depends on the specific mesh motion problem and needs objective judgment. Jasak and Tuković (2007) suggested several possibilities to set the γ value based on distance (linear, quadratic and exponential) from some boundary or mesh characteristics (orthogonality and skewness). These methods all have their merits and shortcomings. In this work, γ is set as a non-zero constant for simplicity. The boundary condition for Eq. 3.18 is given by the Exner equation. After each time step of bed elevation change, the bed grid motion velocity is known. When the grid motion velocity field is solved, the grids in the whole domain can be moved based on the following equation

$$\mathbf{x}^{k+1} = \mathbf{x}^k + \mathbf{v}\Delta t \tag{3.19}$$

Here, $\mathbf{x}^{k+1}$ and $\mathbf{x}^k$ are grid position vectors at time level $k+1$ and k respectively, and Δt is the time step.

Fig. 3.2 is a simple test case for the mesh deformation component of the numerical model. The bottom of a rectangular flume (with unstructured grid) is "vibrating" in a sinusoidal mode with a period $T = 0.8$ s. Mesh grids at $t = 0$, $T/4$, $T/2$ and $3T/4$ are shown. In real cases, the bed will move in a more complicated way.

3.3 Numerical Simulation Schemes and Procedures

The governing equations presented in the previous section form a strongly coupled system of equations. The solution of this system of equations needs some effort because even for each single component (fluid, free surface or sediment) is a difficult problem. Also the time scales of

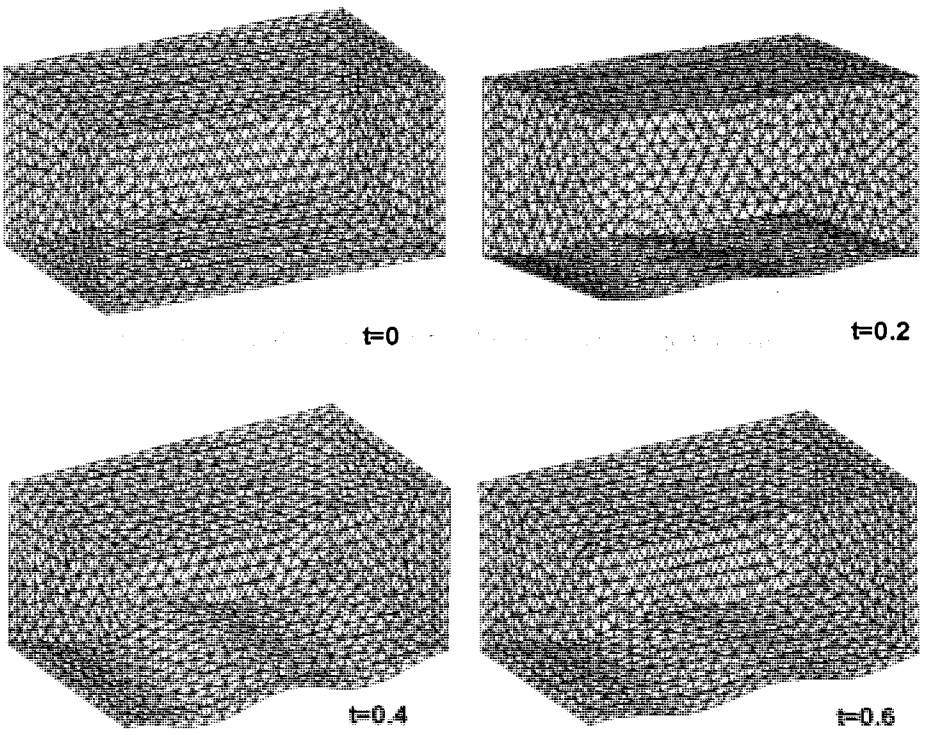

Figure 3.2: Mesh Deformation of Vibrating Flume Bottom

the flow field and sediment transport are so largely different that the whole system is very stiff. Consequently, numerical instabilities can be expected to arise. The emphasis of this research is not on the numerical details but on building a numerical model for the local scour problem and verification of the numerical solution of the model. So numerical schemes for each component of this system are described only briefly. Several references about these numerical schemes are provided for the interested readers.

The code used in this work is an open source computational fluid dynamics (CFD) code named OpenFOAM (OpenCFD 2006). It is freely available through internet. OpenFOAM is primarily designed for problems in continuum mechanics. It uses the tensorial approach and object oriented techniques (Weller et al. 1998). OpenFOAM provides a fundamental platform to write new solvers for different problems as long as the problem can be written in tensorial partial differential equation form. Here, the flow field is solved by the adaption of the original turbulence solver for incompressible fluid. The sediment transport equation and bed deformation are added to the fluid flow solver to form a new solver called FOAMSCOUR. The core of this code is the finite volume discretization of the governing equations. Almost all kinds of differential operators possible in a partial differential equation, such as temporal derivative, divergence, laplacian operator, curl, etc, can be discretized in the code. The finite volume details of the code can be found in Jasak (1996). The next section is a brief introduction of the numerical scheme used in FOAMSCOUR.

3.3.1 Numerical Scheme for the Flow Field

The numerical solution of the Navier-Stokes equation for incompressible fluid flow imposes two main problems (Jasak 1996): the nonlinearity of the momentum equation and the pressure-velocity coupling. For the first problem, two common methods can be used to deal with it. The first is to solve a nonlinear algebraic system after the discretization. This will need a lot of computational effort. The other is to linearize the convection term in the momentum equation by using the fluid velocity in previous time steps which satisfies the divergence-free condition. The latter method is used in this research. For pressure-velocity coupling, many schemes exist, such as the semi-

implicit method for pressure linked equation (SIMPLE) (Patankar 1981) and pressure implicit splitting of operators (PISO) (Issa 1986). PISO scheme is used in this code. For the $k-\epsilon$ turbulence model equations, although k and ϵ equations are coupled together, they are solved by a segregated approach, which means they are solved one at a time. This is also the usual approach used in most CFD codes.

For the free surface, CICSAM scheme is easy to code and captures the free surface fairly well. But the problem with this scheme is that it is very slow. The time step required is so small that the computation usually takes a very long time even for a small computational domain. This is partially caused by the fact that the control cell which has the largest Courant number usually is in the air phase. In our case, the two phases are water and air. The density of water is almost 1000 times larger than that of air and the velocity magnitude in the air phase is far greater than in the water phase. A modified approach is proposed in this work analog to those used in other CFD codes. The aim is to relax the time step requirement while capturing the free surface. In the modified approach, the volume occupied by the air phase can be called *void*. In the *void* region, the velocity is set to zero and the pressure is set to atmospheric pressure. This will not upset the computations because of the large density ratio between water and air. The inertia force associated with air can thus be neglected. The threshold value of α for the *void* (i.e., below what value of α, it can be viewed as *void*) needs some consideration. The classical dam break problem is carried out to investigate the effect of the threshold value. As in Fig. 3.3(a), a column of water is released at time $t = 0$ s and an obstacle is located in front of the water column. Fig. 3.3 shows the contour of the VOF scalar α which is the volume fraction of water. The results at $t = 0.3$ s for different threshold values (0.01 and 0.1) are plotted together with the original scheme (threshold value equals 0). The result from threshold value 0.01 is very close to the original scheme while that from threshold value 0.1 causes more damping of the water flow. This is because high threshold values imply that a larger portion of the flow field is set to zero velocity and the water needs to consume more energy to go through such area. In this work, a threshold value 0.01 is used for all computations and the computational time is reduced by almost half.

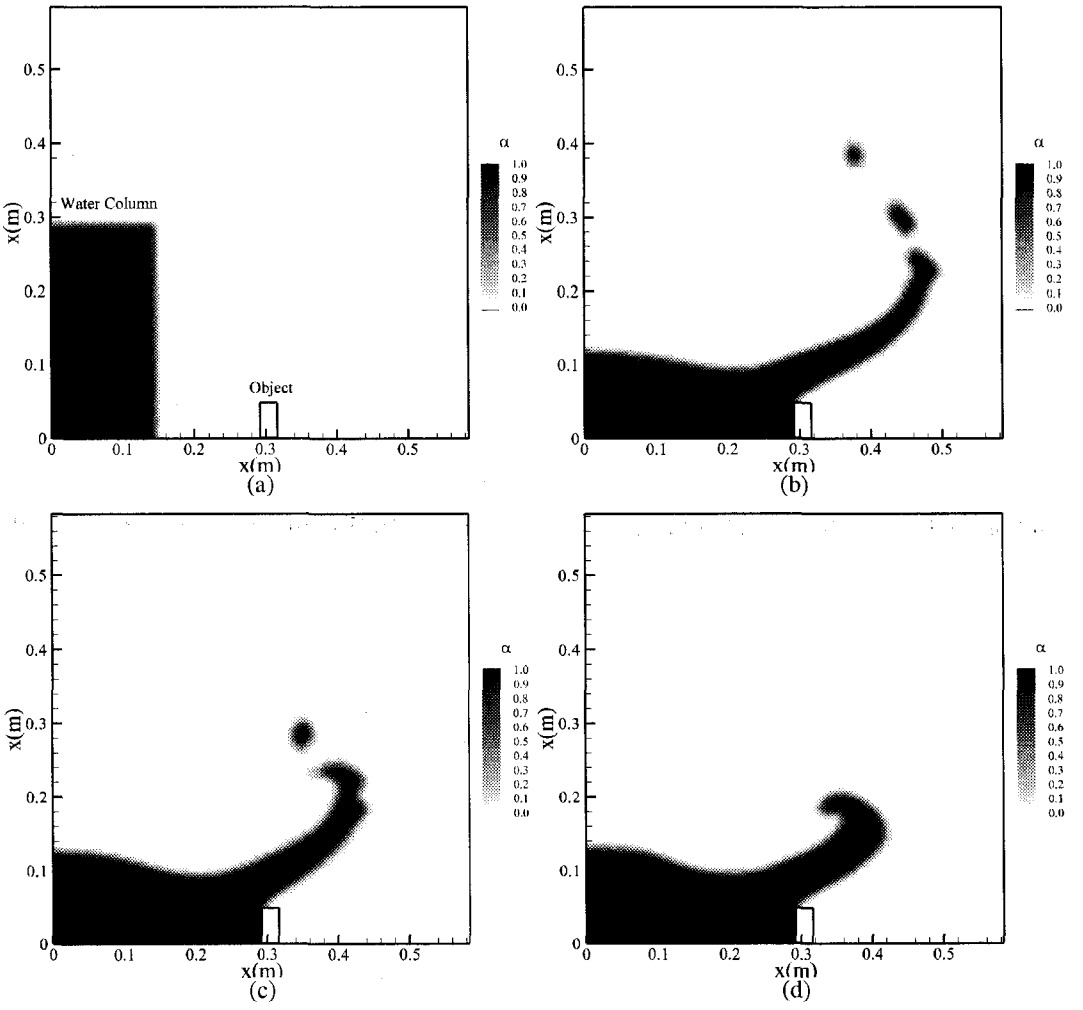

Figure 3.3: Test Cases for Modified CICSM Scheme (a) Initial state (b) Critical $\alpha = 0$ (c) Critical $\alpha = 0.01$ (d) Critical $\alpha = 0.1$

3.3.2 Numerical Scheme for the Sediment Transport

The bed load and suspended load in the sediment transport modules are solved separately. Since the shear stress on the bottom is obtained from the flow solver, using Eq. 3.10 to calculate the bed load is straightforward. The suspended load equation (Eq. 3.13) is a convection-diffusion equation and the sediment is transported passively by the flow field. Finite volume method is also used to solve this equation.

After the sediment load (namely bed load and suspended load) is calculated, the Exner equation is solved to change the bed elevation. Exner equation is a 2D equation although the bed is in 3D space. This is because the vertical coordinate z is the variable to be solved and it is not an independent variable any more. The bed elevation change is due to the divergence of sediment transport flux together with erosion and deposition of sediment on the bed surface. This simple 2D equation can usually be solved by the finite difference method using a structured grid when the bottom has a regular shape (Beek and Wind 1990; Olsen and Melaaen 1993; Brørs 1999; Olsen and Melaaen 1999). For complex domains, such as a natural river bottom or in the presence of objects (bridge piers, break water etc.), a finite volume or finite element method can be used with unstructured grids. In this research, two meshes are used. One is for the fluid flow solver and the other is for the bottom Exner equation. The Exner equation is solved on the 2D mesh using finite volume method. In Fig. 3.4, it is shown that the coupled problem is solved through mapping between the fluid mesh bottom boundary and sediment 2D mesh. After the flow solver and turbulence solver are finished, the shear stress and other parameters are available. Those flow parameters are mapped from the 3D fluid bottom boundary to the 2D bed sediment mesh. On the 2D sediment mesh, the Exner equation is solved and the new bed elevation is calculated. Then the bed elevation is mapped back from 2D sediment mesh to 3D fluid mesh. The 3D fluid mesh is deformed according to this as a boundary condition. The use of separate meshes for the flow field and the Exner equation keeps the concept clear and easy to manage in the code. Mapping back and forth between these two meshes could lead to loss of some accuracy when averaging and

interpolation are needed. But when the mesh is sufficiently fine or the mapping is almost one to one, accuracy is not a problem.

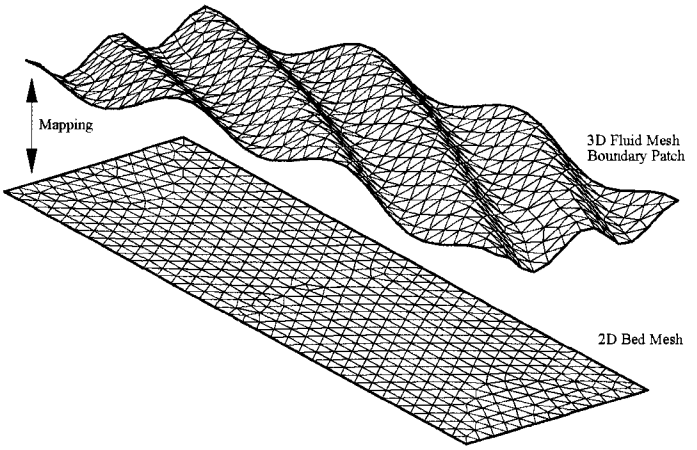

Figure 3.4: Mapping between 3D and 2D Bed Mesh

3.3.3 Numerical Scheme for Automatic Mesh Deformation

The Laplacian equation in Eq. 3.18 needs to be solved on the 3D mesh to get the movement of each node. Finite element method (FEM, which is implemented in the original OpenFOAM package), the finite volume method as well as other numerical methods can be used. In the original OpenFOAM package, each cell of the 3D mesh is decomposed into tetrahedral elements and the new refined mesh is used to solve the Laplacian equation. The details of the FEM implementation can be found in OpenCFD (2006) and Jasak and Tuković (2007). This built-in FEM method is very slow especially when the 3D mesh is very big. Numerical tests show that the decomposition time is almost half that of total mesh motion solution step. Also the decomposition makes the new mesh much larger (usually several times the original mesh size) and therefore makes the computation even longer. In this work, some simplifications are made according to the unique character of the problem under consideration. For the scour problem in this work, the specific characteristic is that the sand bed boundary movement is in the vertical direction (deposition or erosion). This makes

the problem relatively simpler. A new finite volume solver for the Laplacian equation is written and it is used on the 3D fluid mesh. No mesh decomposition is used and the mesh movement is solved at the cell centers. After those center values are obtained, they are interpolated to the grid points to perform the actual mesh motion.

3.3.4 Boundary Conditions

There are basically five boundary types of the domain: inlet, outlet, atmosphere, walls and sand bed. For sediment transport, the boundary conditions for suspended sediment concentration and bed load feeding rate also need to be specified.

Inlet and Outlet

For the inlet, velocity is specified. Pressure is set to be zero normal gradient $\partial p/\partial \mathbf{n} = 0$ to be consistent with velocity condition. Turbulence quantities such as k and ϵ are also set as constant (5% turbulence intensity is used to set the turbulence level). The outlet condition is chosen as zero gradient for all quantities except for the pressure. At the outlet, the dynamic pressure $P_{dynamic} = 1/2\rho u^2$, instead of total pressure (P_{total}), is specified as zero normal gradient. The hydrostatic pressure P_{static} is subtracted from the total pressure. This makes it easy to specify the pressure boundary condition since the free surface will change and the hydrostatic pressure will also change at the outlet. The details of the outlet free surface condition can be found in OpenCFD (2006).

Atmosphere

The top boundary of the domain is the atmosphere and the total pressure is set to zero. k and ϵ at the top boundary will depend on the flow direction relative to the boundary. When the flow is going out of the domain, then zero gradient condition is used. When the flow is going into the domain, a 1% turbulence intensity is used to specify k and ϵ. The small amount of air turbulence will not affect the water flow field too much since the water is much heavier than air.

Walls and Sand Bed

At the surfaces of objects (such as pile, sluice gate and flume walls), wall boundary conditions are used. No-slip condition $\mathbf{u} = 0$ is set for velocity with zero normal gradient for pressure. For the turbulence quantities, it will depend on the smoothness/roughness of the wall. For smooth walls, the value of turbulent kinetic energy k has to be specified, while for rough and transitional cases, normal gradient of k is set equal to zero . For the test cases in this work, the walls are all rough and zero normal gradient condition is used for k. Test cases using zero normal gradient k condition give numerical results which are in better agreement with experiments (Roulund et al. 2005). The bed boundary is almost the same as the walls. One exception is that the vertical velocity is set to be the same as the bed elevation change velocity. This adjustment is particularly important in the early stages of scour and the scour rate is very high. In the later stages, the scour is almost at equilibrium and the vertical velocity of the movable bed is very small compared to that of the flow field. At this stage, it is reasonable to set the bed fluid velocity equal to zero.

Sediment Boundary Conditions

At the inlet, the suspended sediment concentration c is set to zero which corresponds to clear water coming into the domain. At the outlet, zero gradient is applied for c. At the atmosphere boundary, c is set to zero since no sediment particle will go through the water surface. For the solid walls, the flux of sediment through these surfaces is zero. The flux of suspended sediment $\mathbf{q}_s$ (including convective and diffusive fluxes) is defined as

$$\mathbf{q}_s = \left(\mathbf{u} - v_s \frac{\mathbf{g}}{|\mathbf{g}|}\right) c - \nu_t \nabla c \tag{3.20}$$

So the condition for zero flux of suspended sediment through the wall is expressed as

$$\mathbf{q}_s \cdot \mathbf{n} = 0 \tag{3.21}$$

At the sand bed, the suspended sediment flux is specified as the net upward normal flux

$$\mathbf{q}_s \cdot \mathbf{n} = E - D \tag{3.22}$$

where D is defined in Eq. 3.15 and E is calculated by using the empirical model by van Rijn (1984) as shown in Table 3.2.

Bed load boundary conditions are defined similarly. At the inlet, bed load is set to be zero which corresponds to zero feeding rate because of the concrete bed before flow hits the sand bed (see the test case section). At the outlet, zero gradient is applied. At the wall surfaces, the bed load flux is set to zero as for suspended load, i.e.

$$\mathbf{q}_b \cdot \mathbf{n} = 0 \tag{3.23}$$

3.3.5 Simulation Flow Chart

The flow chart for the simulation process is plotted in Fig. 3.5. A quasi-steady approach is used in the model. In this approach, it is assumed the time scale of bed change is far larger than that of flow field and the time steps for flow field and morphological calculations are different. When the flow field is being calculated, the domain boundaries are fixed. Only at the sediment transport step, the domain boundaries are adjusted. A scheme similar to the method proposed by Liang et al. (2005) is used here. During the simulation, m time steps of flow field simulation are carried out between the morphological steps. This approximation is only valid when the bed changes are very slow when compared to the flow changes. Through numerical experiments, it is found that at the beginning of the local scour process, the bed changes very rapidly and most of the scour occurs in this stage. In order to increase the accuracy, smaller values of m are used at the beginning of the simulation. After the flow field and bed change reach relatively steady state, bigger values of m can be used to accelerate the computation. In the test cases considered here, $m = 1$ is used at the initial stage of simulation and m gradually increases to 100 when the whole system tends

to equilibrium. There are some differences between the current time marching scheme and the one in Liang et al. (2005). Liang et al. (2005) only use k, where $k < m$, time steps between morphological steps and assume that from time step $k+1$ to m, the flow field does not change much. The flow field from time step k is used to perform the morphological calculation. This will further reduce the computational time.

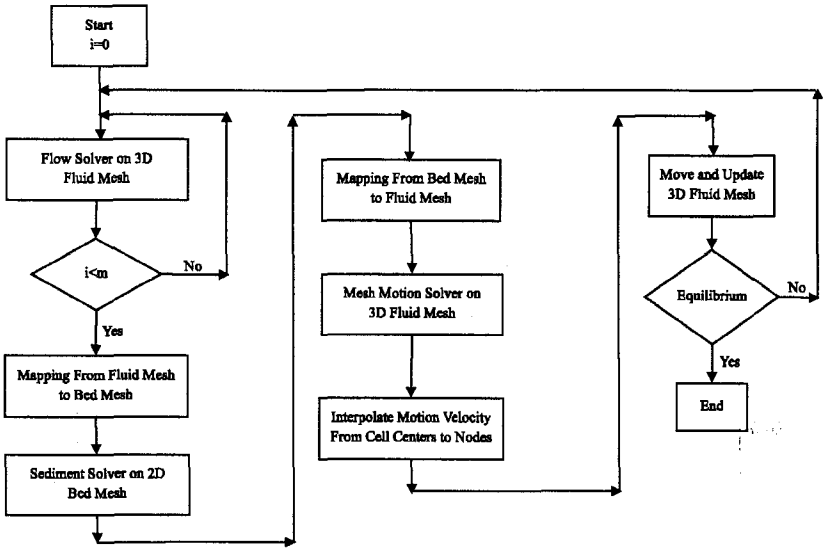

Figure 3.5: Flow Chart of Computational Scheme

3.4 Model Verification and Applications

In this section, applications of turbulent wall jet scour (2D case) and wave scour around a large vertical circular cylinder (3D case) are carried out using FOAMSCOUR and the numerical results are compared with experiments. In turbulent wall jet scour process, the jet flow and momentum diffusion are of interest as both have an impact on the scour hole development. In wave scour around a large pile, the water wave and its interaction with the pile and bed sediment are important. The coupled problems of flow field and morphodynamics usually take a very long time for computation. Parallel computation with domain decomposition is used to accelerate the process. OpenFOAM comes with parallel computing support and FOAMSCOUR easily uses these mod-

ules to implement both flow field solver and sediment transport solver. All computations were done on the National Center for Supercomputing Applications (NCSA) Tungsten Xeon Cluster at the University of Illinois at Urbana-Champaign.

3.4.1 Wall Jet Scour Test Case

The experimental data of turbulent wall jet scour by Chatterjee and Ghosh (1980) and Chatterjee et al. (1994) are used. This experiment investigated the flow field and sediment transport due to a submerged wall jet. The schematic view of the experiment is shown in Fig. 3.6. The jet is formed by a small opening under a sluice gate and flows over a rigid apron onto an erodible bed. The details of the experiment can be found in the original papers. Run2 of the experiment is chosen as a typical run to be simulated. The bed material is sand with d_{50} = 0.76 mm, submerged specific gravity 1.65, porosity 0.43 and angle of repose 29 degrees. The flow condition for this run is as follows. The apron length is 0.66 m and the jet inlet velocity is 1.56 m/s. The downstream water depth is controlled to be 0.291 m by the outlet weir. In the experiment, the jet inlet velocity is caused by the difference between upstream and downstream water depth. The corresponding water depth difference in Run2 is 0.118 m. But in this simulation, the conditions upstream of the sluice gate are not modeled. Equivalently, velocity is specified at the jet inlet. Although the test case is 3D, the flume side walls have little effect on the main region of the flow and the scour profile is almost uniform in the span wise direction.

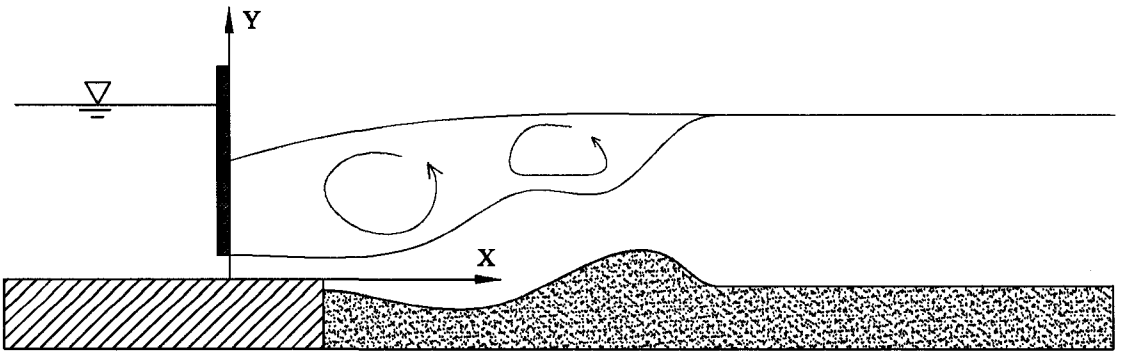

Figure 3.6: Turbulent Wall Jet Scour Schematic View

In Fig. 3.7, free surface and velocity magnitude contours at equilibrium state are plotted. When the jet flow starts, it induces water waves in the domain. After the flow calms down, the free surface keeps an almost steady position. The free surface at the equilibrium state is almost flat except in the region of maximum scour. The velocity magnitude contours show that the jet flow comes into the domain through the small opening and after momentum diffusion and water entrainment it leaves the domain through free fall over the outlet weir.

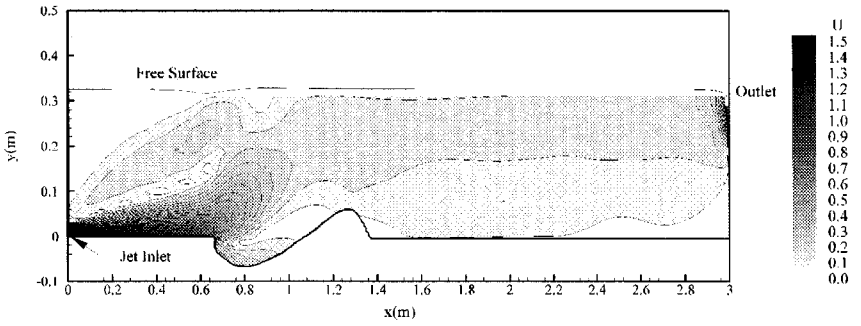

Figure 3.7: Numerical Results for Turbulent Wall Jet Flow Field and Free Surface

The stream trace in the region of jet opening and scour hole at equilibrium state is plotted in Fig. 3.8. The flow pattern is more clearly shown. The jet induces strong flow re-circulation and just above the jet inlet, there are some small circulation areas which are isolated from the main flow. Inside the scour hole, the stream trace lines show another circulation pattern. These flow patterns are closely related to the scour process. When the water leaves the jet orifice, the main physical processes are the momentum diffusion and entrainment of water from above into the jet flow. As a result, the magnitude of the maximum velocity and also the velocity distribution will be

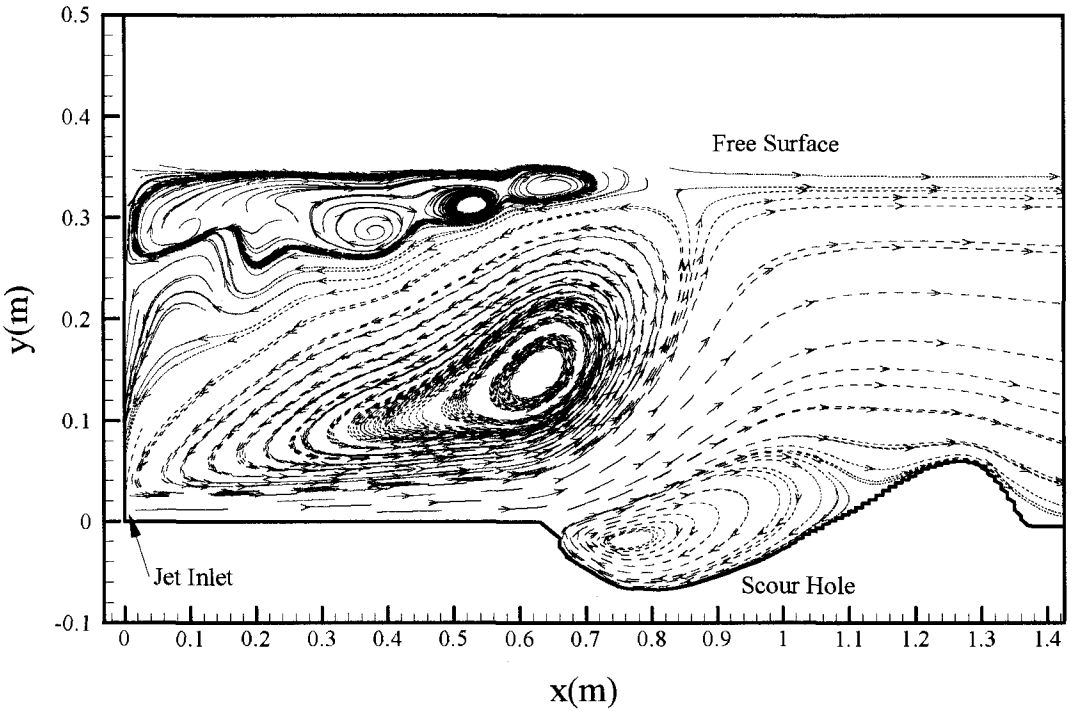

Figure 3.8: Numerical Results for Turbulent Wall Jet Flow Stream Trace

changed. This change is a complicated function of flow domain geometry and sediment properties (Chatterjee and Ghosh 1980). In Fig. 3.9(a), the maximum horizontal velocity normalized by jet inlet velocity is plotted against the non-dimensionalized x distance where B_0 is the jet opening width. The wall jet momentum diffusion characteristics found in experiment are reproduced well by the numerical simulation. As in the experiment, the diffusion process is slower in the rigid apron region than in the erodible bed region. In the near jet opening region, the numerical results are very close to the experimental data. But in the far down stream region, the momentum diffusion is over estimated by the numerical simulation, i.e., the maximum velocity is smaller and the velocity distribution in the vertical direction is more uniform. This may come from the numerical diffusion nature of the schemes used in this test case.

Wall jet flow near the jet opening can be divided into two regions. One is the inner boundary layer region and the other is the outer shear layer region. When the boundary layer meets the shear layer, the potential core will disappear and the jet flow is fully developed (Rajaratnam 1976). The

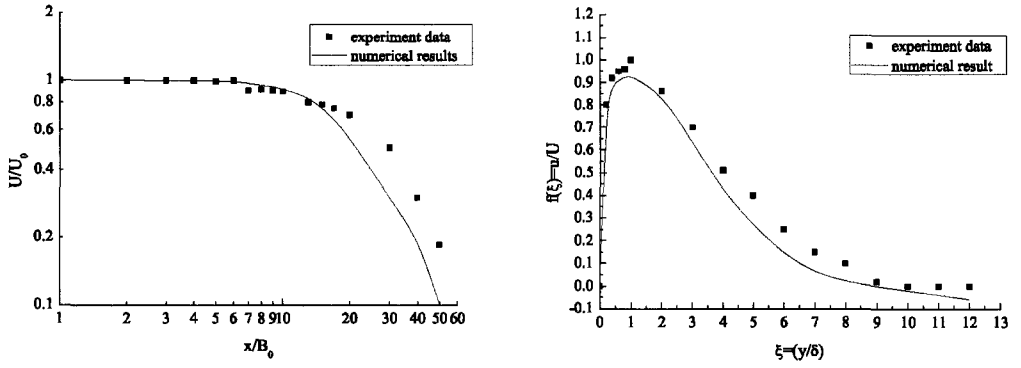

(a) (b)

Figure 3.9: Turbulent Wall Jet Characteristic: (a) Jet Diffusion along x-Axis (b) Velocity Distribution at x=0.6m

horizontal velocity at location x = 0.6 m downstream of the jet opening is plotted in Fig. 3.9(b). In Fig. 3.9(b), ξ is defined as y/δ, where δ is the vertical distance from the wall to location of the maximum horizontal velocity. Non-dimensionalized velocity is plotted as a function of ξ. From Fig. 3.9(b), the numerical simulation predicted the velocity distribution fairly well.

Fig. 3.10 shows the mesh development from the initial flat bed condition to the equilibrium configuration. The unstructured mesh is composed of three layers of fine quadrilateral cells in the boundary layer on the bottom and triangle cells elsewhere. With the change of bottom elevation due to scour and deposition, the computational domain gradually deforms while the unstructured mesh remains valid. There is a small artificial step at the transition point between the concrete apron and the sand bed. It has a depth of 5 mm. This small step is used to improve the mesh quality because the scour hole will make the cells in front of the transition point vertically stretched. Inside the small step, several mesh cells are introduced making the simulation stable.

Scour profiles from numerical simulation at different times are plotted in Fig. 3.11 as solid lines together with the experimental results. The time required to get to equilibrium state is almost one hour for this test case. Fig. 3.12 shows the time development of the maximum scour and deposition. At equilibrium state, according to the numerical simulation results, the maximum

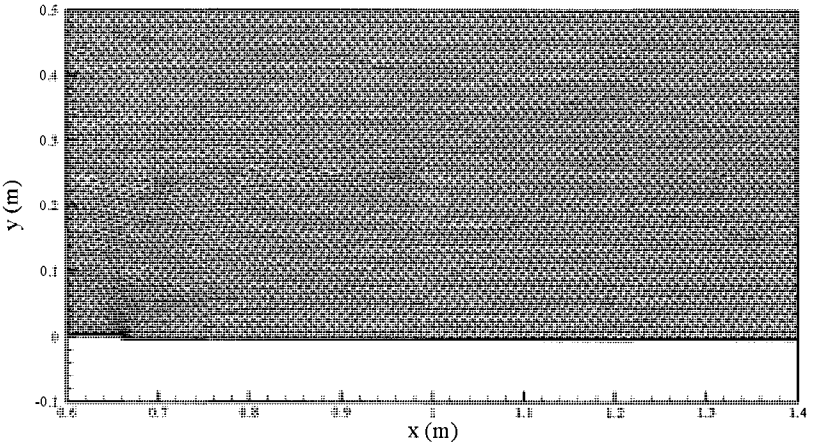

(a)

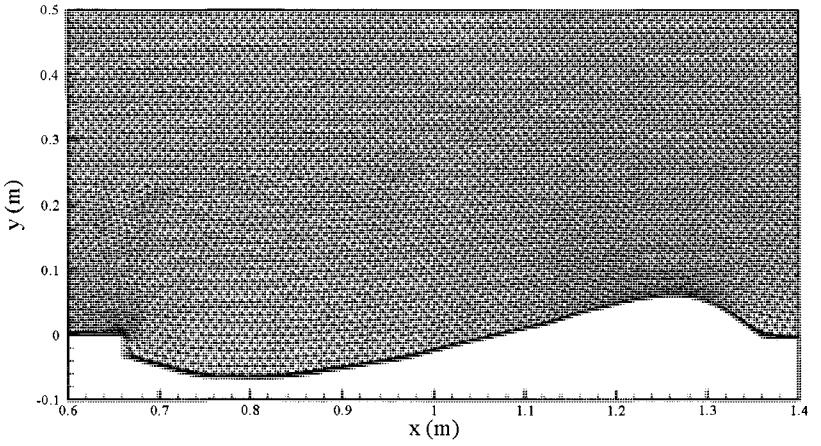

(b)

Figure 3.10: Turbulent Wall Jet Scour Mesh Deformation: (a) Initial (b) Equilibrium

scour depth is about 0.63 m and the maximum deposition depth is about 0.4 m. These fit well with the observations made in the experiment. From Fig. 3.12, the scour process occurs very rapidly in the early stage while at later stage, the profile changes very slowly. The maximum scour position and the peak of the sediment deposition dune move very slowly downstream.

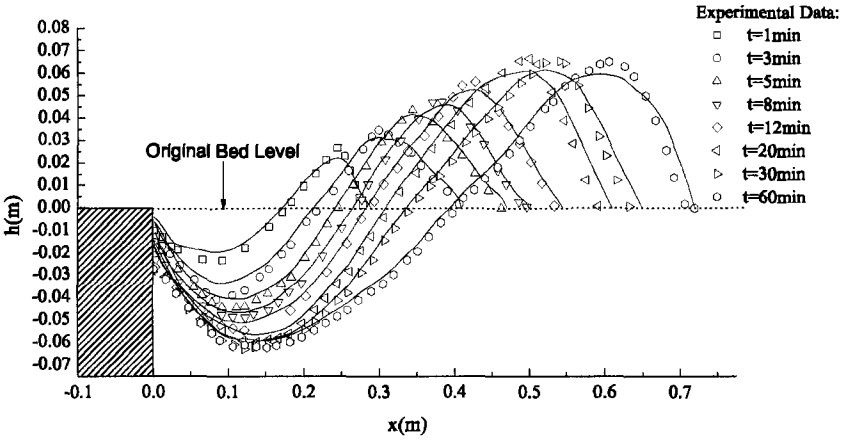

Figure 3.11: Wall Jet Scour Profile

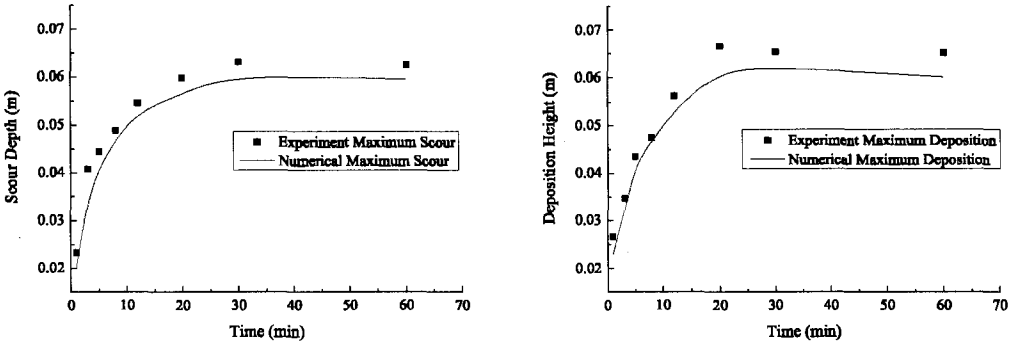

(a) (b)

Figure 3.12: Wall Jet Maximum Scour and Deposition Development with Time: (a) Maximum Scour (b) Maximum Deposition

In Fig. 3.13, the Shields number at equilibrium state is plotted. Chatterjee and Ghosh (1980) gave an estimation of critical shear stress along the bed using von Karman's integral theorem. But

there is a discrepancy between this estimation and the critical shear stress using Shields method. This discrepancy could be due to the non-hydrostatic pressure distribution, non-uniformity of the grain size or the pressure differential recorded by the Preston tube used in the experiment. Thus in Fig. 3.13, only numerical results for shear stress are plotted. The Shields number (shear stress) decreases with the distance from the jet opening. This is in agreement with the experiment. The maximum Shields number occurs near the transition point between the concrete apron and the sand bed. At equilibrium state, the Shields numbers along the bed are all below the critical Shields number which means that no sediment is moving.

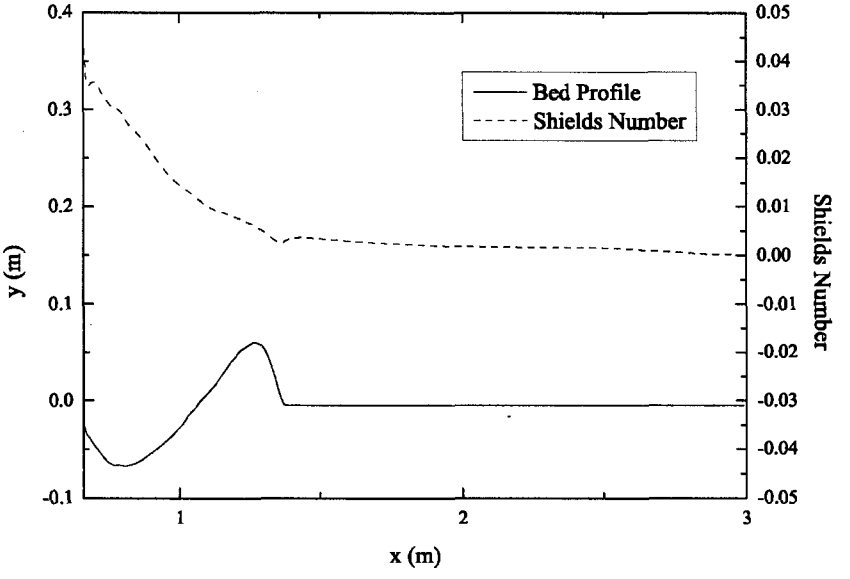

Figure 3.13: Bed Shear Stress Distribution at Equilibrium for Wall Jet Scour

3.4.2 Wave Scour Around a Large Vertical Circular Cylinder

Scour process around vertical pile caused by wave is more complicated because of the 3D nature of the problem. The free surface of water wave and 3D scour hole around the pile make it a good test case for the application of the solvers presented above. The test case uses the experimental

data obtained by Sumer and Fredsøe (2001). The schematic view of the experiment is shown in Fig. 3.14. Test case 7 of the experiment is used in this work. In this case, the wave has a period of 3.5 s, wave height of 6.4 cm, wave length of 6.79 m and Keulegan-Carpenter (KC) number of 0.61. The pile has a diameter of 1 m and the sand has d_{50} = 0.2 mm.

The mechanism causing the scour around a vertical pile can be different under different conditions. Flow regimes change when the dimensionless number KC (Keulegan-Carpenter number) increases. KC number is defined as

$$KC = \frac{U_m T}{D} \tag{3.24}$$

where U_m is the maximum undisturbed orbital velocity at the bed. When the pile is slender, the scour is primarily caused by vortex shedding ($KC < O(100)$) and by horseshoe vortex ($KC > O(100)$) (Sumer et al. 1992; 1993). For this case, the free surface is of secondary importance and can be replaced by a rigid lid. Numerical simulations using the rigid-lid approximation captured the vortex shedding and horseshoe vortex well and gave good results (Roulund et al. 2005). When the pile diameter is big enough, the scour is caused by the combined effect of phase-resolved component of the wave flow and the steady streaming due to the presence of the large cylinder (Sumer and Fredsøe 2001). For this case, the modeling of the free water surface is very important. Without the free surface, the steady streaming can not be correctly simulated and the scour process can not be captured.

The waves in the experiment are generated by a piston type wave maker and at the end of the wave tank, there is a wave absorber to eliminate wave reflection. The details of the experiment can be found in the original paper. In the numerical simulations, the wave can be generated generally by two approaches: moving mesh (Aliabadi et al. 2003) and wave boundary condition (Mayer et al. 1998). For the moving mesh approach, the piston movement is simulated by moving the boundary of the computational domain. For the wave boundary condition approach, the mesh is fixed but boundary condition on the piston part is given by wave theory. The second approach is adopted in this work. A time varying velocity profile is imposed at the piston boundary to generate the waves

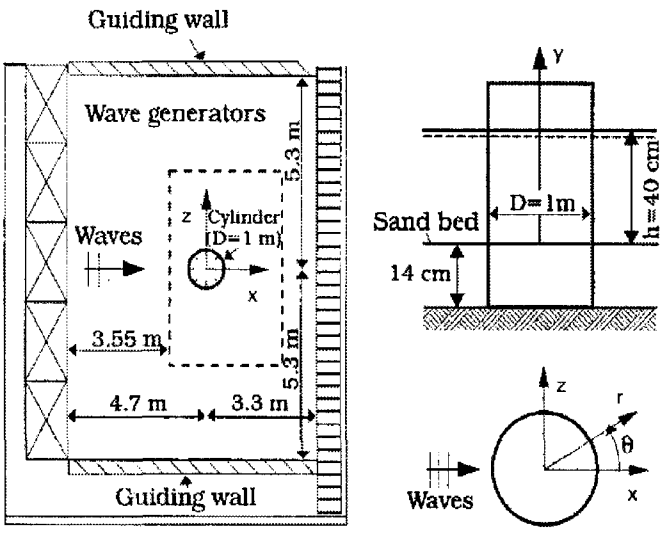

Figure 3.14: Wave Scour around a Large Vertical Circular Cylinder Scheme (After Sumer and Fredsøe (2001) With Permission)

$$\mathbf{U} = f_r(t)\,[\mathbf{U}(y)sin(\omega t + \theta)] \tag{3.25}$$

where $\mathbf{U}$ is the velocity vector at the boundary, ω is the wave frequency, θ is the phase. $\mathbf{U}(y)$ is imposed by the type of the piston. In the test case, the relative depth h/L and wave steepness H/L are about $1/17$ and $1/106$ respectively. The linear wave maker theory applies and for the piston type wave maker in this case, $\mathbf{U}(y)$ is a constant (Dean and Dalrymple 1991). For finite amplitude wave cases, nonlinear effect is important and higher order terms need to be added. $f_r(t)$ is the "ramp" function to start up the piston. $f_r(t)$ has the form

$$f_r(t) = \begin{cases} \frac{t}{T} - \frac{1}{\pi} sin\left(\pi \frac{t}{T}\right) & \text{for } 0 < t < T \\ 1 & \text{for } t > T \end{cases} \tag{3.26}$$

where T is the wave period.

The wave absorber is simulated using a damping zone (or sponge layer). In this damping zone, wave energy is artificially dissipated and wave reflection is minimized. The water depth and fluid

velocity in the damping zone are modified at each time step according to the method proposed in Mayer and Madsen (2000). Two blocks of meshes are used in the computation. One is for the wave tank and the other is for the damping zone which has the length of twice the wave length. The damping zone block has relatively coarse mesh to reduce the computational time. The Coarser mesh in the damping zone also has the effect of numerical dissipation which will make the wave absorber even better. Numerical simulation for Test 1 of the rigid bed experiments in Sumer and Fredsøe (2001) is carried out to test the wave absorber algorithm. Wave profiles in one period are shown in Fig. 3.15 and the reflection coefficient is about 10% which is in the range of laboratory experiment setups.

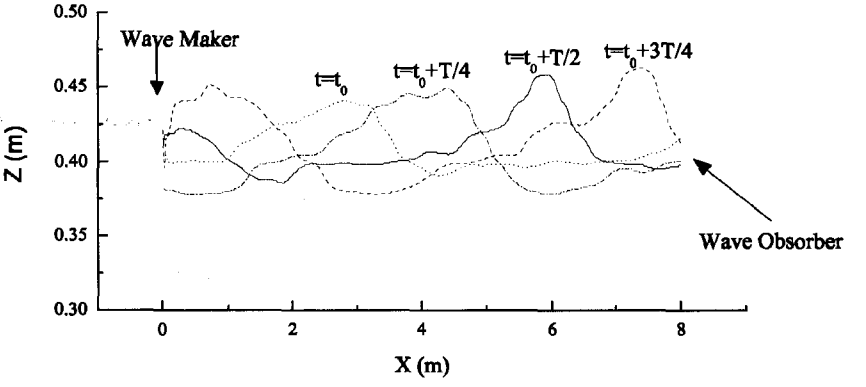

Figure 3.15: Wave Profiles in One Period for Test 1 of Rigid Bed Experiment in Sumer and Fredsøe (2001)

It is shown by the experiment that when a large vertical cylinder is subjected to a progressive wave, the combined effect of incident wave, reflected wave and diffracted wave will create phase-resolved flow and steady streaming. Steady streaming is very important for the mass transport near the bed and therefore the scour process. Steady streaming due to the wave and induced by the presence of cylinder are simulated and compared with the experiment. For the steady streaming due to wave, the Test 1 of rigid bed experiment in Sumer and Fredsøe (2001) is simulated. Fig.3.16 shows the period-averaged velocity profile at the location of the cylinder center (without the cylin-

der in the wave tank). The numerical velocity profile is obtained by averaging the velocity over 30 wave periods. The return flow pattern caused by the wave drift and confined wave tank environment is well captured. The steady streaming near the bed is also captured despite the streaming velocity is lower than the experiment. For steady streaming due the presence of the cylinder, the

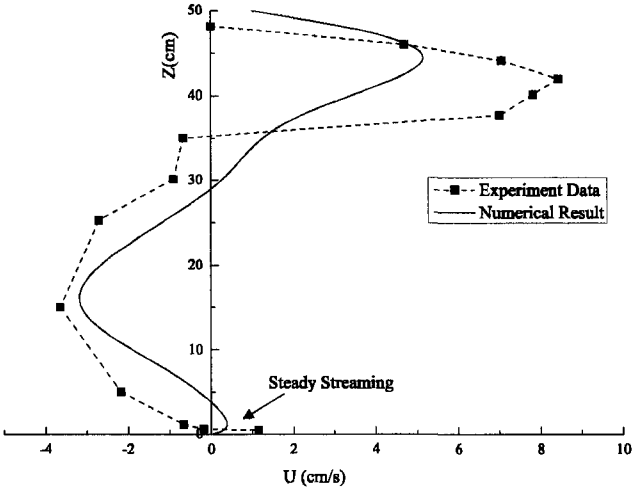

Figure 3.16: Period-Averaged Velocity Profile at the Location of Cylinder Center in Undisturbed Flow

Test 1 of rigid bed experiment in Sumer and Fredsøe (2001) is simulated with the cylinder in the wave tank. Fig. 3.17 shows the period averaged velocity components at point P which is very near the cylinder against the measurement. The radial velocity U_r is in the outward direction over the phase interval from about $\omega t = 150^o$ to 360^o which is in agreement with experiment. The tangential velocity U_θ shows a steady streaming in the opposite direction of wave propagation since the negative tangential velocity experiences a longer period of time.

Fig. 3.18 shows an instantaneous free surface of the wave. A probe point (x = 5.7 m, y = 0.2 m, z = 5.3 m) is also indicated in the figure. Fig. 3.19 shows the pressure change with time at the probe location. During the first several time periods, the wave is under development and the pressure has some noise. But when the wave is fully developed, the pressure is undergoing periodical changes as expected.

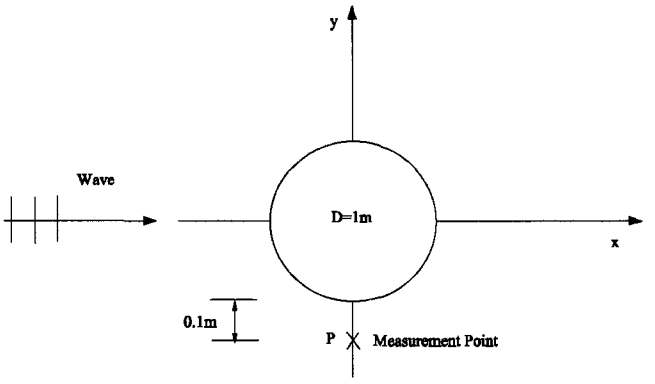

(a)

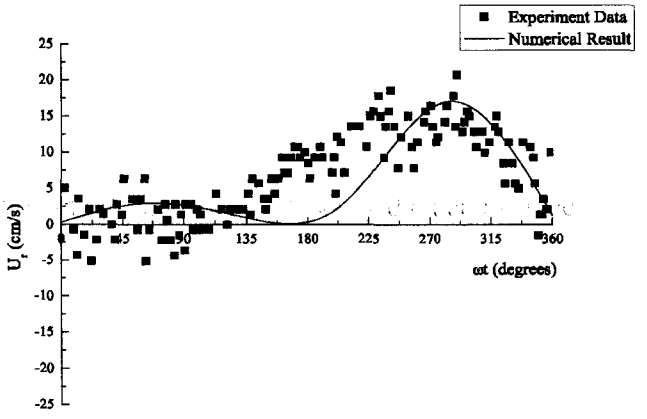

(b)

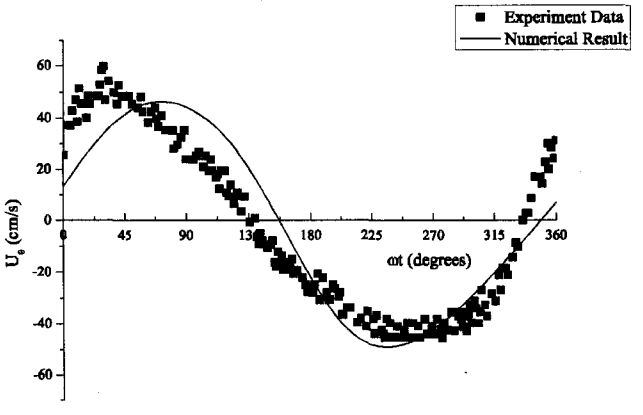

(c)

Figure 3.17: Period-Averaged Velocity Components at Point P for KC=1.1, D/L=0.15, z=0.4 from Bed: (a) Measurement Point (b) Radial Velocity (c) Tangential Velocity

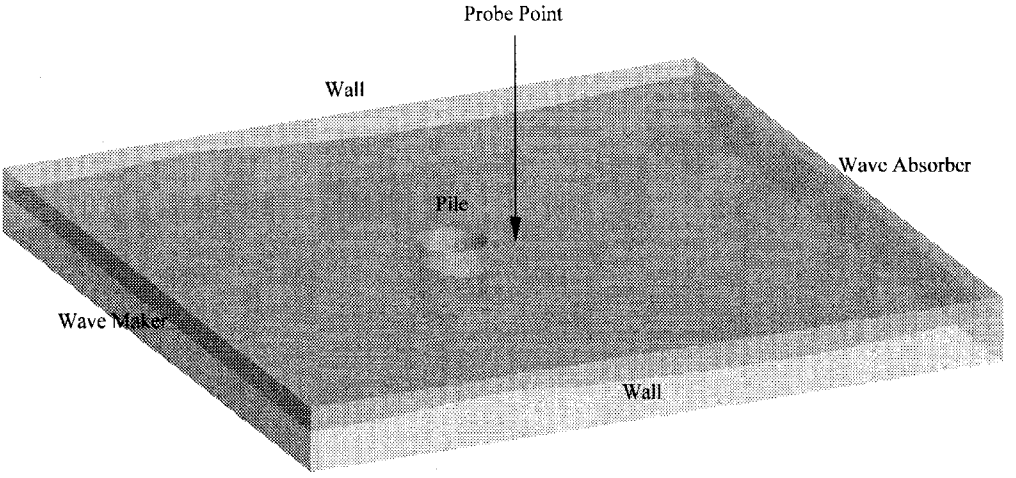

Figure 3.18: Free Surface of the Wave around Pile

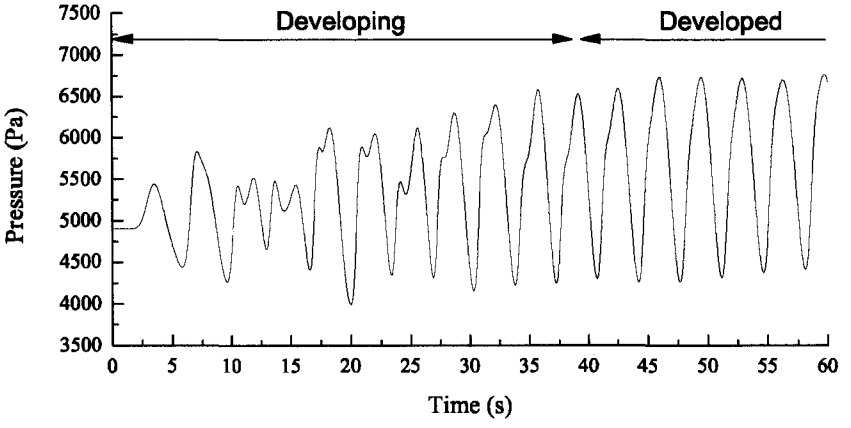

Figure 3.19: Pressure Probe at Point (x = 5.7 m, y = 0.2 m, z = 5.3 m)

Fig. 3.20 shows the equilibrium state of the scour around the pile. The numerical result is comparable with the experimental data although the maximum scour depth obtained with the numerical simulation is slightly higher than the experiment result. As in the experiment, the deposition zone is on the side of the pile and the scour zone is in the front and in the back. Although the scour pattern is not identical to that of the experimental results, they are very similar. Fig. 3.21 shows the scour around the periphery of the cylinder base. Only half of the periphery is shown because of symmetry. From this figure, the scour and deposition patterns around the pile are seen to agree well with the experiment except for the amplitude. This may be caused by the fact that some other factors in the experiment are not included in the numerical model. Further research is needed to make the model more accurate.

3.5 Discussion

3.5.1 Effect of Free Surface

For the rigid-lid approach, the free surface is replaced with an imaginary horizontal frictionless plane. In reality, even when the free surface is almost flat and will not change with time, a reasonable position for the free surface is not easy to be defined. This is because locally, such as in the case of free surface around a bridge pier, the free surface may change very abruptly and the rigid-lid approach simply can not capture these features. On the other hand, for the submerged wall jet case, the water depth in the flow domain is much bigger than the jet opening and the free surface changes very slowly. This makes the rigid-lid approximation a reasonable one. For scour around slender piles under waves, the rigid-lid assumption is also valid since the most important mechanism here is the vortex shedding and horseshoe vortex. However, for the wave-induced scour around large piles, it's unreasonable to use the rigid-lid approximation since the dominant mechanism here is the phase-resolved component of the wave flow and the steady streaming.

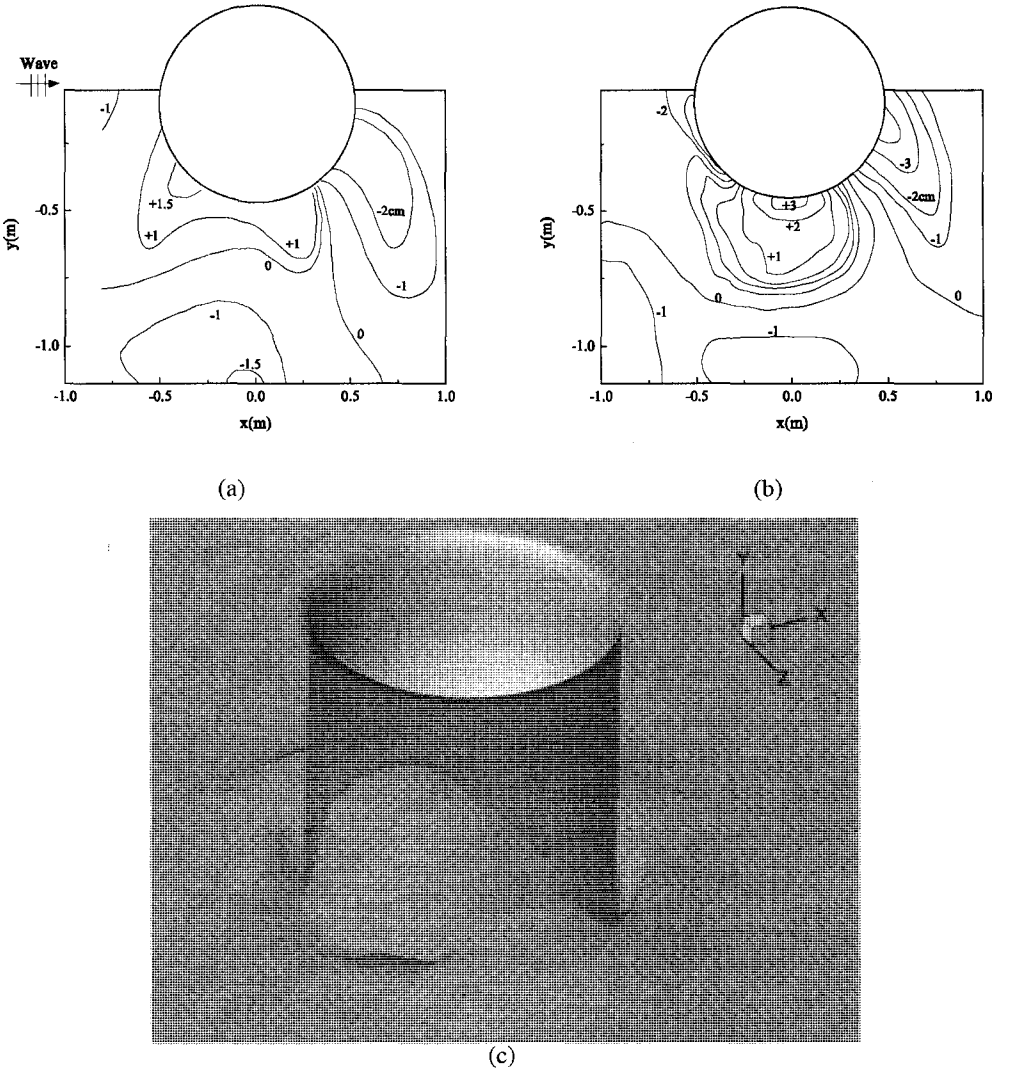

Figure 3.20: Wave Scour around a Large Vertical Circular Cylinder: (a) Experimental Data (b) Numerical Result (c) 3D View of Numerical Result

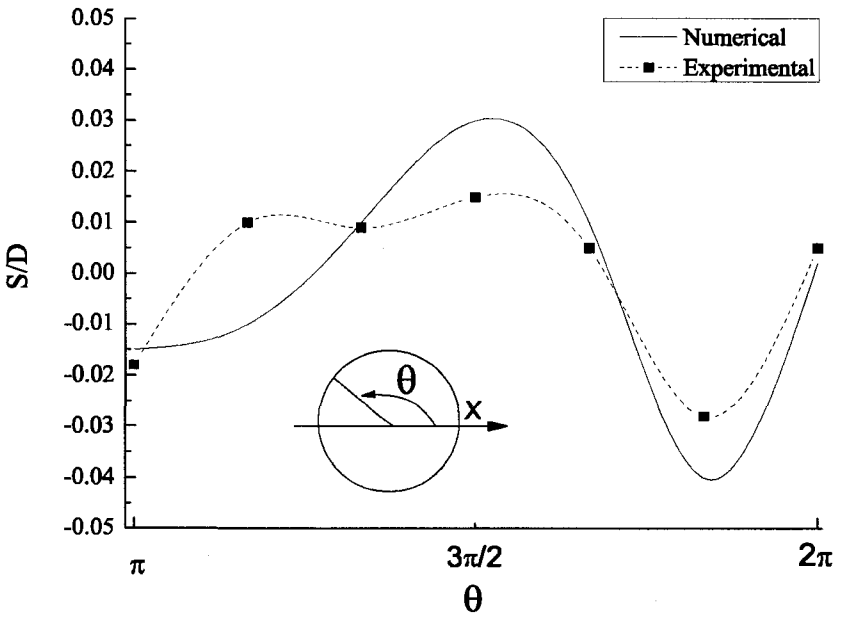

Figure 3.21: Scour at Periphery of Cylinder Base

3.5.2 Interface Capturing Techniques

In the current numerical model, the two moving surfaces (water free surface and moving bed) are captured by different approaches, namely Eulerian and Lagrangian approaches. The free surface is solved by CICSAM VOF scheme, which is an Eulerian approach. The moving bed is captured by mesh deformation method, which is a Lagrangian approach. The scour test cases in this work are relatively simple. For more complicated problems, if there are objects interacting with the fluid phase and the bed, the moving mesh technique will not be appropriate. The interface between the object, water and bed is so complicated and changing with time. Simply moving a grid point along the interface will be not feasible. For such cases, the Eulerian approach (VOF or LSM) can be used to implicitly track the interface. This could provide a new research direction in the scour problem and is currently being explored.

3.5.3 Limitation of Mesh Deformation Approach

As mentioned in the previous section, the mesh deformation approach is hard to implement with the presence of interaction between moving objects and bed or when the boundary movement is irregular. Also when the amplitude of the boundary movement is big enough, the mesh may be highly distorted and the deteriorated mesh quality will make the computation not easy to converge, eventually leading to unstable solutions. In order to avoid these problems, dynamic mesh approach should be used. In dynamic mesh approach, mesh cells can be split or merged when necessary. But comparing with mesh deformation, dynamic mesh approach is more difficult. Combination of these two approaches can be promising for scour problem where scour pattern is complicated and the scour/deposition depth is very large.

3.6 Conclusions

Numerical model FOAMSCOUR for local scour with free surface and automatic mesh deformation is proposed. The turbulence model used is the simple two equation $k - \epsilon$ model. Other turbulence models, even large eddy simulation, can be used to improve the accuracy of the fluid flow field simulation. All these models are readily implemented in OpenFOAM. The free surface is modeled by VOF method while the scour process is modeled by moving mesh method. These two methods for moving boundaries(free surface and bed) are coupled together. Each method has its merits and shortcomings. Eulerian approach can be used to capture the complex scour profiles. Flow field is coupled with sediment transport (both bed load and suspended load) using a quasi-steady approach. Parallel computations are used to reduce the CPU time which is usually tremendously large for morphological simulations (Parker and García 2006).

Numerical simulations for turbulent wall jet scour and wave scour around large vertical cylinder are carried out to compare with experiments. Good results have been obtained using the proposed modeling approach. Velocity field and other flow field characteristics compare fairly well with experimental observations. The maximum scour depths and local scour profile fit well with

the experiment data. Further research is needed to investigate the effect of turbulence model for free surface waves (especially for near breaking and breaking waves) and to study the possibility of using an Eulerian approach for morphological modeling.

Chapter 4

Three-Dimensional Numerical Model for Momentary Liquefaction Potential under Waves

4.1 Introduction

The interest in wave-seabed-structure interaction is growing because it is important for geotechnical engineers to design offshore foundation and structure (such as pipe lines, piles and break waters). Also sinking/floating of objects on the sea bed (such as wrecked ships, mines) is closely related to the sea bed response under waves. Many experiments (Sakai et al. 1994; Sumer et al. 1999) and numerical simulations (Magda 1996; Jeng and Lin 1999; Gao et al. 2003; Liu and García 2006b) have been done to try to understand this complicated process. There are also many analytical models which describe the sea bed response and give fairly good results (Yamamoto 1977; Mei and Foda 1981; Jeng and Hsu 1996; Yuhi and Ishida 2002).

Although many numerical models have been developed to solve sea bed response under wave, most of them just assume the wave pressure on the water-bed interface using wave theory. This is valid for many cases if there is only water wave and sea bed interaction. But for the case when there is extra object in the system (such as pile, semi-buried foundation, etc.), the water flow around the object will be highly three dimensional and is not easy to get an analytical solution from wave theory. Wave, sea bed and object form a big coupled system. Multi-physics numerical models have been widely used to solve these coupled systems. The approach in these models is to solve different governing equations on different domains (or some on the same domain) and couple the

*This chapter, as a manuscript, is published in International Journal of Offshore and Polar Engineering

system through common boundary or other ways. This is also the approach used in this chapter. 3D computational fluid dynamics (CFD) models is used to predict the free surface wave field and the results can be used as boundary condition for the sea bed governing equations.

Traditionally, the Biot consolidation equations used in this chapter to describe the sea bed response are solved via finite element method (FEM). FEM is the most widely used method in stress analysis. But FVM is gaining popularity in this area because it is good at treating complicated, coupled and non-linear differential equations (Jasak and Weller 2000). Application of FVM in stress analysis can be found, among many others, in Demirdžić et al. (1994) and Demirdžić et al. (1997). An iterative scheme for the Biot consolidation equation using FVM is proposed in this chapter. Momentary liquefaction potential due to waves are assessed based on the numerical result of consolidation.

The structure of this chapter is as follows. Governing equations of the coupled system are described first. Then the numerical schemes used in this chapter are discussed. Numerical verification and application of the current model are provided. Discussion and conclusion are at the end of the chapter.

4.2 Governing Equations

Fig. 4.1 shows a typical experiment setup for the sea bed response under waves. Governing equations in different parts of the domain (sea bed domain and fluid domain) are listed below. The sea bed response is governed by Biot consolidation equations. The fluid flow is governed by Navier-Stokes equations with $k - \epsilon$ turbulence model.

4.2.1 Biot Consolidation Equations

Governing equations for the poro-elastic sea bed two phase media is the Biot consolidation equation (Biot 1941):

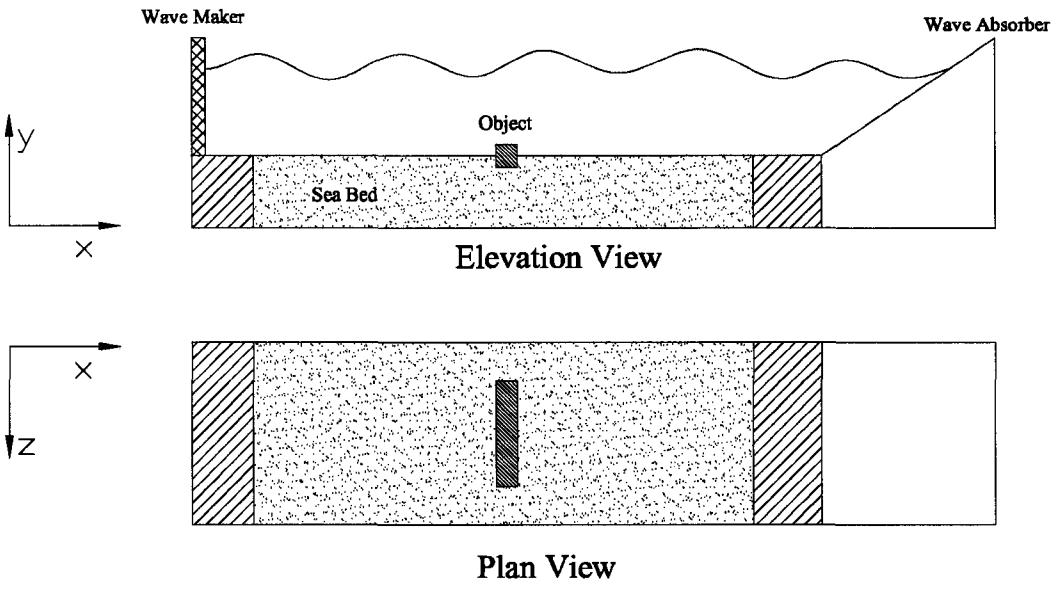

Figure 4.1: Schematic View of Typical Experiment Setup for the Sea Bed Response under Waves

$$G\nabla^2\mathbf{v} + \frac{G}{1-2\nu}\nabla(\nabla\cdot\mathbf{v}) = \nabla p \tag{4.1}$$

$$\frac{k}{\gamma}\nabla^2 p = \frac{n}{K'}\frac{\partial p}{\partial t} + \frac{\partial}{\partial t}(\nabla\cdot\mathbf{v}) \tag{4.2}$$

Eq. 4.1 is the force balance equation of the bed soil, and Eq. 4.2 is the storage equation which describes the mass balance of the pore water. Here p is the pore water pressure, $\mathbf{v}$ is the displacement of soil skeleton. G is the shear modulus of soil, ν is the Poisson ratio of the soil, K is the coefficient of the isotropic permeability of soil, γ is the specific weight of water, K' is the bulk modulus of elasticity of water, n is the soil porosity. These equations assume that the hydraulic permeability is isotropic and the stress-strain relationship is linear. Strain tensor ϵ is defined in

terms of the displacement vector **v** as

$$\epsilon = \frac{1}{2}\left[\nabla \mathbf{v} + (\nabla \mathbf{v})^T\right] \tag{4.3}$$

and the stress tensor σ is related to strain rate ϵ via

$$\begin{aligned} \sigma &= \sigma^{'} - p\mathbf{I} && (4.4) \\ &= 2G\epsilon + \left[2G\frac{\nu}{1-2\nu}tr\left(\epsilon\right) - p\right]\mathbf{I} && (4.5) \end{aligned}$$

where **I** is the unit tensor. $tr(\epsilon)$ is the trace of the tensor ϵ which is equal to $\nabla \cdot \mathbf{v}$. This equation also says that the stress in soil is constituted by two parts:the effective stress $\sigma^{'}$ supported by soil skeleton and pore water pressure p. Here the stress-strain relationship is slightly different from that of elastic solid. The only difference is that the pore pressure is included for the porous media. Plane strain is also assumed here.

4.2.2 Navier-Stokes Equations

The governing equations for the wave part is the Navier-Stokes equations:

$$\begin{aligned} \nabla \cdot \mathbf{u} &= 0 && (4.6) \\ \frac{\partial \rho \mathbf{u}}{\partial t} + \nabla \cdot (\rho \mathbf{u}\mathbf{u}) - \nabla \cdot (\mu \mathbf{S}) &= -\nabla p + \rho \mathbf{g} + \sigma K \frac{\nabla \alpha}{|\nabla \alpha|} && (4.7) \end{aligned}$$

where **u** is the velocity vector field, p is the pressure field, α is the volume fraction function for the two fluids defined by

$$\alpha = \begin{cases} 0 & \text{volume occupied by air} \\ 1 & \text{volume occupied by water} \end{cases} \tag{4.8}$$

S is the strain rate tensor defined by $\mathbf{S} = \frac{1}{2}\left[\nabla \mathbf{u} + (\nabla \mathbf{u})^T\right]$. σ is surface tension, K is the surface curvature. Surface tension is not so important in current problem but it's included for complete-

ness. The density ρ and viscosity μ in the domain is given by

$$\rho = \alpha\rho_1 + (1-\alpha)\rho_2 \tag{4.9}$$

$$\mu = \alpha\mu_1 + (1-\alpha)\mu_2 \tag{4.10}$$

Volume fraction α is transported by the fluid velocity field. The equation for the volume fraction scalar α is

$$\frac{\partial\alpha}{\partial t} + \nabla\cdot(\mathbf{u}\alpha) = 0 \tag{4.11}$$

Numerical diffusion will spread out the sharp interface between water and air. An compressive interface capturing scheme is used to resharpen the interface. The details of the present free surface modeling can be found in Ubbink and Issa (1999).

4.2.3 Turbulence k- ϵ Model

Equations in wave part are closed by conventional k- ϵ model (Lauder and Spalding 1973; Rodi 1993).

$$\mu_t = C_\mu\rho\frac{k^2}{\epsilon} \tag{4.12}$$

$$\frac{\partial k}{\partial t} + \nabla\cdot(\mathbf{u}k) = \frac{1}{\rho}\nabla(\frac{\mu_t}{\sigma_k}\nabla k) + 2\frac{\mu_t}{\rho}|\nabla\mathbf{u}|^2 - \epsilon \tag{4.13}$$

$$\frac{\partial\epsilon}{\partial t} + \nabla\cdot(\mathbf{u}\epsilon) = \frac{1}{\rho}\nabla(\frac{\mu_t}{\sigma_\epsilon}\nabla\epsilon) + 2\frac{C_1\mu_t}{\rho}|\nabla\mathbf{u}|^2\frac{\epsilon}{k} - C_2\frac{\epsilon^2}{k} \tag{4.14}$$

where μ_t is turbulence eddy viscosity, k is turbulence kinetic energy and ϵ is turbulence energy dissipation rate. The constants appear in Eqs. (4.12), (4.13) and (4.14) take the values given in Table 3.1.

4.3 Numerical Simulation Schemes and Procedures

The code used in this research is the open source numerical library (OpenCFD 2006). It's freely available through internet. OpenFOAM is primarily designed for problems in continuum mechanics. It uses the tensorial approach and object oriented techniques (Weller et al. 1998). OpenFOAM provides a fundamental platform to write new solvers for different problems as long as the problem can be written in tensorial partial differential equation forms. In this research, the flow field is solved by the adaption of the original turbulence solver for incompressible fluid in the code. The consolidation equation solver is newly added. The core of this code is the finite volume discretization of the governing equations. Almost all kinds of differential operators possible in a partial differential equation, such as temporal derivative, divergence, laplacian operator, curl, etc, can be discretized in the code. The finite volume details of the code can be found in Jasak (1996). One application of OpenFOAM in stress analysis can be found in Jasak and Weller (2000). Next several sections briefly introduces the numerical schemes used in the coupled solvers.

4.3.1 Numerical Scheme for Foundation Part

Finite element method is usually used to solve the Biot equations of soil consolidation (Lewis and Schrefler 1998) and to do other stress analysis. But finite volume method is becoming popular because of its flexibility to deal with complex domain. In this chapter, FVM is used to solve the consolidation equations. Comparing the Biot consolidation equations with the Navier-Stokes equations shows they are very similar. Both equations couple two quantities (pore pressure and displacement for consolidation, pressure and velocity for fluid) and both equations describes the mass balance and force balance. Inspired by these similarities, a new scheme is proposed to solve consolidation equations on an iterative basis. This iterative procedure is similar to the SIMPLE and PISO schemes for Navier-Stokes equations. A segregated approach is used to solve the couple consolidation equation which means components of the displacement vector and pore pressure are solved separately. At each time step, storage equation (Eq. 4.2) is rearranged into implicit and

explicit parts and is solved first according to

$$\underbrace{-\frac{n}{K'}\frac{\partial p}{\partial t}+\frac{k}{\gamma}\nabla^2 p}_{\text{implicit}}=\underbrace{\frac{\partial}{\partial t}(\nabla\cdot\mathbf{v})}_{\text{explicit}} \tag{4.15}$$

where the displacement $\mathbf{v}$ in the explicit part is from previous iteration or initial condition. Then the force balance equation (Eq. 4.1) is solved. In order to get higher efficiency of the segregated solver and to increase the convergence radius, a decomposition and a rearrangement of Eq. 4.1 is carried out similar to Jasak and Weller (2000). The terms in the equation are also split into implicit part and explicit part. The aim is to achieve maximum implicity. Assuming G and ν are constant, using the fact that

$$\nabla(\nabla\cdot\mathbf{v})=\nabla\cdot(\mathbf{I}\nabla\cdot\mathbf{v})=\nabla\cdot(\mathbf{I}\mathrm{tr}(\nabla\mathbf{v})) \tag{4.16}$$

the force balance equation (Eq. 4.1) can be written as

$$\underbrace{G\nabla^2\mathbf{v}+\frac{G}{1-2\nu}\nabla^2\mathbf{v}}_{\text{implicit}}=\underbrace{\nabla p-\nabla\cdot\left(\frac{G}{1-2\nu}\mathbf{I}\mathrm{tr}(\nabla\mathbf{v})-\frac{G}{1-2\nu}\nabla\mathbf{v}\right)}_{\text{explicit}} \tag{4.17}$$

Eq. 4.17 is solved for each component of vector $\mathbf{v}$ and the resulting $\mathbf{v}$ is used to solve storage equation again. This inner coupling is looped until desired convergence tolerance is achieved.

4.3.2 Numerical Scheme for Fluid Part

The numerical solution for Navier-Stokes equation of incompressible fluid flow imposes two main problems (Jasak 1996): the nonlinearity of momentum equation and the pressure-velocity coupling. For the first problem, two common methods can be used to deal with it. The first is to solve a nonlinear algebra systems after the discretization. This will need a lot of computational effort. The other is to linearize the convection term in the momentum equation by using the fluid velocity in old time steps which satisfies the divergence-free condition. The latter method is used in this research. For pressure-velocity coupling, many schemes exist, such as SIMPLE (Patankar 1981)

and PISO (Issa 1986). PISO scheme is used in this code. For the $k-\epsilon$ turbulence model equations, although k and ϵ equations are coupled together, they are solved by segregated approach, which means they are solved one at a time. This is also the usual approach used in most CFD codes.

4.3.3 Grids

There are two grids in the computational domain. One is for the fluid and the other is for the sea bed. Since no governing differential equation is specified on the object, no grid is needed for it. In some cases such as ocean pipe line analysis, the deformation of those pipes under wave is important and the grid for the pipe is needed (Magda 1996). Fig. 4.2 shows how the two grids (wave tank and sea bed)are used to do coupling computations. Information is transferred between fluid grid and sea bed grid via the common boundary, i.e. sea bottom. The figure also shows the presence of an object.

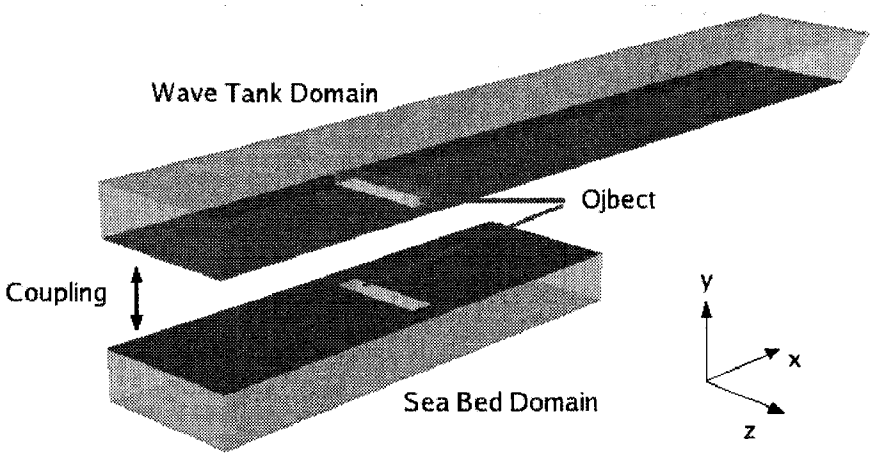

Figure 4.2: Coupling between Fluid Domain and Bed Domain

4.3.4 Boundary Conditions

Boundary Conditions for the Sea Bed Domain

In this chapter, only finite soil depth is considered for the sea bed domain because it's the case for most of the physical experiments. Infinite soil depth case can be achieved by extending the sea bed downward until the numerical result won't change anymore. The boundary conditions for the sea bed domain is very similar to Magda (1996) and Jeng and Lin (1999). At the bottom of the sea bed, zero displacements and zero vertical flow are specified, i.e.

$$\mathbf{v} = 0 \tag{4.18}$$

$$\frac{\partial p}{\partial \mathbf{n}} = 0 \tag{4.19}$$

where $\mathbf{n}$ is the surface normal direction vector.

At the top of sea bed (i.e. the common boundary between two domains), the fluid shear stress is neglected and the pore water pressure is equal to water wave pressure on the bed. This pressure value comes from the fluid solver. For the displacement on this surface, it's more complicated. Since the pore water pressure is set to be the wave pressure, the effective normal stress σ'_{yy} on the this boundary is zero. This gives the boundary condition of Neumann type (traction boundary) for displacement (Demirdžić et al. 1994; Jasak and Weller 2000)

$$\mathbf{n} \cdot \nabla \mathbf{v} = \frac{\mathbf{t} - \mathbf{n} \cdot \left[\mu \left(\nabla \mathbf{v}\right)^T - \left(\mu + \lambda\right) \nabla \mathbf{v}\right] - \lambda \mathbf{n} \nabla \cdot \mathbf{v}}{2\mu + \lambda} \tag{4.20}$$

where $\mathbf{t}$ is the traction stress on the bed which equals zero for the free bed surface in this case.

On the surfaces of object, it's assumed that no water can flow through. So zero pressure gradient as in Eq. 4.19 applies. For the displacement on the object, the object sides and bottom are considered separately. For the object sides, it's assumed that the sides are smooth and the soil can slip on the surface. The normal displacement component on the sides are set to zero. For the object

bottom, the traction boundary condition (Eq. 4.20) is specified. The traction on the bottom is from the simple force balance of the object (see Fig. 4.3). The forces on the object are flow drag F_{drag}, flow lift F_{lift}, gravity $m\mathbf{g}$ and bottom supporting force. The friction force on the object sides are neglected. This is reasonable because the sand on the sides of the object can be assumed loosely back filled in experiment. The flow drag and lift are calculated at each time step from the flow solver. So the Neumann type condition in Eq. 4.20 is applied with traction $\mathbf{t}$ from force balance of the object. This assumption is valid if the object is rigid body and will not move. It will be violated if the object is moving under wave force.

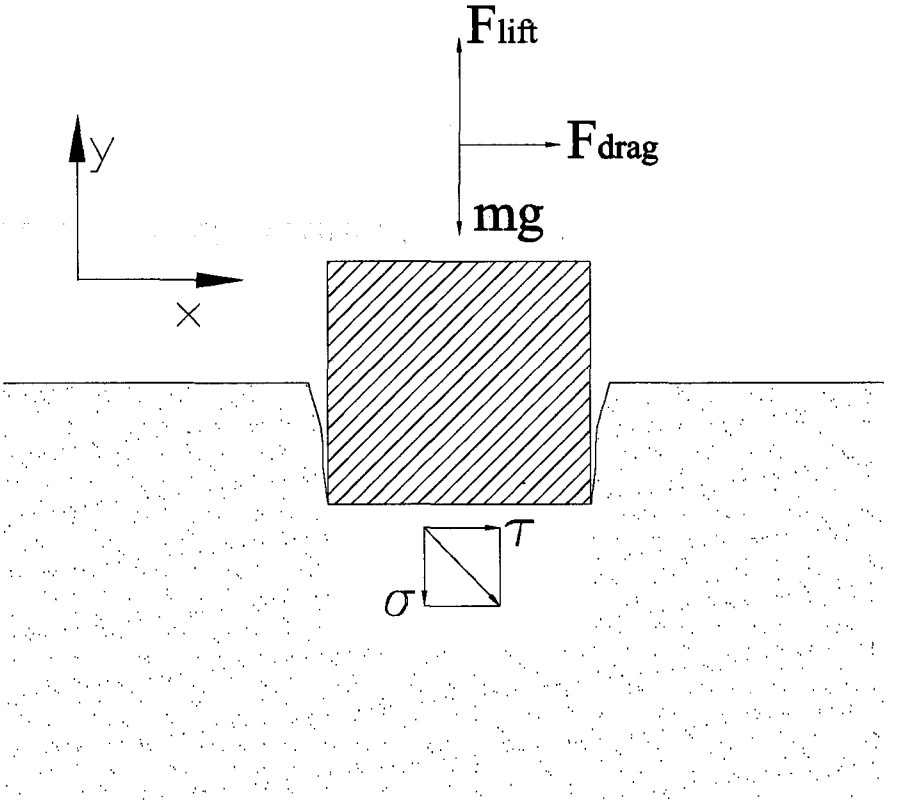

Figure 4.3: Force Balance of the Object

Boundary Conditions for Fluid Domain

The wave in the physical experiment is usually generated by a piston type wave maker and at the end of the wave tank, there is a wave absorber to eliminate the wave reflection. In numerical simulation, the wave can be generated generally by two approach: moving mesh (Aliabadi et al. 2003) and wave boundary condition (Mayer et al. 1998). For moving mesh approach, the piston movement is simulated by moving the boundary of the computational domain. For wave boundary condition approach, the mesh is fixed but boundary condition on the piston part is given by wave theory. The second approach is adopted in this chapter. A time varying velocity profile is imposed at the piston boundary to generate the waves

$$\vec{U} = f_r(t)\left[\vec{U}(y)sin(\omega t + \theta)\right] \tag{4.21}$$

where $\vec{U}$ is the velocity vector at the boundary, ω is the wave frequency, θ is the phase. $\vec{U}(y)$ is imposed by the type of the piston. $f_r(t)$ is the "ramp" function to start up the piston. $f_r(t)$ has the form

$$f_r(t) = \begin{cases} \frac{t}{T} - \frac{1}{\pi}sin\left(\pi\frac{t}{T}\right) & \text{for } 0 < t < T \\ 1 & \text{for } t > T \end{cases} \tag{4.22}$$

where T is the wave period.

The wave absorber is simulated using a damping zone (or sponge layer). In this damping zone, extra fluid viscosity is added to the momentum equation to dissipate the fluid dynamic energy. In numerical test cases, in order to eliminate the introduced artificial effect, the damping zone is extended far downstream. That's the reason that the wave tank domain used in this chapter will be longer than the sea bed domain. An alternative method by modifying the water depth and fluid velocity in the damping zone can be found in Mayer et al. (1998).

At the piston, pressure is set to be zero normal gradient to be consistent with velocity condition. Turbulence quantities such as k and ϵ are set as zero normal gradient at the piston wall. The

condition at the wave tank outlet is chosen as zero gradient for all quantities except pressure which is specified as hydrostatic (i.e., the dynamic pressure is zero). The top boundary of the fluid domain is atmosphere. The dynamic pressure is set to zero as the outlet and the velocity is set to zero. Other quantities are set to zero normal gradient. At the object's surfaces or flume walls, it is assumed to be hydraulically smooth. No-slip condition is set for velocity with zero normal gradient for pressure. Other quantities such as k and ϵ are also set as zero normal gradient.

4.3.5 Simulation Process

In order to study the effect of waves, base state of pore pressure and displacement without wave is obtained by doing the computation for a period of time with the wave maker shut off. This resembles the fact that in the experiment, the bed soil is already in the equilibrium state before the wave maker is started. After that, the wave maker boundary condition is switched on and waves are generated. Base stable pore pressure and displacement is subtracted from the result to investigate the effect of waves. The main application of current numerical model is the study of liquefaction potential. When the pore water pressure is so excessive that the effective stress in soil is zero or negative, the soil is in the state of liquefaction (Jeng 1996). For a flat bed, the criterion for liquefaction is

$$\frac{p}{\frac{1}{3}\left(\gamma_s - \gamma_w\right)\left(1 + 2K_0\right)y} \geq 1 \tag{4.23}$$

where p is excessive pore pressure, γ_s and γ_w are unit weight of soil and water, K_0 is the coefficient of lateral earth pressure at rest which ranges from 0.4 to 1.0. y is the depth of the soil measured downward from the bed. But for complicated computational domain, it is not easy to calculate the effective soil gravity force at each point in the bed. In this chapter, the dimensionless excessive pore water pressure (non-dimensionized by $p_0 = \rho g H_0$, where H_0 is the wave height) is used as an indicator for the liquefaction potential.

At each time step, the fluid field is first solved and the pressure on the sea bed is mapped to the bed domain. Based on the pressure from fluid solver, the Biot consolidation equations are solved.

This process continues until wave period averaged pore pressure and displacement reach steady state or the specified computation time is reached.

4.4 Model Verification and Applications

4.4.1 Verification of FVM Solver for Biot Consolidation Equations

In order to verify the Biot equation solver in the numerical model, a test case which is similar to that of Jeng and Lin (1999) is carried out. Fig. 4.4 is the schematic view of the test case. The details of the test case can be found in Jeng and Lin (1999) and the analytical solution can be found in Jeng and Hsu (1996). In this test case, uniform sea bed is under the progressive wave. The bed soil depth $h = 1m$ and the wave pressure amplitude $p_b = 2000N/m^2$. The wave number $k = \pi$ and wave frequency $\omega = 2\pi$.

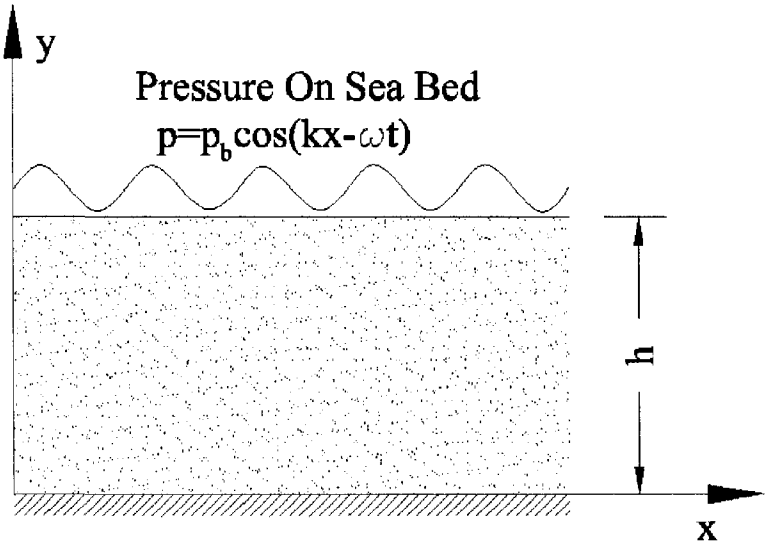

Figure 4.4: Numerical Test of Sea Bed Response

The numerical result of excessive pore pressure at each depth of the soil versus $kx - \omega t$ is plotted in Fig. 4.5. The analytical solution is also plotted. The difference between numerical result

and analytical solution is so small that they are almost identical to each other. From the figure, the excessive pore pressure diffuses with the increase of depth which is as expect. For flat bed, top layers of soil are most vulnerable to storm waves and failure of foundation due to liquefaction always happens in these layers.

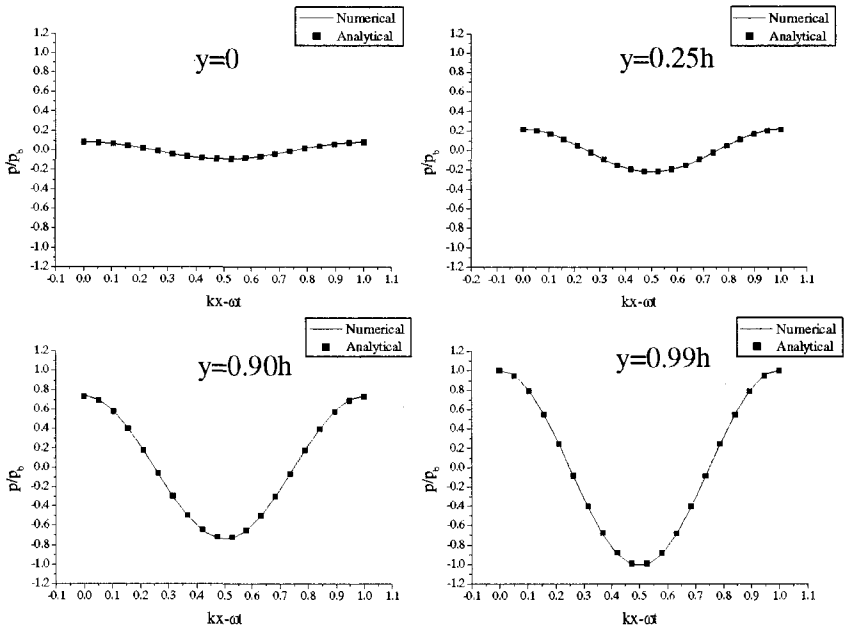

Figure 4.5: Pore Pressure Comparison between Numerical and Analytical Solution

Fig. 4.6 shows the numerical results of the test case. Fig. 4.6(a) shows the pore water pressure and Fig. 4.6(b) shows the displacement magnitude. From the figures, it's clear that under wave crest the pressure on the bed is increased and the soil is compressed. Under wave trough, it's just the opposite. The displacement vector field in Fig. 4.7 demonstrates this pattern even more clearly. The geometry in this figure is distorted by $1E+4$ times the displacement to show elastic deformation.

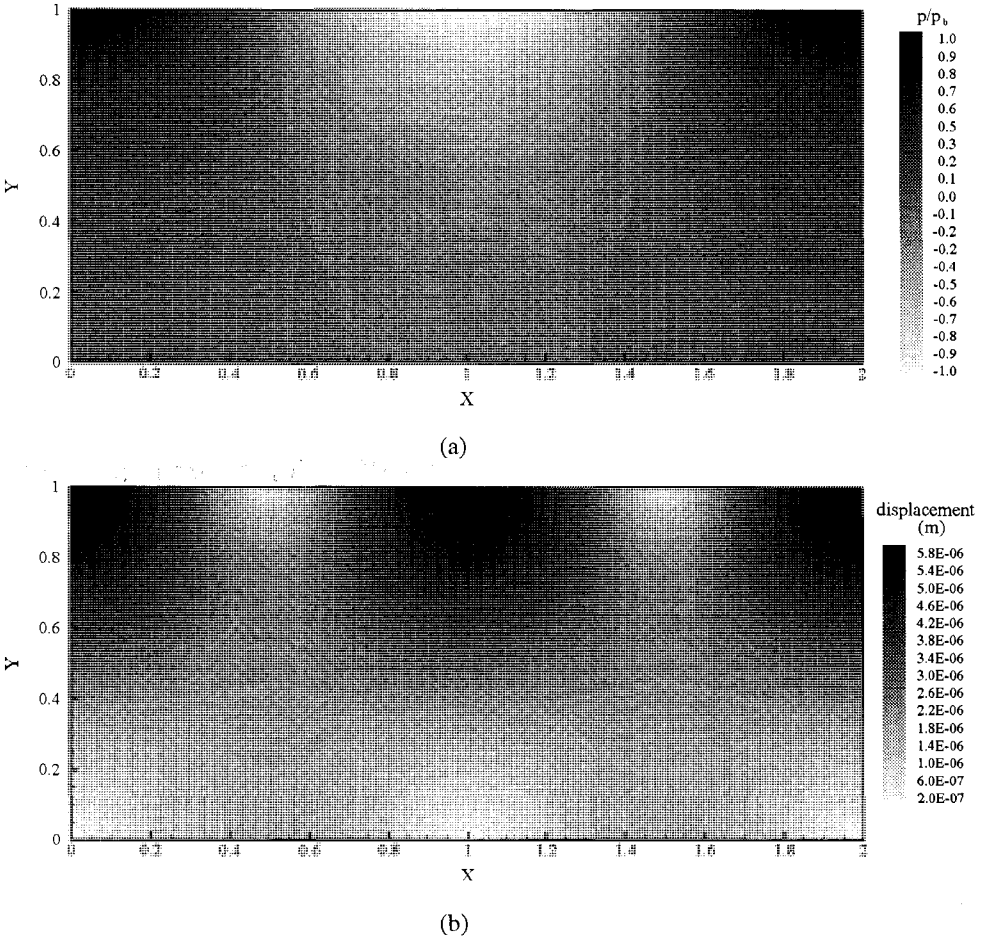

Figure 4.6: Displacement of Consolidation Test Case: (a) Pore Pressure (b) Magnitude of Displacement

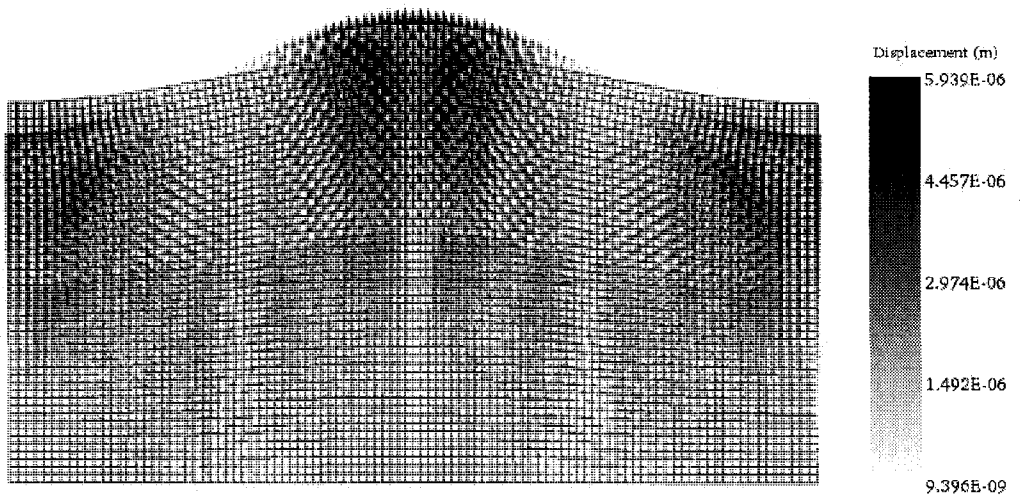

Figure 4.7: Displacement Vector Field (Geometry Distorted)

4.4.2 3D Test Case of Sea Bed Response under Waves with Presence of an Object

In this test case, 3D sea bed response in the numerical wave tank is simulated. The wave tank is $40m$ long and $3m$ wide. The water depth in the tank is $1m$. An object (which is represented by a box of dimensions $2m \times 0.5m \times 0.5m$) is half buried in the sand (see Fig. 4.1). The presence of the object will change the wave flow field. Hence the local pressure and force on the sea bed will be changed. $\vec{U}(y)$ in Eq. 4.21 is set as $0.5m/s$ and wave period T is $3s$. The generated wave height H_0 is about $0.4m$ and wave length is about $10m$. One fact needed to be pointed out is that the wave simulated in this chapter is not so strong that the excessive pore water pressure can't cause dramatic change in liquefaction zone. But the main purpose of this chapter is to demonstrate the new methodology of coupled solver of free surface fluid field and Biot consolidation equations. In order to simulate real storm waves, more computation resource is needed. Future research can use parallel computation to decrease the computational time and simulate bigger domain with higher wave height.

Fig. 4.8 shows the fluid force components and magnitude on the object. The forces on the object undergo periodical changes. The most significant components are in the streamwise direction and vertical direction which is as expected. The spanwise fluid force is very small comparing with the other two. Second mode effect can also be seen in the figure but is not significant. This could be caused by the wave reflection from the object or the wave tank end. The forces are used to calculate the traction boundary condition on the object bottom.

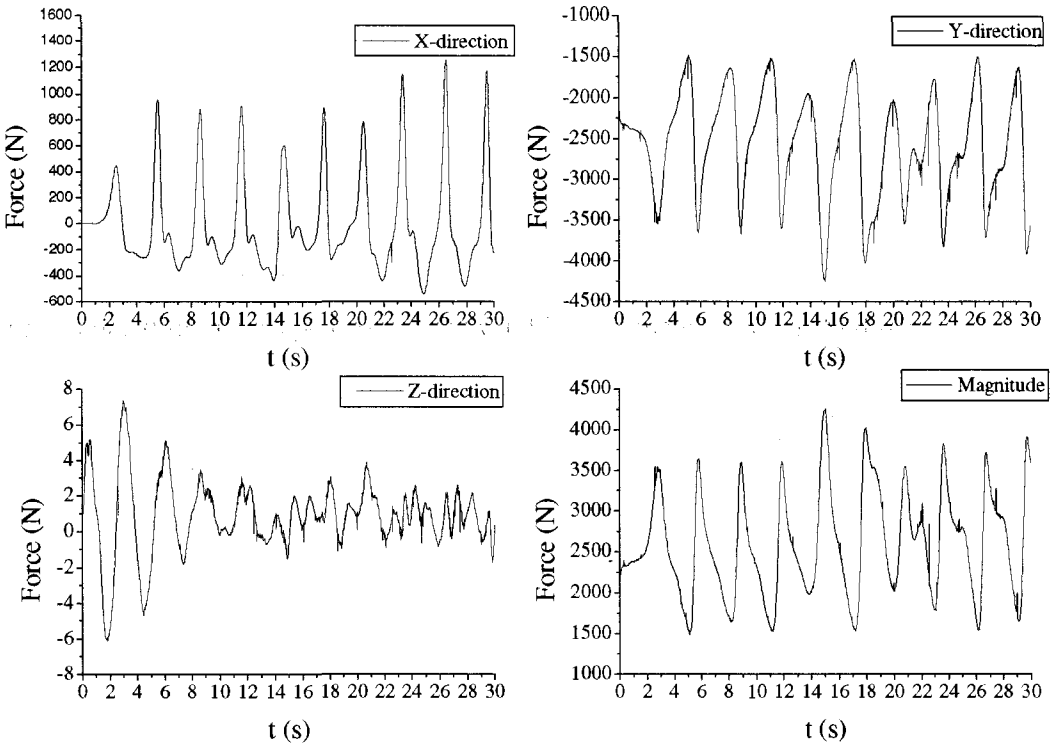

Figure 4.8: Object Force History

In Fig. 4.9, the free surface of waves in one typical period is plotted. The wave height relative to the water depth can also be seen. Fig. 4.10 shows the iso-surface of the dimensionless instantaneous excessive pore pressure inside the sea bed. With the propagation of the wave, the sea bed pressure response also moves forward accordingly.

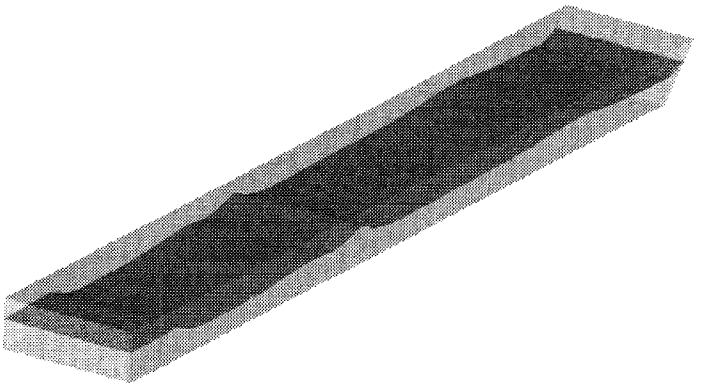

(a)

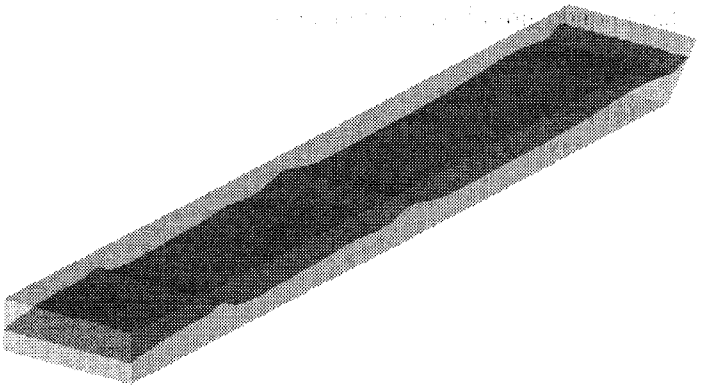

(b)

Figure 4.9: Free Surface of Waves in One Typical Period: (a) $t = t_0 + \frac{T}{4}$ (b) $t = t_0 + \frac{T}{2}$ (c) $t = t_0 + \frac{3T}{4}$ (d) $t = t_0 + T$

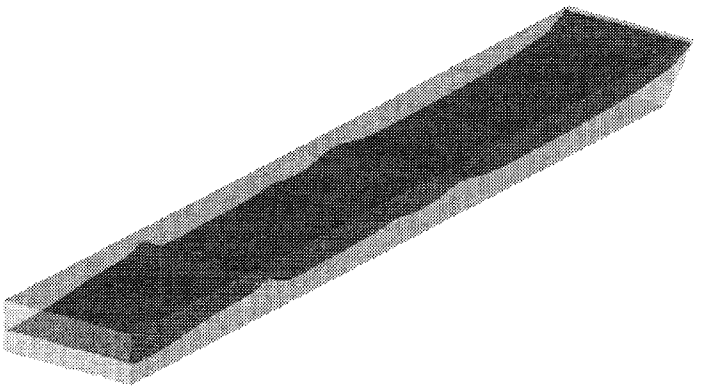

(c)

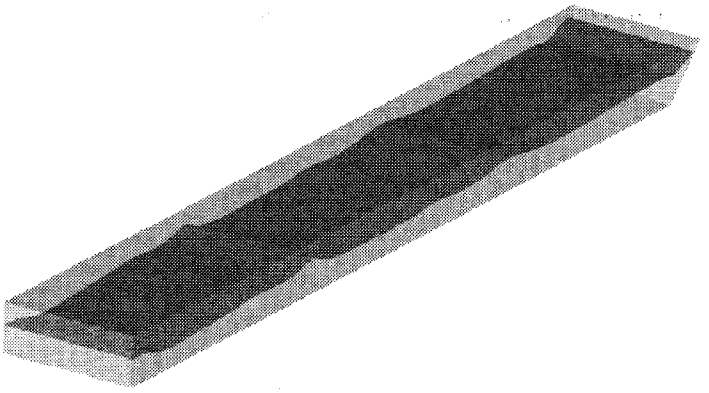

(d)

Figure 4.9: Free Surface of Waves in One Typical Period (Cont'd): (a) $t = t_0 + \frac{T}{4}$ (b) $t = t_0 + \frac{T}{2}$ (c) $t = t_0 + \frac{3T}{4}$ (d) $t = t_0 + T$

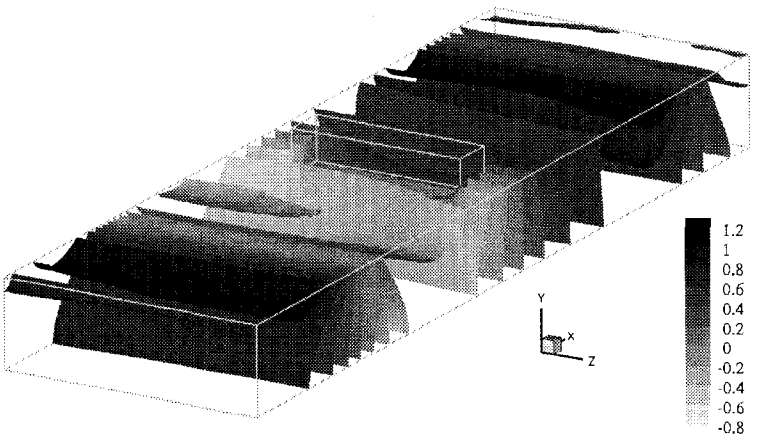

(a)

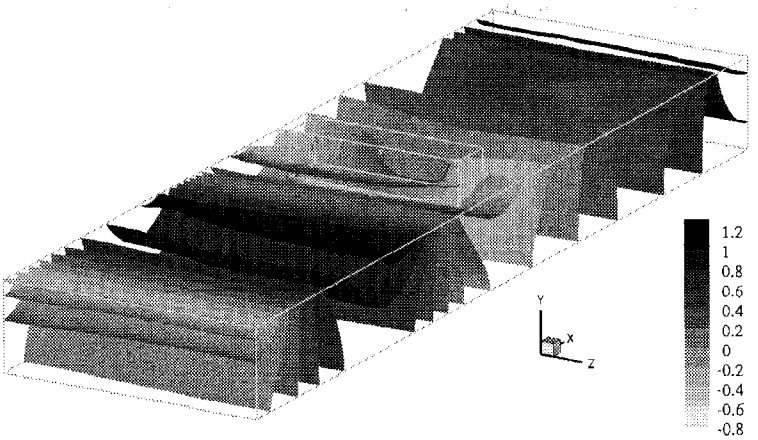

(b)

Figure 4.10: Dimensionless Excessive Pore Pressure under Waves in One Typical Period : (a) $t = t_0 + \frac{T}{4}$ (b) $t = t_0 + \frac{T}{2}$ (c) $t = t_0 + \frac{3T}{4}$ (d) $t = t_0 + T$

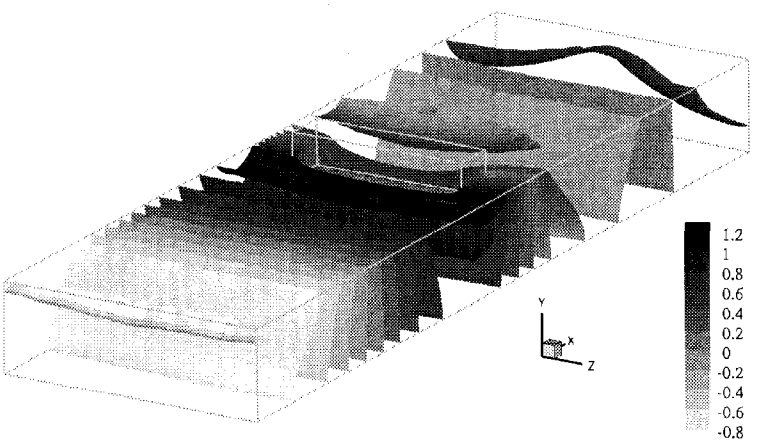

(c)

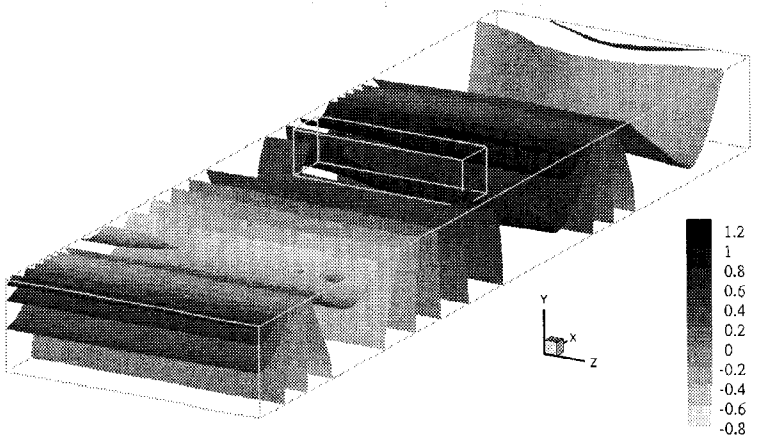

(d)

Figure 4.10: Dimensionless Excessive Pore Pressure under Waves in One Typical Period (Cont'd): (a) $t = t_0 + \frac{T}{4}$ (b) $t = t_0 + \frac{T}{2}$ (c) $t = t_0 + \frac{3T}{4}$ (d) $t = t_0 + T$

Fig. 4.11 is the contour plot of non-dimensionized excessive pore pressure under the instantaneous flow field ($t = t_0 + \frac{3T}{4}$) in Fig. 4.9(c). The reason to plot for this time point is that the wave crest is almost on top of the object and it's considered to be the most possible time for the momentary liquefaction to happen. From the figures, it's clear the pressure distribution is disturbed by the half buried object. At this very moment, the excessive pore pressure in front of the object is very high and the liquefaction potential in this area and under the object is amplified. From the slice view, the excessive pore pressure beneath the object is also at the peak value. This is caused by two facts. One is that the wave crest in just above the object. The other is that the fluid forces on the object are also at maximum values.

4.5 Discussion

4.5.1 Soil Constitutive Model Effects

For geotechnical problems, a realistic stress-strain constitutive relationship is one of the most important things for the ability of the numerical model to reproduce the reality situations. Herein, the simple linear isotropic elastic model is used to describe the soil skeleton. More advanced and accurate constitutive models (such as variable elasticity, elasto-plastic model and visco-plastic model, etc.) can be easily incorporated in the current numerical code. Anisotropic effect can also easily come into the model since the code is based on the tensorial description of the equations and anisotropic tensors can be included inside the differential operators.

4.5.2 Residual Liquefaction Effects

Only momentary liquefaction is model in this chapter since it is simple and easy. Liquefaction is an complicated physical process which is still not well understood today. Liquefaction is generally caused by two main mechanisms: momentary liquefaction and residual liquefaction (Sumer and Fredsøe 2002). Residual liquefaction is more complicated than momentary liquefaction because

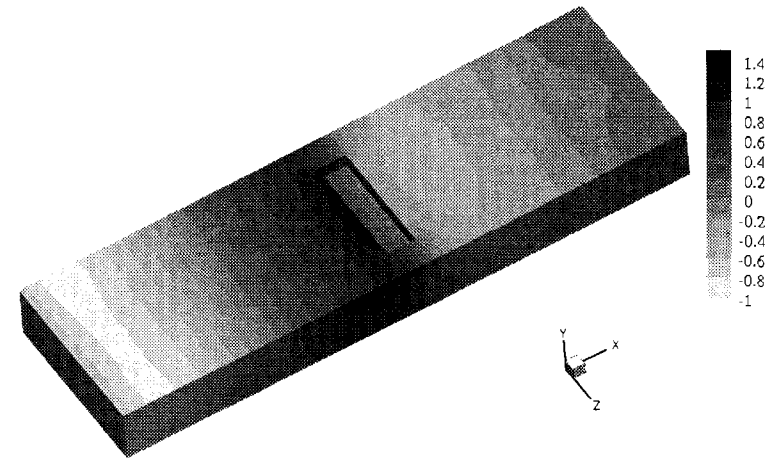

(a)

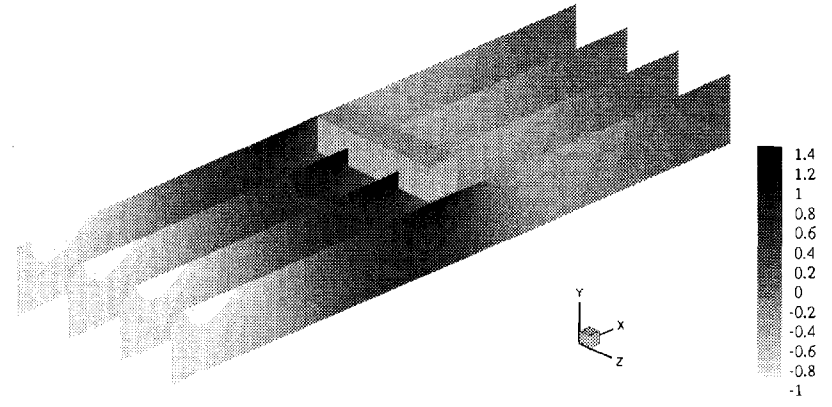

(b)

Figure 4.11: Dimensionless Excessive Pore Pressure on the Bottom Corresponding to the Moment of Fig. 4.9(c): (a) 3D view of the Bottom Pressure (b) Slice View of the Bottom Pressure

the pore pressure builds up with time. Some simplified models existing for the residual liquefaction add a source term to the governing equation of pore pressure. This can also easily be incorporated into current model. Further research is needed to carefully verify the parameters and to what happens after the liquefaction.

4.5.3 Bed Morphodynamics and Object Movement

In the wave-seabed-object system, another process, sediment transport, is also very important and is closely related the flow field and bed soil. Flow field change around the object causes scour and deposition of the sediment. Sediment movement will change the sea bed elevation and consequently affect the flow field. This sea bed change also will change the domain of the consolidation and change the pore pressure distribution. Scour is one of the main reasons of foundation failure in ocean and river engineering. Sediment transport together with the other processes modeled in this chapter forms an even bigger coupled system. Sediment transport and morphodynamic models should be included in the future.

The object is assumed to be at fixed position during the computation. This is not always true since when the liquefaction occurs, the soil can't support the object any more and the object will move. Even without liquefaction, the object could rotate or slide under the influence of fluid force. All these make the problem extremely complicated and it's impossible to include all factors into the numerical model. But by fixing the object in one position, it is possible to investigate the possibility of liquefaction and analyze the dynamics of the system. This could be useful for engineers to design structure and foundations to prevent damage under extreme conditions.

4.6 Conclusion

The numerical model in this chapter can solve the coupling problem between waves, object (structure) and sea bed response. Sea bed response under wave is one of the keys to the understanding of liquefaction. The wave induced shear stress and pore pressure in the soil is governed by Biot con-

solidation equation. Free surface is modeled by Volume of Fluid (VOF) method and water wave is generated by numerical wave maker boundary condition. Instead of using finite element method to do stress analysis inside the bed material which is the traditional method used in geotechniques, an iterative numerical scheme is proposed to solve Biot consolidation equation using finite volume method. The new scheme shows fast convergence rate and high accuracy. The coupling between water wave and sea bed is through pressure and stress condition on common boundaries. Two numerical tests of the proposed scheme is carried out. First numerical case tests the consolidation solver part of the numerical model. Good agreement with analytical results is obtained. The second case is a 3D test to study the interaction between wave, sea bed and object. A box is half buried in the wave tank. More complicated real geometry can be simulated as well. From the result excessive pore pressure of the sea bed, liquefaction potential can be analyzed. Only momentary liquefaction can be studied using current model. For residual liquefaction, the modified Biot consolidation equation should be solved. The model proposed in this chapter can be used to guide the design of under water structures and foundations.

Chapter 5

Models for the Residual Pore Water Buildup Process

5.1 Introduction

Liquefaction can cause enormous damage to infrastructures, and there has been great interest in the geotechnical profession to study the liquefaction due to earthquakes and general cyclic loadings. The most cited example of liquefaction damage due to the earthquake is the Alaska and Niigata earthquake in 1964 where buildings tilted. During an earthquake, shear waves are propagated upwards in the sediment deposit from the earthquake center to the surface. During an ocean storm, the water waves will induce cyclic shear stress on the bottom of the seabed. This cyclic shear stress will also lead to the buildup of excessive pore pressure in the same way as during an earthquake. Another aspect for an ocean storm is when structures interact with the water waves and the seabed, lateral forces and overturning momentum will be exerted on the structure. The forces and the momentum will change direction during one wave period. These facts will cause the foundation soil to experience cyclic stresses in both horizontal and vertical directions (Taiebat 1999).

In general, liquefaction is a term used to describe the behavior of loose saturated cohesionless soils, i.e. loose sands, which go from a solid state to a heavy liquid, or reach a liquefied state as a consequence of increasing pore water pressures, and thus decreasing effective stress. In Seed (1976), liquefaction is defined as a condition where soil deforms continuously with low residual strength or without strength. Liquefaction is more likely to occur in loose to moderate granular

*This chapter, as a manuscript, is in preparation for possible publication in Journal of Engineering Mechanics, ASCE

soils with poor drainage. Deposits most susceptible to liquefaction are young sands and silts of similar grain size (well-sorted), in beds at least several feet thick, and saturated with water. Such deposits are often found along river beds, beaches, and dunes. Some examples of liquefaction include quicksand, quick clay, fluid mud, and earthquake liquefaction (Wikipedia 2007). Although liquefaction can happen under both static and cyclic loadings, this chapter limits the study to the case of liquefaction due the cyclic loadings.

The interest in liquefaction is growing because it is important for geotechnical engineers to design onshore/offshore foundations and structures. Liquefaction is one of the main mechanisms which dominates the interaction between water waves, sea bed, and structures. Due to liquefaction, the supporting foundations will loose their strength and the supported structures (such as oil pipe lines) will sink or float and hence cause damage. Experimental work (Sakai et al. 1994; Sumer et al. 1999) and numerical simulations (Magda 1996; Jeng and Lin 1999; Gao et al. 2003; Liu and García 2006b; Cardenas and Wilson 2007) have been done to understand this complicated process. Analytical models which describe the sea bed response under waves have been developed for many years. Yamamoto (1977) treated the wave-induced sea bed response analytically based on the three-dimensional Biot consolidation theory (Biot 1941). Closed form of the analytical solutions are given. One conclusion from the paper is that the bed response is strongly dependent on the permeability and the stiffness ratio G/K', where G is the shear modulus and K' is the apparent bulk modulus of elasticity of water.

Mei and Foda (1981) treated the porous elastic medium using Biot's linearized theory, which can be seen as a special case of the mixture theory. For sufficiently high frequency waves, the area near the water-soil interface can be divided into a boundary layer of Stokes' type and an outside layer. In the outside layer, fluid and the solid skeleton move together according to the laws of the classical elasticity theory for a single phase. Based on this division, the governing equations can be simplified and analytical solutions are proposed.

In Jeng and Hsu (1996), a closed-form analytical solution is developed for the wave-induced pore pressure, soil displacements, and effective stresses in an elastic sea-bed subject to a system of

two intersecting waves. Although the solution is for the finite depth soil, it can be reduced to the conditions for soil of infinite thickness. The solution can also be extended to the limiting cases of two-dimensional progressive and standing waves for soil of finite thickness. The authors compared their analytical solutions with numerical results and the solutions from Yamamoto (1977) and Mei and Foda (1981). The proposed solutions are found in complete agreement with the results of Yamamoto (1977) for both fine sand and coarse sand. The solutions also agree with those of Mei and Foda (1981) for the fine sand while deviation is observed for coarse sand. In Jeng et al. (2007), a new approximation for the pore water pressure buildup in marine sediments is proposed which will be discussed in detail in this chapter.

Cheng et al. (2001) corrected some errors contained in the analytical solution for wave-induced pore pressure accumulation in McDougal et al. (1989) and gave the revised solution in a more general form. The authors studied the behavior of the solution under different soil conditions. For deep soil, the solution is sensitive to the soil shear stress in the top thin layer of the soil. In contrast, for shallow and finite depth soil, the solution is sensitive to shear stress in the thin layer of soil near the impermeable base. It is also found that a small error in the soil shear stress can lead to a large error in the accumulated pore pressure. Sensitivity analysis is also done to investigate the relationships between the accuracy of the pore pressure accumulation and the accuracy of the soil shear stress. In that paper, the simplified Biot consolidation equations are also solved numerically. Both analytical and numerical examples are given to validate the error estimation method proposed in that paper.

Most analytical models assume the soil to be an isotropic medium while natural soils always display some degree of anisotropy. The effects of soil anisotropy will have great effect on the sea bed response. They are revealed as the anisotropy of the soil Young's modulus, Poisson's ratio, and permeability. Analytical solutions which consider the soil anisotropy are complicated (Gatmiri 1992; Jeng 1997). Yuhi and Ishida (2002) gave simplified analytical solutions for the wave-induced response of a cross-anisotropic seabed of infinite thickness for both slightly and fully saturated conditions.

The literature mentioned above for liquefaction is almost all based on the linear theory of Biot consolidation. There are other theories proposed to explain the phenomenon of liquefaction. Foda et al. (1993) considered the rheological properties of marine sediment and incorporated them into potential flow equations for both water layer and the fluidized mud layer. The fluidization depth of the sediment is solved as a function of the imposed wave height.

Aside from analytical models, numerical models, especially from computational geomechanics, have also been developed to predict the liquefaction in the soil (Zienkiewicz et al. 1999). The poro-elastic model is the simplest constitutive relationship, and it is used in most analytical models. The elasto-plastic model is more popular in computational geomechanics, and it gives results which are closer to the experiment. Although it is easier to implement different constitutive relationships, the non-linearity associated with these relationships increases the computational cost tremendously.

Taiebat (1999) developed a three-dimensional elasto-plastic finite element model for the liquefaction problem of offshore foundations. By representing the variables of an axis-symmetric body as a discrete Fourier series, the three-dimensional problem is reduced to several small problems and therefore the computational cost is also reduced. This author proposed a new procedure for the liquefaction analysis of offshore foundations subjected to storm loadings. The numerical model is used to evaluate the liquefaction problem of Ekofisk tank which is constructed in North Sea.

Dunn et al. (2006) used the finite element model, DIANA-SWANDYNE II (Chan 1995) to study the wave-induced liquefaction around offshore structures. It is a two-dimensional model with the plane strain assumption. It solves the fully coupled Biot dynamic equation for both drained and undrained conditions. Different constitutive relationships are implemented in the model. Among many other interesting results, the authors found that the excessive pore pressure builds up more quickly around the structure and the boundary conditions at the structure have a great effect on the results.

Although many numerical models have been developed to solve sea bed response under waves, most of them just use the wave pressure on the water-bed interface by wave theory. This is valid

when there is only water wave and sea bed interaction. But when there is extra object in the system (such as pile, semi-buried foundation, etc.), the water flow around the object will be highly three-dimensional and it is not easy to get an analytical solution from wave theory. Wave, sea bed, and object form a large coupled system. Multi-physics numerical models have been widely used to solve these coupled systems. The approach in these models is to solve different governing equations on different domains and to couple the system through common boundaries or other ways. Three-dimensional CFD models can be used to predict the free surface wave field and the results can be used as boundary condition for the sea bed governing equations (Liu and García 2006b; 2007a).

The structure of this chapter is as follows. The governing equations for the consolidation of poro-elastic soil will be introduced. Source term, which is responsible for the excessive pore pressure generation, is added to the governing equations. Under some simplifications, the new equations system for the period-averaged pore pressure has analytical solutions. The analytical solutions of the sea bed pore pressure due to the progressive waves found in the literature are summarized. For deep sea bed, the behavior of the pore pressure is estimated using an asymptotic method. Numerical simulations which include the source term effect are carried out, and the results are compared with experiment and analytical solutions. At the end, a tentative effort is made to simulate the phase-resolved residual pore water pressure buildup process using the numerical model introduced in Chapter 4 with an extra source term from the current chapter.

5.2 Governing Equations

5.2.1 Three-Dimensional Biot Consolidation Equations

Governing equations for the poro-elastic seabed two-phase media is the Biot consolidation equation (Biot 1941):

$$G\nabla^2\mathbf{v} + \frac{G}{1-2\nu}\nabla\left(\nabla\cdot\mathbf{v}\right) = \nabla p \tag{5.1}$$

$$\frac{k}{\gamma}\nabla^2 p = \frac{n}{K'}\frac{\partial p}{\partial t} + \frac{\partial}{\partial t}\left(\nabla\cdot\mathbf{v}\right) \tag{5.2}$$

Eq. 5.1 is the force balance equation of the bed soil, and Eq. 5.2 is the storage equation which describes the mass balance of the pore water. Here p is the pore water pressure, $\mathbf{v}$ is the displacement of soil skeleton. G is the shear modulus of soil, ν is the Poisson ratio of the soil, K is the coefficient of the isotropic permeability of soil, γ is the specific weight of water, β is the compressibility of pore water, and n is the soil porosity. These equations assume that the hydraulic permeability is isotropic and the stress-strain relationship is linear. Strain tensor ϵ is defined in terms of the displacement vector $\mathbf{v}$ as

$$\epsilon = \frac{1}{2}\left[\nabla\mathbf{v} + \left(\nabla\mathbf{v}\right)^T\right] \tag{5.3}$$

and the stress tensor σ is related to strain rate ϵ via

$$\sigma = \sigma' - p\mathbf{I} \tag{5.4}$$

$$= 2G\epsilon + \left[2G\frac{\nu}{1-2\nu}tr\left(\epsilon\right) - p\right]\mathbf{I} \tag{5.5}$$

where $\mathbf{I}$ is the unit tensor. $tr(\epsilon)$ is the trace of the tensor ϵ which is equal to $\nabla\cdot\mathbf{v}$. This equation also states that the stress in soil is constituted by two parts: the effective stress σ' supported by soil skeleton and the pore water pressure p. Here the stress-strain relationship is slightly different from that of an elastic solid. The only difference is that the pore pressure is included for the porous media. Plane strain is also assumed here.

5.2.2 One-Dimensional Period-Average Pore Pressure Equations

McDougal et al. (1989) derived the simplified equation governing the buildup of pore water pressure. Assuming that the process is only one-dimensional in the vertical z direction, i.e., the variations with respect to other directions are negligible, then Eq. 5.1 can be written as

$$G\frac{2-2\nu}{1-2\nu}\frac{\partial^2 w}{\partial z^2} = \frac{\partial p}{\partial z} \tag{5.6}$$

and Eq. 5.2 becomes

$$\frac{k}{\gamma}\frac{\partial^2 p}{\partial z^2} = \frac{n}{K'}\frac{\partial p}{\partial t} + \frac{\partial^2 w}{\partial z \partial t} \tag{5.7}$$

Taking the derivative of Eq. 5.6 with respect to t and Eq. 5.7 with respect to z, and then cross eliminating the terms with w, the equations become

$$c_v\frac{\partial^3 p}{\partial z^3} = \frac{\partial^2 p}{\partial z \partial t} \tag{5.8}$$

where c_v is the coefficient of consolidation which has the form of

$$c_v = \frac{Gk}{\gamma}\frac{2-2\nu}{(1-2\nu)+(2-2\nu)\frac{nG}{K'}} \tag{5.9}$$

Integrating Eq. 5.8 with respect to z gives

$$\frac{\partial p}{\partial t} = c_v\frac{\partial^2 p}{\partial z^2} + c \tag{5.10}$$

where c is a constant. Moving-averaging Eq. 5.10 gives the governing equation for the period-averaged pore pressure

$$\frac{\partial \overline{p}}{\partial t} = c_v\frac{\partial^2 \overline{p}}{\partial z^2} + f \tag{5.11}$$

The period-averaged pore pressure is defined as

$$\overline{p} = \frac{1}{T}\int_t^{t+T} p dt \tag{5.12}$$

where T is the wave period. Eq. 5.11 is a diffusion equation with a source term f which is the amount of pore water pressure generated per unit time and per unit volume. Although from the derivation of the Eqs. 5.8 5.10 and 5.11, f should only be a function of time t, McDougal et al. (1989) suggested that in general f can be considered to be a function of both time t and space variable z. Careful examination of Eq. 5.11 reveals that the excessive pore water pressure is generated through the source term f and spreads with sediment depth through the diffusion process where c_v plays the role of diffusion coefficient (Sumer and Fredsøe 2002).

In order to solve Eq. 5.11, the following boundary conditions and initial conditions are needed:

$$\overline{p}(z,0) = \overline{p}(0,t) = 0 \tag{5.13}$$

$$\frac{\partial \overline{p}(h,t)}{\partial z} = 0 \tag{5.14}$$

where h is the depth of the sediment. When the sediment is very deep, i.e., $h \to +\infty$, Eq. 5.14 still holds.

The source term f for the excessive pore water pressure generation comes from the cyclic shear of the soil. It is important to know the normal and shear stresses in the soil due to waves beforehand since most of the models for the source term f depend on the stress state of the soil. Analytical solutions for wave-induced stresses in sea bed sediment have been developed by researchers (Yamamoto et al. 1978; Madsen 1978; Okusa 1985; Jeng and Hsu 1996). In Jeng and Hsu (1996), the amplitudes of the oscillatory pore water pressure and the shear stress for a saturated, isotropic sea bed of finite thickness are given by

$$p_0 = \frac{P_b}{1-2\mu}\left[(1-2\mu)\left(C_2 e^{-kz} - C_4 e^{kz}\right) + (1-\mu)\left(\delta^2 - k^2\right)\left(C_5 e^{-\delta z} - C_6 e^{\delta z}\right)\right] \tag{5.15}$$

$$\tau_0 = P_b \left[(C_1 - C_2 kz)\, e^{-} kz - (C_3 - C_4 kz)\, e^{kz} + k\delta \left(C_5 e^{-\delta z} - C_6 e^{\delta z} \right) \right] \tag{5.16}$$

where

$$P_b = \frac{\rho_w g H}{2 \cosh kd} \tag{5.17}$$

is the amplitude of the dynamic wave pressure on the bottom of the sea bed. Here, the ρ_w is the density of water, H is the wave height, k is the wave number, and d is the water depth. The coefficients C_1 to C_6 and the parameter δ can be found in Jeng and Hsu (1996).

There are two categories of mechanisms, namely nonlinear and linear mechanisms, which can be used to model the source term. Both categories are listed below.

Nonlinear Pore Water Generation Mechanism

De Alba et al. (1976) related the excessive pore water generation with the number of load cycles in a simple shear test. The equation is given as

$$\frac{p_g}{\sigma_0^{'}} = \frac{1}{2} + \frac{1}{\pi} \sin^{-1} \left[2 \left(\frac{N}{N_1} \right)^{\frac{1}{\theta}} - 1 \right] \tag{5.18}$$

where p_g is the amount of excessive pore water pressure generated, $\sigma_0^{'}$ is the initial effective stress, N is the number of cyclic loading, N_l is the number of cycles to liquefaction. θ is a shape factor which is suggested to have a value of 0.7 by Seed et al. (1975). The relationship given by Eq. 5.18 with different values of θ is plotted in Fig. 5.1.

The source term for pressure generation should be

$$\begin{aligned} f &= \frac{\partial p_g}{\partial t} \\ &= \frac{2\sigma_0^{'} \left(\frac{t}{TN_l} \right)^{\frac{1}{\theta}-1}}{\pi \sqrt{1 - \left[1 - 2 \left(\frac{t}{TN_l} \right)^{\frac{1}{\theta}} \right]^2}\, TN_l\theta} \end{aligned}$$

where t is time and T is the period of the cyclic loading.

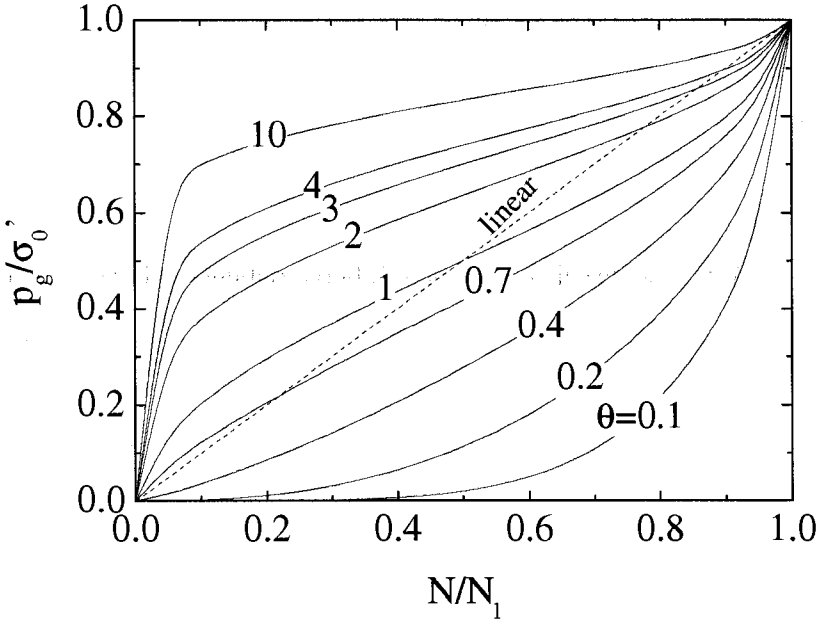

Figure 5.1: Excessive Pore Water Pressure Generation as a Function of Cyclic Load Number

Linear Pore Water Generation Mechanism

The nonlinear mechanism from the experiment can be simplified to get the linear approximation. In Fig. 5.1, when $\theta = 0.7$, it is very close to the linear relationship which is also plotted. Seed et al. (1975) proposed the linear mechanism as

$$\frac{p_g}{\sigma_0^{'}} = \frac{N}{N_l} \tag{5.19}$$

Thus, the source term for the pore water pressure generation should be

$$\begin{aligned} f &= \frac{\partial p_g}{\partial t} \\ &= \frac{\partial}{\partial t}\left(\sigma_0^{'}\frac{t}{TN_l}\right) \\ &= \frac{\sigma_0^{'}}{TN_l} \end{aligned}$$

For both mechanisms, the number of cyclic loadings to liquefaction N_l is a function of the cyclic shear stress ratio (Seed and Booker 1978)

$$N_l = \left(\frac{\tau}{\alpha\sigma_0^{'}}\right)^{-\frac{1}{\beta}} \tag{5.20}$$

where τ is the amplitude of the shear stress due to the cyclic loading and the two dimensionless parameters α and β are functions of the soil type and the relative density.

5.3 Numerical Simulation of One-Dimensional Excessive Pore Pressure Buildup Process

Even the simplified solutions to the analytical model introduced in this chapter are complicated, and some assumptions such as isotropic can not be satisfied in real world. Analytical approach is not always easy to be used. In this section, a numerical model is developed for the general one-

dimensional seabed response under waves. The results are used to compare with those from the analytical solutions.

The residual pore water pressure equation is solved by using the open source CFD package OpenFOAM OpenCFD (2006). This package is designed to solve partial differential equations (PDEs) as long as the PDEs can be written in the specified format. Differential operators, such as time derivative, Laplacican operator, and divergence, are implemented in the code. OpenFOAM uses finite volume method to solve the equations. The residual pore water pressure equation is a simple diffusion equation with a source term. It can be easily solved in OpenFOAM as follows.

```
fvMatrix PEqn
(
    fvm::ddt(P)
  - fvm::laplacian(C_nu,P)
 ==
    src
);

PEqn.solve();
```

The term `src` is the source term. The shear stresses used to define the source term can be calculated by using the numerical model introduced in chapter 4. This is the approach used by Cheng et al. (2001). The shear stress can also be calculated by using the analytical solution of oscillatory response of sea bed due to water waves (Jeng and Hsu 1996). Both approaches will give the same results. For simplicity, the shear stresses and therefore the source term are defined by the analytical solution. The schemes to discretize each term is defined in the file `fvScheme` which is listed below.

```
ddtSchemes
{
    default Euler;
}

gradSchemes
{
    default          Gauss linear;
    grad(V)          Gauss linear;
}

divSchemes
{
    default          none;
    div(V)       Gauss linear;
}

laplacianSchemes
{
    default          none;
    laplacian(V) Gauss linear corrected;
}

interpolationSchemes
{
    default          linear;
```

```
}

snGradSchemes
{
    default         corrected;
}
```

Here, the time derivative is discretized by using the Euler method, and the Laplacian operator is discretized by using the Gauss theorem and a second order linear correction for the non-orthogonality of the mesh. The details of each entry can be found in the manual of OpenFOAM.

5.4 Analytical Solution of One-Dimensional Excessive Pore Pressure Buildup Model

Jeng et al. (2007) gives the analytical solutions to the excessive pore pressure generation model. Under the conditions of finite depth, shallow and deep soil, the solutions can be expressed in different forms. The details of the derivation can be found in Jeng et al. (2007). In this section, only the results are listed. For the deep soil condition, the result given by Jeng et al. (2007) is not easy to use. Based on this, a simplified estimation is proposed in this section using the asymptotic method. Some errors in their paper are pointed out. Calculations are carried out to estimate the time scale and maximum pressure depth.

The analytical solutions depend on the relative depth of the sediment, d/L, which is the ratio between the sediment depth and the water wave length. Different authors have various criteria for the relative depth (McDougal et al. 1989; Jeng et al. 2007). Table 5.1 lists the three regimes by different authors. There are no clear-cut between different regimes, and both criteria are applicable.

Table 5.1: Criteria for the Relative Depth

	McDougal et al. (1989)	Jeng et al. (2007)
shallow	$d/L < 1/20$	$d/L < 1/10$
finite	$1/20 < d/L < 1/2$	$1/10 < d/L < 3/10$
deep	$d/L > 1/2$	$d/L > 3/10$

For finite and shallow soil depth, it is easy to solve the boundary value problem by using Fourier series expansion method. For deep soil depth, Laplace transformation can be used for the problem in the semi-infinite space.

5.4.1 Finite Depth Soil Solution

For the finite depth soil model, the residual pore water pressure can be expressed as

$$p = \sum_{n=1}^{\infty} a_n \left(1 - e^{-c_v k_n^2 t/h^2}\right) \sin\left(\frac{k_n z}{h}\right) \tag{5.21}$$

$$a_n = \frac{2h}{c_v k_n^2} \int_0^h f(r) \sin\left(\frac{k_n r}{h}\right) dr \tag{5.22}$$

where f is the general source term as in the last section, and $k_n = \frac{(2n-1)\pi}{2}$.

5.4.2 Shallow Soil Solution

For shallow soil, where the relative soil depth $h/L < 0.1$, the wave-induced shear stress can be approximated as

$$\tau = mP_b z \tag{5.23}$$

where the definition of m can be found in Jeng et al. (2007). Then the source term f can be approximated as

$$f = az \tag{5.24}$$

where

$$a = \frac{(1+2K_0)\,\gamma'}{3T}\left[\frac{2mP_b}{\alpha\,(1+2K_0)\,\gamma'}\right]^{\frac{1}{\beta}} \tag{5.25}$$

Then the excessive pore water pressure can be written using a Fourier series as

$$p = \frac{a}{2c_v}\left[\left(h^2 z - \frac{z^3}{3}\right) - \sum_{n=1}^{\infty} a_n e^{-c_v k_n^2 t/h^2} \sin\left(\frac{k_n z}{h}\right)\right] \tag{5.26}$$

$$a_n = \frac{2}{h}\int_0^h \left(h^2 r - \frac{r^3}{3}\right) \sin\left(\frac{k_n r}{h}\right) dr \tag{5.27}$$

Jeng et al. (2007) did not give the final form of the Fourier series coefficients a_n. It is straight forward to give a closed form

$$a_n = \frac{4h^3}{3k_n^4}\left[3\sin k_n - k_n\left(3 + k_n^2\right)\cos k_n\right] \tag{5.28}$$

5.4.3 Deep Soil Solution

For deep soil, where the relative soil depth $h/L > 0.3$, the source term can be approximated as

$$f = bze^{-\lambda z} \tag{5.29}$$

where

$$\lambda = \frac{k}{\beta} \tag{5.30}$$

and In Jeng et al. (2007), b is defined as

$$b = \alpha\left(\frac{k}{m}\right)^{\frac{1}{\beta}} \tag{5.31}$$

where m is defined the same as in the shallow soil solution. This is not correct since the wave induced shear stresses are different for shallow soil and deep soil conditions. For shallow soil, the shear stress can be approximated as a linear function of z with m as a linear coefficient. But for

deep soil, m can not be defined for the whole soil depth. This could be a typographical error. The correct form of b should has the form as in Jeng and Seymour (2007)

$$b = \frac{\gamma'}{T}\frac{1+2K_0}{3}\left[\frac{kP_b}{\alpha\gamma'^{\frac{1+2K_0}{3}}}\right]^{1/\beta} \tag{5.32}$$

Then the governing equation for the excessive pore water pressure can be written as

$$\frac{\partial p}{\partial t} = c_v\frac{\partial^2 p}{\partial z^2} + Aze^{-\lambda z} \tag{5.33}$$

with boundary conditions

$$p(0,t) = p(z,0) = 0 \quad \text{and} \quad \frac{\partial p}{\partial z}|_{z=\infty,t} = 0$$

In Jeng et al. (2007), the boundary condition at $z = \infty$ is set as $p(\infty, t) = 0$. It is incorrect, which will be shown later. Following the procedure in Jeng et al. (2007), Equation 5.33 is rescaled according to

$$\xi = c_v\lambda^2 t, \quad P = \frac{c_v\lambda^3 p}{A} \quad \text{and} \quad y = \lambda z$$

The rescaled equation and initial/boundary conditions are

$$\frac{\partial P}{\partial \xi} = \frac{\partial^2 P}{\partial y^2} + ye^{-y} \tag{5.34}$$

$$P(0,\xi) = P(y,0) = 0 \quad \text{and} \quad \frac{\partial P(\infty,\xi)}{\partial y} = 0$$

At steady state, the equation becomes

$$\frac{\partial^2 P}{\partial \xi^2} + ye^{-y} = 0 \tag{5.35}$$

Integrate the equation twice

$$P(y) = -e^{-y}(2+y) + C_1 y + C_2$$

The coefficients C_1 and C_2 are determined by the boundary conditions

$$P(y=0) = 0 : -e^{-0}(2+0) + C_1 * 0 + C_2 = 0 \quad \Rightarrow \quad C_2 = 2$$

$$\frac{\partial P(y=\infty)}{\partial y} = 0 : e^{-0}(2+0) - e^{-0} + C_1 = 0 \quad \Rightarrow \quad C_1 = 0$$

If the boundary condition at $y = \infty$ is set as in Jeng et al. (2007), then

$$P(y=\infty) = 0 : -e^{-\infty}(2+\infty) + C_1 * \infty + 2 = 0$$

Then C_1 can not be determined which means the boundary condition is not suitable.

Thus, the steady state solution is

$$P(y,\xi) = 2\left[1 - \left(\frac{y}{2}+1\right)e^{-y}\right] \tag{5.36}$$

The full solution to equation 5.34 can be derived using Laplace transformation method. Jeng et al. (2007) did not give the details of the derivation. The details of the laplace transformation and inverse transformation are given in Appendix B. The full solution is

$$P(y,\xi) = 2\left[1 - \left(\frac{y}{2}+1\right)e^{-y} - \frac{1}{\pi}\int_0^\infty \frac{e^{-r\xi}}{r(r+1)^2}\sin\sqrt{r}y dr\right] \tag{5.37}$$

The analytical solution in Jeng et al. (2007) involves improper integration over infinite domain. It is not easy to evaluate the solution. This difficulty is illustrated as follows.

The numerical evaluation of the improper integral in Eq. 5.37 needs some effort since the upper limit of the integration is $+\infty$ and the integrand is unbounded at $r = 0$. Fig. 5.2 shows the plots

of the integrand $f(r; y, \xi)$ as a function of r, where

$$f(r; y, \xi) = \frac{e^{-r\xi}}{r(r+1)^2} \sin(\sqrt{r}y) \tag{5.38}$$

The integrand is not zero only on a very narrow band near $r = 0$ and it goes to $+\infty$ very fast as $r \to 0$. This characteristic can be used to get some estimation using asymptotic method. On the other hand, numerical methods such as mid-point rule and Simpson's rule can be used. Due to the singularity, the iteration numbers to achieve desired accuracy needs to be very large. For comparison, the integral is evaluated using mid-point rule. The integration is from 0 to 1 since the contribution from 1 to $+\infty$ is essentially small. The interval is divided into 100 subintervals and the sum of the contributions from each subinterval is calculated. If desired accuracy is not achieved, the size of the subintervals is doubled. Suppose f_k is the result from step k, then the iteration relative error can be defined as

$$\text{Relative} \quad \text{Iteration} \quad \text{Error} = \frac{|f_k - f_{k-1}|}{|f_k|} \tag{5.39}$$

Fig. 5.3 shows the relative iteration error for fixed ξ and fixed y. For both cases, the interval needs to be divided into thousands of subintervals to achieve 2% accuracy. In order to achieve the same accuracy, for fixed ξ, the number of subintervals increases as y increases (deep into the bed). For fixed y, the number of subintervals does not show any pattern. In general, higher accuracy requires more subintervals.

It is not convenient to evaluate the excessive pore pressure using numerical integration. In this chapter, the solution is estimated using asymptotic expansion.

Asymptotic Analysis of the Long Term Behavior of Excessive Pore Pressure

When ξ is large, the asymptotic expansion will reveal the long term behavior. As seen from the previous section, when $\xi \to +\infty$, the only contribution comes from a small strip of $0 < r < \epsilon$,

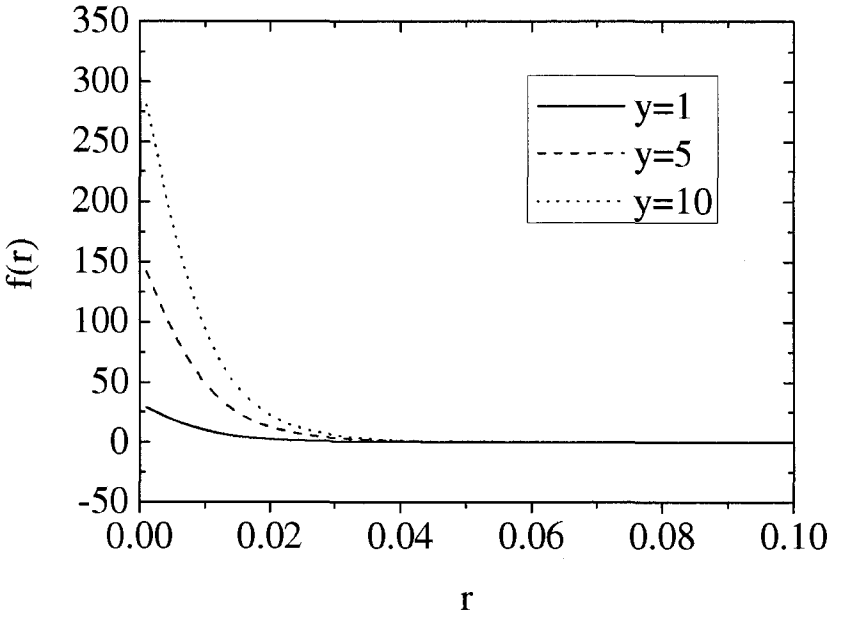

(a)

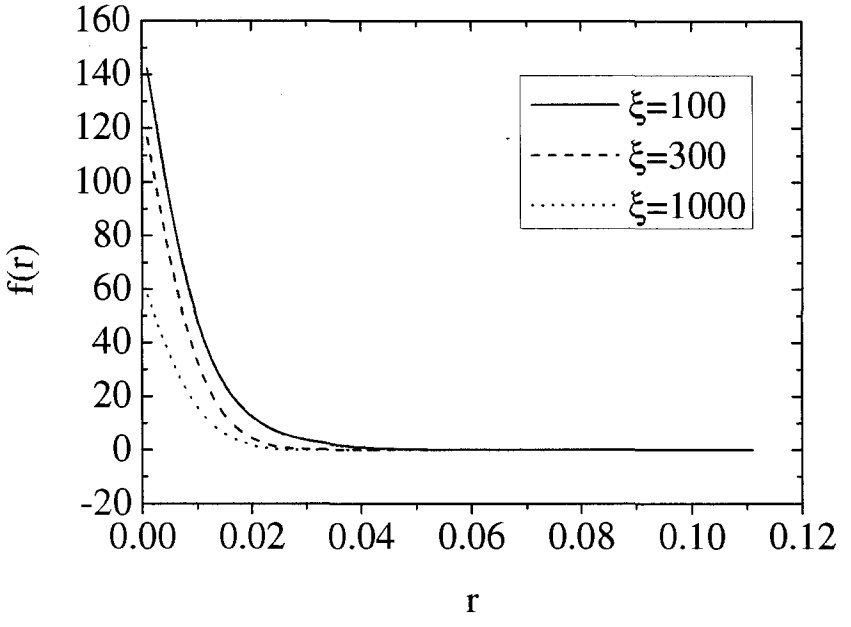

(b)

Figure 5.2: Plot of the Integrand: (a) Same ξ ($\xi = 100$) (b) Same y ($y = 5$)

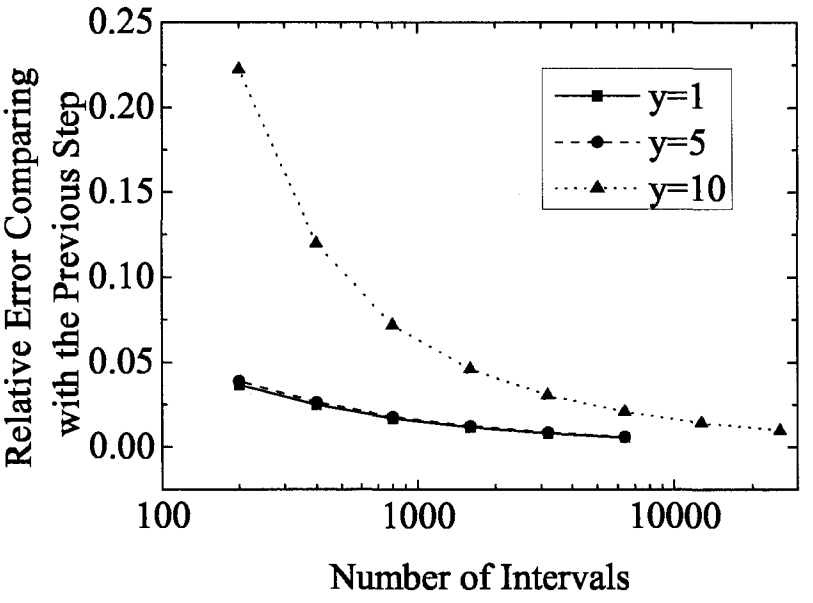

(a)

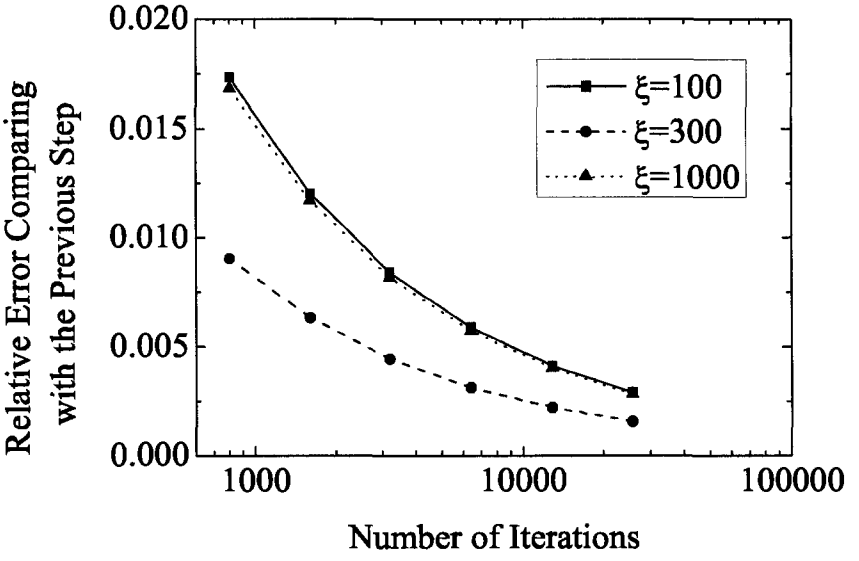

(b)

Figure 5.3: Convergence History of the Numerical Integration Using Mid-Point Method: (a) Same ξ ($\xi = 100$) (b) Same y ($y = 5$)

where $\epsilon \sim o(1)$. Then

$$\frac{1}{(r+1)^2} \sim (1-r)^2 \sim 1-2r \tag{5.40}$$

Plug into the integral,

$$\begin{aligned}
\int_0^\infty \frac{e^{-r\xi}}{r(r+1)^2}\sin(\sqrt{r}y)dr &\sim \int_0^\infty e^{-r\xi}\frac{1-2r}{r}\sin(\sqrt{r}y)dr \\
&= \int_0^\infty \frac{e^{-r\xi}}{r}\sin(\sqrt{r}y)dr - 2\int_0^\infty e^{-r\xi}\sin(\sqrt{r}y)dr \\
&\sim \pi \mathrm{erf}(\frac{y}{2\sqrt{\xi}}) - \frac{\sqrt{\pi}y}{\xi^{3/2}}e^{-\frac{y^2}{4\xi}}
\end{aligned}$$

So

$$P(y,\xi) \sim 2\left[1-\left(\frac{y}{2}+1\right)e^{-y} - \mathrm{erf}(\frac{y}{2\sqrt{\xi}}) + \frac{y}{\sqrt{\pi}\xi^{3/2}}e^{-\frac{y^2}{4\xi}}\right] \quad \text{as} \quad \xi \to +\infty \tag{5.41}$$

The error function can be approximated as

$$\mathrm{erf}(x) = \left[1-\exp\left(-x^2\frac{4/\pi + ax^2}{1+ax^2}\right)\right]^{\frac{1}{2}} \quad \text{for} \quad x \geq 0 \tag{5.42}$$

where

$$a = -\frac{8}{3\pi}\frac{\pi-3}{\pi-4} \tag{5.43}$$

In Fig. 5.4, the integral as a function of ξ and y is plotted. Both the results from numerical method and asymptotic method are shown. The results from both methods are almost identical. For the same y, the integral decreases to zero as time ξ increases to infinity. At the same time ξ, the integral increases to an asymptotic value as y goes deep into the soil.

Fig. 5.5 shows the relative error using the asymptotic estimation. The exact value of the integral is calculated using the numerical method with the successive change of the iterations less than 0.1%. The maximum relative error is around 1.5%. When y increases, i.e., deep into the soil, the relative error increases. When time ξ increases, the relative error also increases.

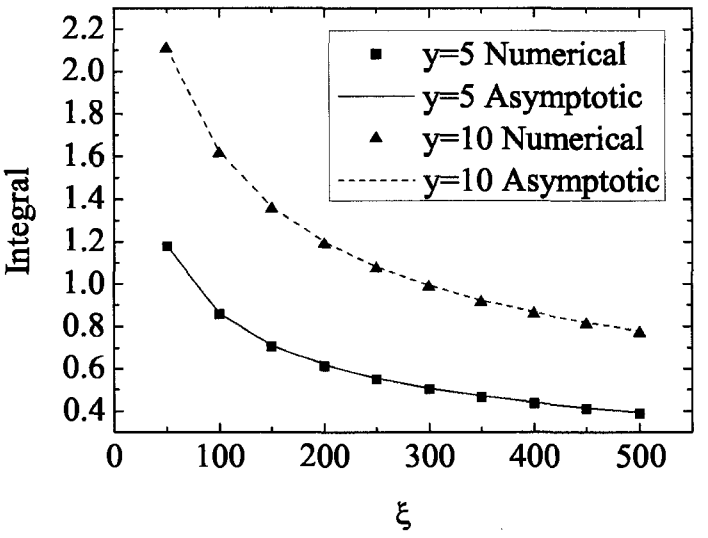

(a)

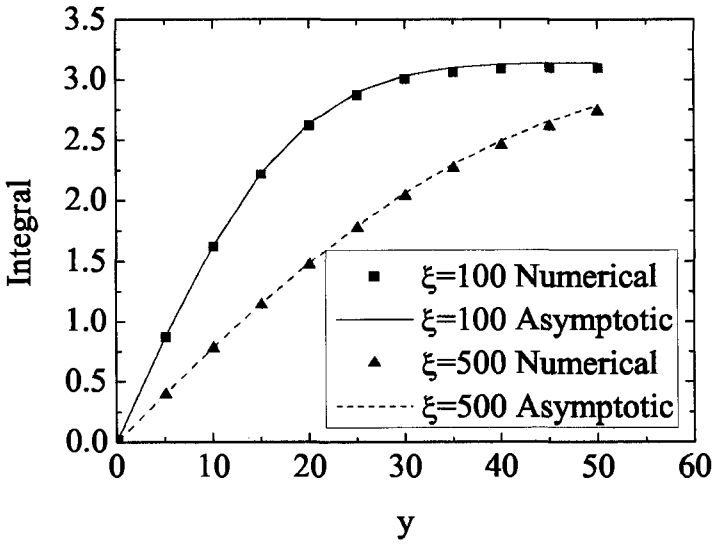

(b)

Figure 5.4: Integral Evaluation Using Numerical Method and Asymptotic Estimation: (a) Same ξ ($\xi = 100$) (b) Same y ($y = 5$)

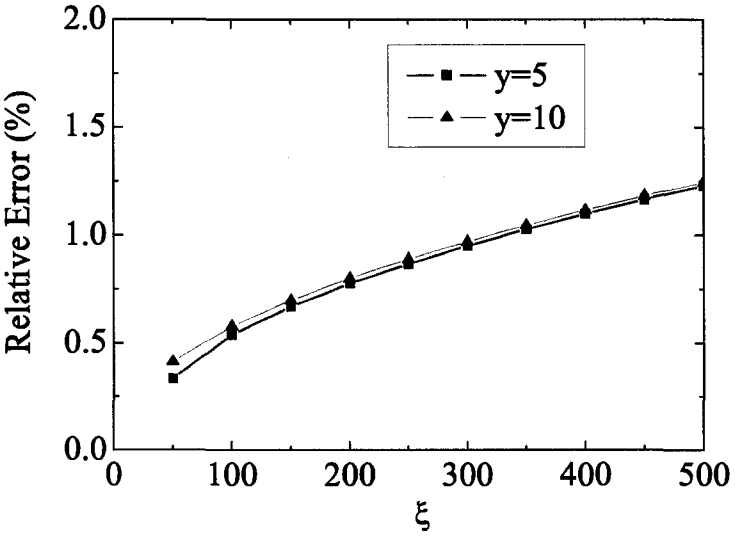

(a)

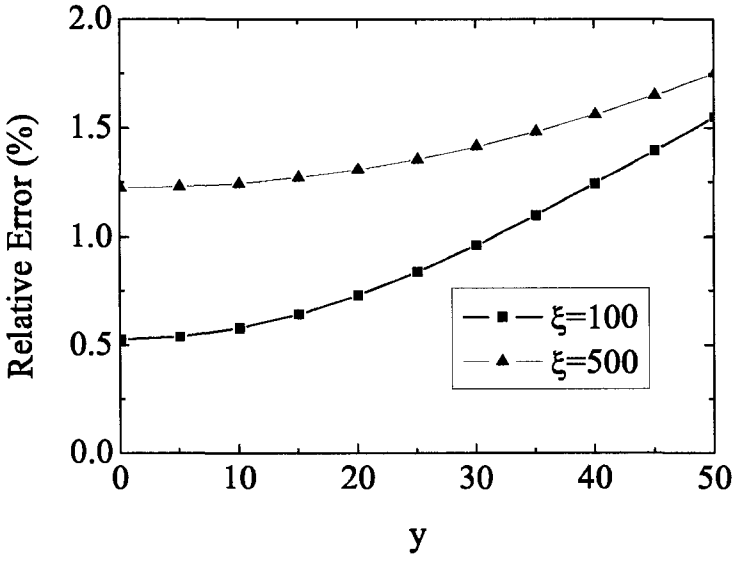

(b)

Figure 5.5: Relative Error Using the Asymptotic Approximation: (a) Same ξ ($\xi = 100$) (b) Same y ($y = 5$)

Due to the diffusion nature of the equation, it will take infinite time to reach the steady state. It is useful to get some information on where the pore pressure will reach 99% of the maximum value and for each depth, how long it will take to reach 99% of its steady state. Using the numerical method and asymptotic analysis, the excessive pore pressure is plotted in Fig. 5.6.

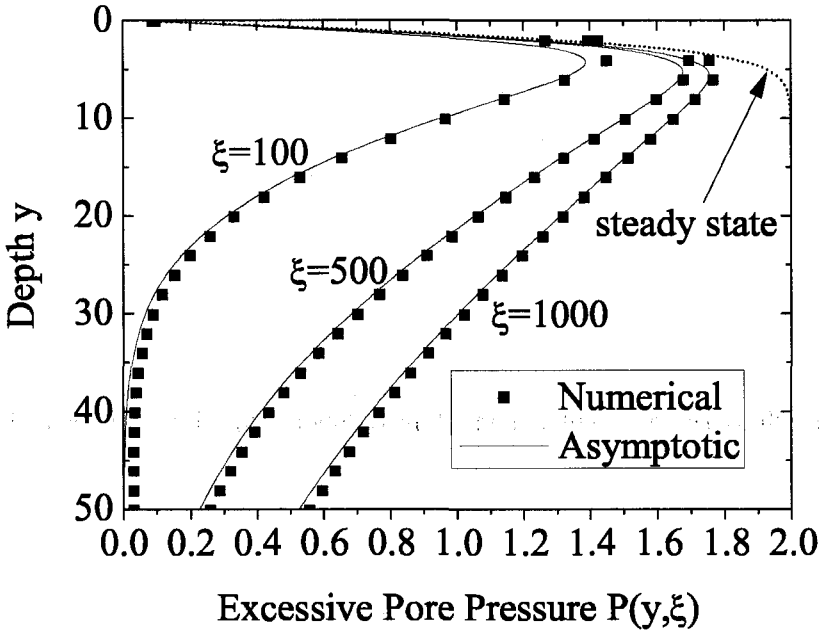

Figure 5.6: Excessive Pore Pressure Development for Deep Soil

At steady state, the position $y = y_{99\%}$ where the pore pressure reaches 99% of the maximum value can be solved using

$$2\left[1-\left(\frac{y}{2}+1\right)e^{-y}\right] = 2*0.99 \quad \Rightarrow \quad y_{99\%} = 5.99$$

At $y = y_{99\%}$, the time it takes for the excessive pore pressure to reach 99% of local maximum value (i.e. $P_{\max} = 1.98$) is about $\xi = 116533$. Fig. 5.7 shows the relationship between the time and the percentage of the local maximum pore pressure at $y = y_{99\%}$. With the percentage increasing, the time needed increases.

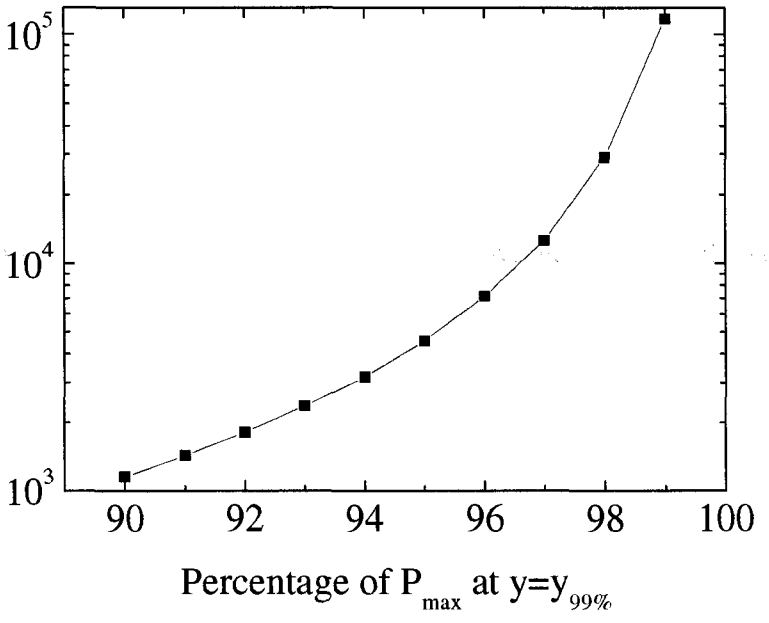

Figure 5.7: Excessive Pore Pressure Development at $y = y_{99\%}$

5.5 Comparison Between Numerical and Analytical Solutions

In this section, the results from both numerical and analytical solutions are compared for different soil and wave conditions. Three different depths of soil are calculated using the model developed in the previous sections. For shallow and finite depth soil models, comparisons are done between the numerical and analytical solutions. For deep soil model, asymptotic solution is also compared. Numerical simulations are carried out using a uniform grid along the depth. The total grid number for all simulations is 1000. The numerical accuracy can be improved when the total number of grid is increased, especially in the region where the residual pressure gradient is high. For the purpose of this chapter, 1000 grids along the depth give a good representation of the solution.

The test cases used in this chapter are from Clukey et al. (1985) where pressure accumulation experiments are done in a small wave tank. Wave-induced liquefaction data in this chapter is also used by many authors (McDougal et al. 1989; Cheng et al. 2001; Jeng et al. 2007). Pa'rameters for the soil used in the experiments are listed in Table 5.2. Only Run 3-1 of Clukey et al. (1985) is used in this chapter and the liquefaction results from the experiment is listed in Table 5.3. For the soil depth used in Clukey et al. (1985), $d = 0.84m$, and the wave length in Run 3-1, $L = 3.473m$, the relative soil depth is $d/L = 0.242$. This falls in the range of finite to deep soil. In order to verify the models in this chapter, soil depth d is set to be $0.11m$, $0.84m$ and $10m$ for shallow, finite, and deep soil models. Only when $d = 0.84m$, the model can be validated with experiments.

Table 5.2: Soil Parameters from Clukey et al. (1985)

Poisson's ration	0.49
Shear modulus (N/m^2)	5.6×10^5
Submerged weight (N/m^2	8.5×10^3
Permeability (m/s)	4×10^{-8}
Porosity	0.46
Lateral earth pressure coefficient	0.4
α	0.246
β	0.165
c_v	0.000156

Table 5.3: Liquefaction Experiment Results of Clukey et al. (1985) (Run 3-1)

Wave Period	Wave Height	Water Depth	Soil Depth	Residual Pore Pressure	
(s)	(m)	(m)	(m)	Depth (m)	Pressure(kN/m^2)
1.76	0.22	0.5	0.84	0.04	0.77
				0.10	0.96
				0.35	2.20
				0.47	2.54

5.5.1 Comparison for Shallow Soils

For the shallow soil model, since there is no measurement, the only comparison is between the results of numerical model and analytical model. Here, the soil depth is set as $0.11m$, corresponding to $d/L = 0.032$. The results are plotted in Fig. 5.8. Both results agree with each other. The pore pressure at the soil surface is zero due to the boundary condition. The maximum pore pressure is always at the impermeable boundary at $z = d$. The steady state solution is also plotted. From the figure, the result at $t = 100s$ is close to steady state.

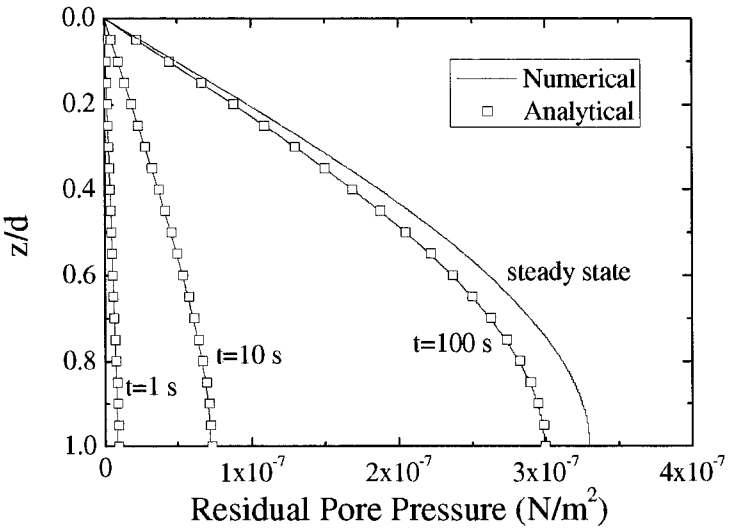

Figure 5.8: Comparison between Numerical and Analytical Solutions for Shallow Soil ($d/L = 0.032$)

5.5.2 Comparison for Finite Depth Soils

Fig. 5.9 shows the comparison between the results of the numerical model and the analytical model. Here the soil depth is set as the same as in the experiment of Clukey et al. (1985). Again, both results agree with each other very well. Steady state solution is also plotted. The solution at $t = 10000s$ is close to steady state. The shape of the residual pore pressure for finite depth soil is similar to that of shallow soil where residual pressure is zero at the surface and maximum pressure is achieved at the bottom. But for finite depth soil, the time to get steady state is longer than that of shallow depth.

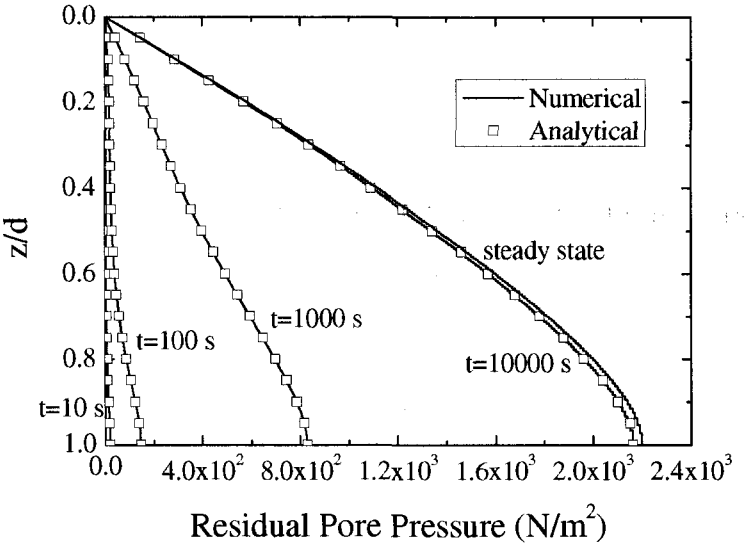

Figure 5.9: Comparison between Numerical and Analytical Solutions for Finite Depth Soil ($d/L = 0.242$)

For finite deposit soil, the experiment results can be used to validate the model. In Fig. 5.10, the data from Clukey et al. (1985) is plotted. The model used in this chapter gives fairly good results

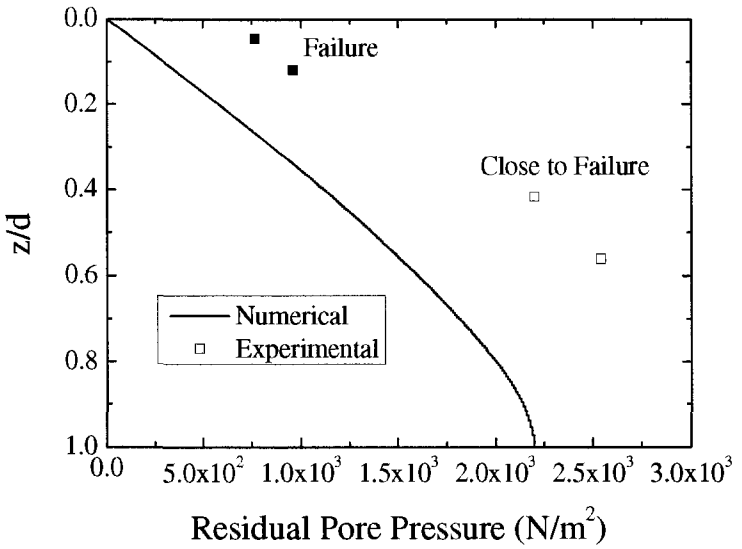

Figure 5.10: Comparison between Numerical and Experimental Results for Finite Depth Soil ($d/L = 0.242$)

5.5.3 Comparison for Deep Soils

For the deep soil case, the soil depth is set as $d = 10m$, which corresponds to $d/L = 2.879$. The comparison between the numerical solution and the analytical solution is plotted in Fig. 5.11. At steady state, the whole soil column has almost the same residual pressure except that at the top portion the pressure decreases to zero due the effect of diffusion. The time for the deep soil case to get to close to the steady state is far more than the previous two cases (shallow and finite depth). From the figure, at $t = 100000s$, the maximum pore pressure almost reached its final state. The majority part of the soil column below that point is still far away from steady state.

The comparison is also done between the numerical results and the asymptotic solutions. It is plotted in Fig. 5.12. The agreement is clearly shown in the figure. The asymptotic solution proposed in this chapter can be used to get a faster solution of the problem.

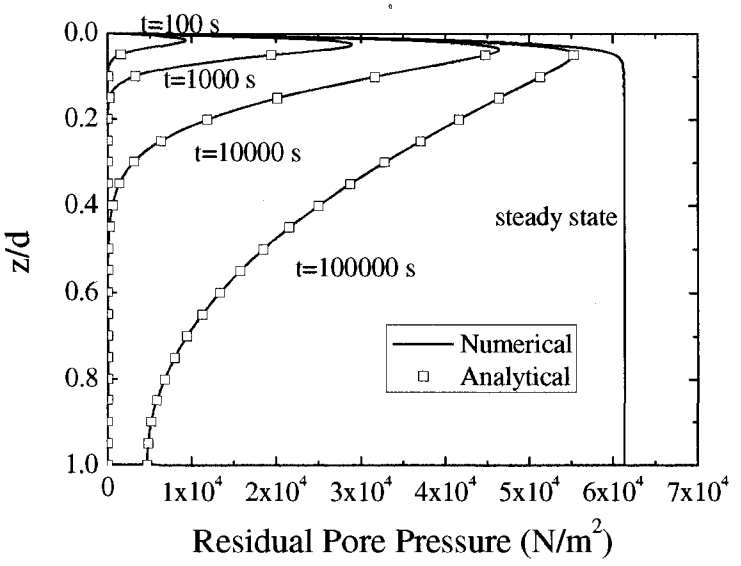

Figure 5.11: Comparison between Numerical and Analytical Solutions for Deep Soil ($d/L = 2.879$)

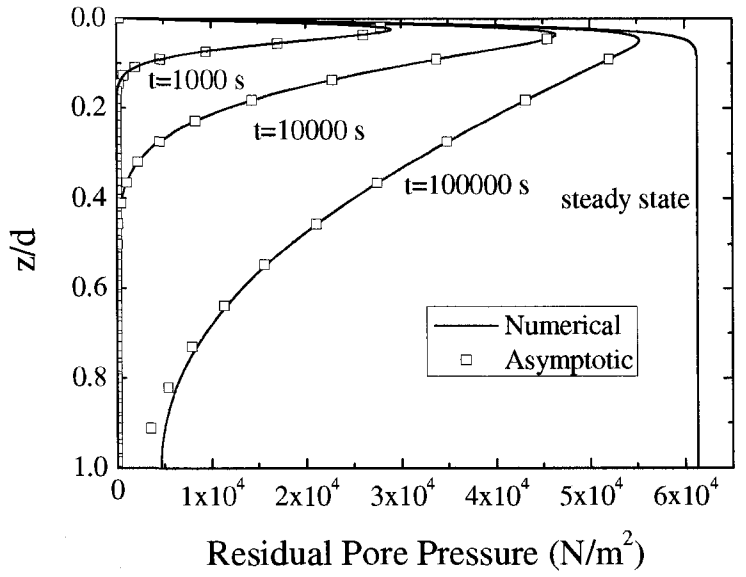

Figure 5.12: Comparison between Numerical and Asymptotic Solutions for Deep Soil ($d/L = 2.879$)

5.6 Numerical Model For Phase-Resolved Residual Pore Pressure and Liquefaction Potential Under Waves

The one-dimensional model introduced in the previous sections is only for the period-averaged residual pore pressure. It is applicable when the interaction is only between the wave and the seabed. In reality, the situation will be more complicated and the application of the one-dimensional model is limited. In engineering practice, it is important to know the liquefaction potential around the structure foundation or pipe lines. Because of the presence of these structures, the water wave field in the vicinity will be changed. Therefore, the wave-induced shear stress in the soil will also be changed. With one-dimensional model, it is impossible to capture the interactions between waves, structure, and sea bed. The three-dimensional numerical model developed in Chapter 4 has been used to investigate the oscillatory response of the sea bed under waves. In this section, a tentative effort is made to modify the model to study the residual response of the seabed.

The governing equation for the force balance of the soil is the same as Eq. 5.1. For the storage equation, an extra source term corresponding to the excessive pore pressure generation is added. The new storage equation has the form

$$\frac{n}{K'}\frac{\partial p}{\partial t} + \frac{\partial}{\partial t}(\nabla \cdot \mathbf{v}) = \frac{k}{\gamma}\nabla^2 p + \frac{n}{K'}f \tag{5.44}$$

where f is given as in the previous section for the one-dimensional period averaged model.

5.6.1 Two-Dimensional Test Case for the Experiment by Clukey et al. (1985)

Fig. 5.13 shows the domain of the problem. The depth of the soil is $0.84 \quad m$ and the length of the domain is set as the water wave length. Left and right boundaries are periodic. The pressure at the bed surface is set as the progressive water wave pressure. At the bottom, slip boundary condition is set for the displacement and zero gradient is set for the pressure (i.e., impermeable).

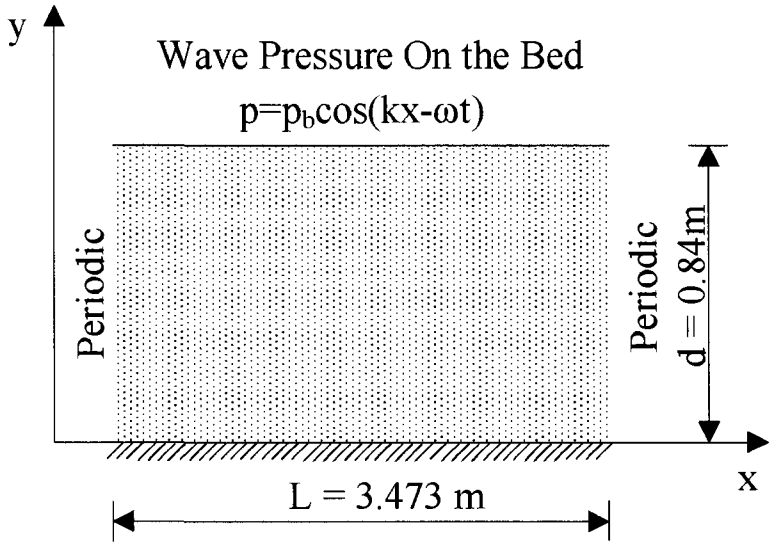

Figure 5.13: Schematic View for the 2D Residual Liquefaction Test Case

Total simulation time for this case is $20T$, where T is the wave period. In Fig. 5.14 and Fig. 5.15, both the water wave pressure field and the pore pressure field are plotted for different moments during one wave period. At the beginning of simulation, not too much residual pressure has been generated. The pressure field is similar to that of momentary liquefaction, i.e., the source term effect is negligible. With time increases, the pore water pressure generated is much more than which is dissipated. Except for the near surface region, the whole soil column almost has uniform residual pore pressure (see Fig. 5.15).

Two probe points are placed in the center plane ($x = 1.737m$) of the simulation domain to record the time development of residual pore pressure. Those two probe points are at $z = -0.1m$ and $z = -0.8m$. The recorded residual pore pressure is plotted in Fig. 5.16. Also plotted is the period-average of both signals. At both probe points, the pressure signal oscillates around the trend line (the period-average). It is clear that the residual pore pressure increases to some asymptotic value for both depth. The asymptotic value for $z = -0.1m$ is lower than that for $z = -0.8m$ which is as expected by analytical solution.

In Fig. 5.17, the residual pore pressure profiles at the center plane $x = 1.737m$ in one typical wave period are plotted. The data plotted is from the last simulated wave period ($t = 19T \rightarrow 20T$).

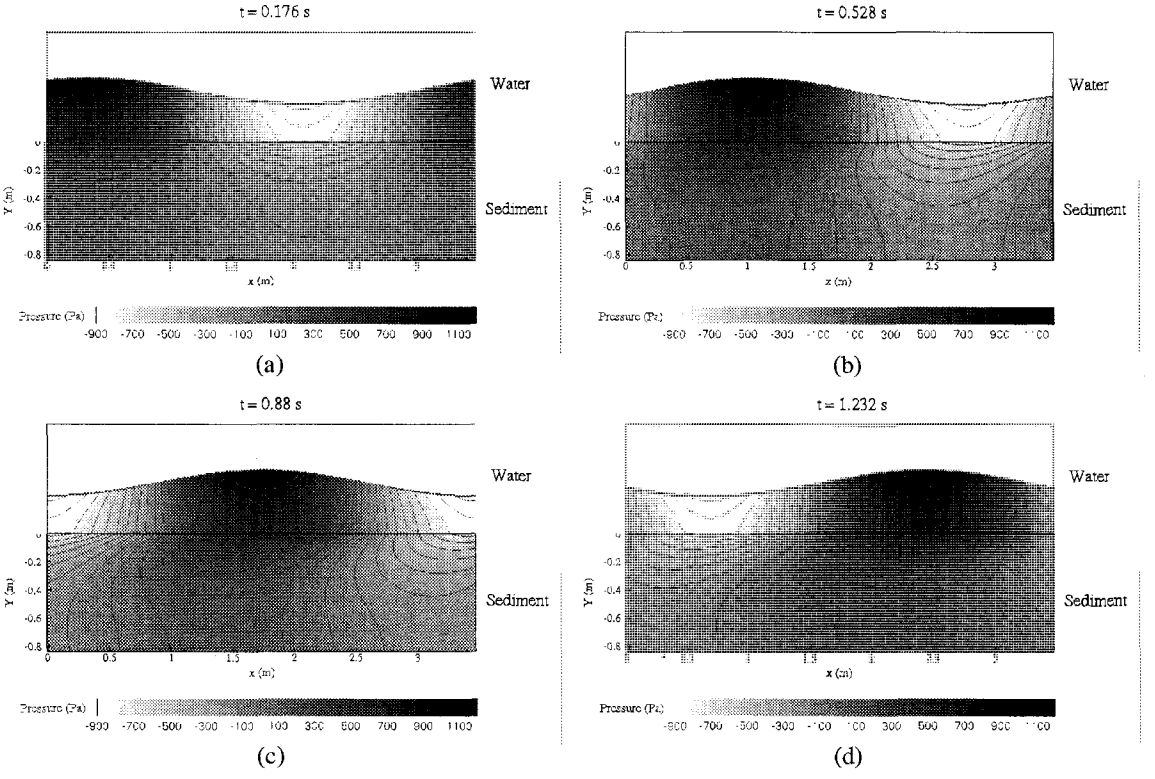

Figure 5.14: Excessive Pore Pressure under Waves in One Typical Period (Early Stage) : (a) $t = t_0 + \frac{T}{10}$ (b) $t = t_0 + \frac{3T}{10}$ (c) $t = t_0 + \frac{5T}{10}$ (d) $t = t_0 + \frac{7T}{10}$

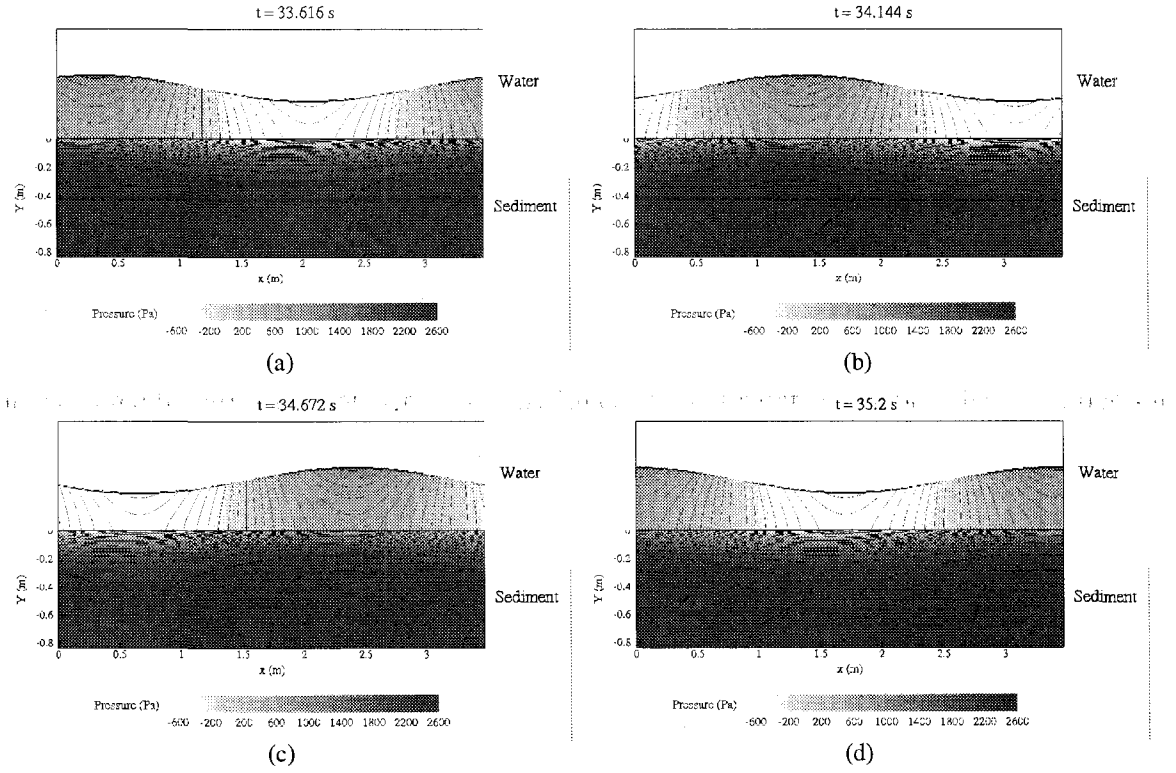

Figure 5.15: Excessive Pore Pressure under Waves in One Typical Period (Later Stage)): (a) $t = t_0 + \frac{T}{10}$ (b) $t = t_0 + \frac{3T}{10}$ (c) $t = t_0 + \frac{5T}{10}$ (d) $t = t_0 + \frac{7T}{10}$

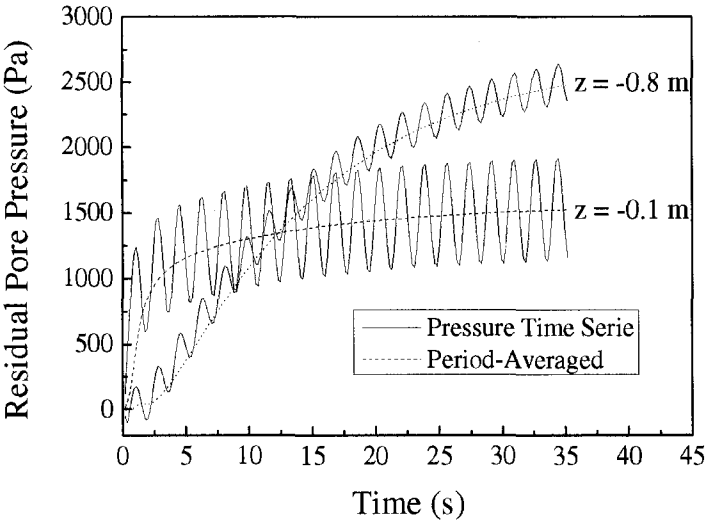

Figure 5.16: Time Series For the Residual Pore Pressure at Different Depth

From the figure, the residual pore pressure during this last simulated wave period still oscillates but is close to steady state solution. At the upper portion near the bed surface, the amplitude of the pore pressure oscillation (p_1) is larger than that at the lower portion of the soil (p_2).

The period-averaged residual pore pressure profile is plotted in Fig. 5.18. For comparison, the one-dimensional analytical solution is also plotted. A large amount of difference between the one-dimensional and two-dimensional results is observed. However, the result from the two-dimensional model is closer to the experiment data. One reason could be that the one-dimensional model neglects the variation along the x direction. The neglect of x direction variation will change the shear stress which is a function of $\partial u/\partial x$ and therefore introduce error for residual pore pressure.

5.7 Discussion

The one-dimensional residual pore pressure buildup model used in this chapter is only for the period-averaged pressure. It is only valid in the sense of averaging. This model is good for the

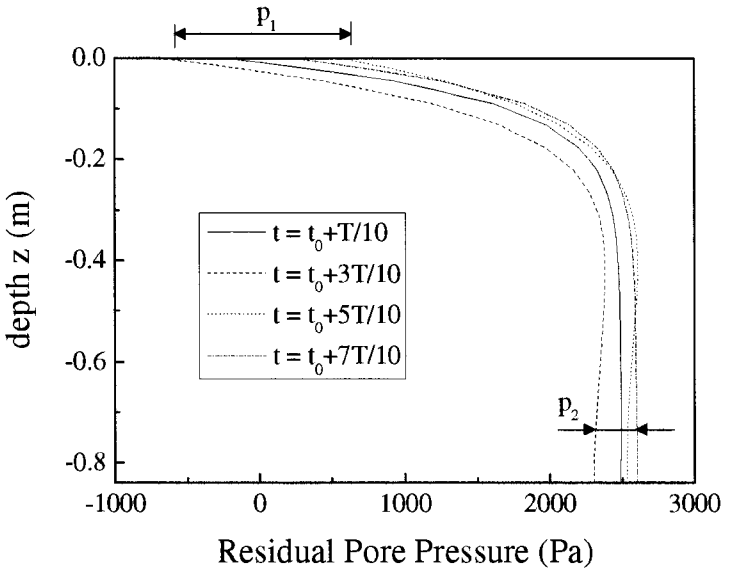

Figure 5.17: Residual Pore Pressure Profiles at the Center Plane in One Typical Wave Period

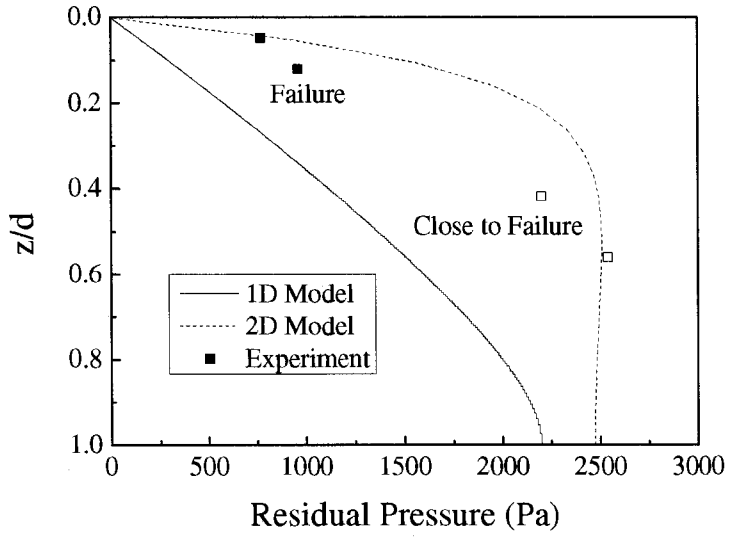

Figure 5.18: Schematic View for the 2D Residual Liquefaction Test Case

investigation of the liquefaction trend in the soil. The detailed pore pressure buildup process (oscillation around the mean value) is lost.

The classification of three different regimes of soil (shallow, finite depth, and deep) are not so apparent. For shallow soil, the shear stress induced by the waves should be approximately linear with the depth. For deep soil, the shear stress should be able to be written in the general form ye^{-y}. If the approximated shear stress is far away from these forms, the proposed solutions can not be used. As pointed out by Cheng et al. (2001), the solutions are sensitive to the shear stress (the sensitivity depends on the soil regime and the parameter β), and different approximation of the shear stress will lead to huge difference in the solutions. In general, the finite depth model (with the full solution of the shear stress) is valid for all three regimes. No approximation is made for the shear stress, therefore, it can be used as a general solution.

The model used in this chapter depends on the coefficients from the experiment (especially α and β). These coefficients are only for the soil used in the experiment. When soil conditions change, these coefficients should also change. As mentioned earlier, the results are very sensitive to these coefficients. More experimental work should be done to give good description of these coefficients.

5.8 Conclusion

In this chapter, a one-dimensional period-averaged residual pore pressure model is introduced. The governing equation for the residual pore water pressure is a diffusion equation with a source term which represents the generation of the pore pressure. Although this source term comes from the analytical derivation of the equation, it is given by experiments. Linear and nonlinear forms of the source term were proposed by De Alba et al. (1976). For nonlinear form of the source term, the governing equation can only be solved numerically while for linear form of the source term, it can be solve both numerically and analytically. According to the relative depth d/L, the soil can be classified into three different regimes (shallow, finite depth, and deep soils). In each regime,

the analytical solution for wave induced shear stress is used for the source term. Based on the solutions given by Jeng et al. (2007), some errors are corrected in this chapter and revised forms of the solutions are given.

For deep soil model, the solution by Jeng et al. (2007) has an improper integral and is not easy to use. The difficulty to evaluate the solution numerically due to the singularities is illustrated in this chapter with the help of examples. Based on the form of the improper integral, an asymptotic solution is proposed in this chapter. This asymptotic solution has a closed form and is easy to evaluate.

Besides an analytical approach, numerical solutions for the residual pore water pressure are also given by using the differential equation solver package OpenFOAM. The results from analytical solutions, numerical solutions, and asymptotic estimations are compared. Perfect agreement has been achieved. For finite depth soil, the experiment data of Clukey et al. (1985) are used for validation. The models in this chapter predict the liquefaction fairly well.

A numerical model is also introduced for the phase-resolved residual pore pressure. The basic idea of adding a source term to the governing equation is used. The source term has the same form as that of the period-averaged residual pore pressure model. Test cases show that this model gives good results when comparing with the one-dimensional period-averaged model.

Chapter 6

Summary

This thesis addresses two mechanisms in the interaction between water, sediment, and structures, namely scour and liquefaction. Both mechanisms are closely related to each other. Numerical models are developed to simulate and study the process.

6.1 Numerical Models for Scour

For scour, two-dimensional and three-dimensional models are developed. Two-dimensional model is suitable for large scale and long term scour process, while the three-dimensional model is suitable for detailed local scour around structures.

6.1.1 Two-Dimensional Scour Model

The coupled model of two-dimensional SWEs and sediment transport on unstructured mesh was implemented for scour problems on complex domains. This coupled modeling approach is necessary when the scour process is rapid. When the scour process is slow (such as long term aggradation/degradation of natural rivers), both the usual quasi-steady approach and the coupled approach can give good results. However, the numerical stability of the quasi-steady approach will present difficulty. High order discretization of the Exner equation may lead to non-physical oscillations which could be incorrectly interpreted as ripples and sand waves. Low order discretization of the Exner equation may under-estimate the amplitude of the real sand wave or even smear it out. The hyperbolic nature of the Exner equation (even though there is dispersion effect in the equation) makes it possible to couple it with SWEs and to use Godunov schemes. The coupled model with

a higher order Godunov scheme proposed in this thesis can capture the real wave accurately while controlling the growth of non-physical oscillations.

An asymptotic analysis was done to gain an insight about the wave speed structure and to construct an explicit expression for the Roe's flux. It also gave a fast and accurate evaluation of the eigenvalues/vectors. Comparing to the numerical iteration method for the eigen-system, the asymptotic approximation is far more efficient. For the test case used in this paper, the average computational time can be reduced by approximately 64%.

The interpolation method of the TVD scheme used in the current numerical model for the upwind ratio of consecutive gradients is based on the virtual upwind node. The basic assumption is that the gradient from upwind node to downwind node is the same as that from center node to downwind node. This assumption simplifies the calculation and reduces the stencil. Future research is needed on the comparison of different interpolation methods and TVD schemes.

6.1.2 Three-Dimensional Scour Model

Numerical model FOAMSCOUR for local scour with free surface and automatic mesh deformation is proposed. The turbulence model used is the simple two equation $k - \epsilon$ model. Other turbulence models, even large eddy simulation, can be used to improve the accuracy of the fluid flow field simulation. All these models are readily implemented in OpenFOAM. The free surface is modeled by VOF method while the scour process is modeled by moving mesh method. These two methods for moving boundaries(free surface and bed) are coupled together. Each method has its merits and shortcomings. Eulerian approach can be used to capture the complex scour profiles. Flow field is coupled with sediment transport (both bed load and suspended load) using a quasi-steady approach. Parallel computations are used to reduce the CPU time which is usually tremendously large for morphological simulations.

Numerical simulations for turbulent wall jet scour and wave scour around large vertical cylinder are carried out and compared with experiments. Good results have been obtained using the proposed modeling approach. Velocity field and other flow field characteristics compare fairly

well with experimental observations. The maximum scour depths and local scour profile fit well with the experiment data. Further research is needed to investigate the effects of turbulence model for free surface waves (especially for near breaking and breaking waves) and to study the possibility of using an Eulerian approach for morphological modeling.

For the effect of the free water surface, the following conclusions are drawn. For the submerged wall jet case, the water depth in the flow domain is much bigger than the jet opening and the free surface changes very slowly. This makes the rigid-lid approximation a reasonable one. For scour around slender piles under waves, the rigid-lid assumption is also valid since the most important mechanism here is the vortex shedding and horseshoe vortex. However, for the wave-induced scour around large piles, it is unreasonable to use the rigid-lid approximation since the dominant mechanism here is the phase-resolved component of the wave flow and the steady streaming.

In the current numerical model, the two moving surfaces (water free surface and moving bed) are captured by different approaches, namely Eulerian and Lagrangian approaches. The free surface is solved by the CICSAM VOF scheme, which is an Eulerian approach. The moving bed is captured by the mesh deformation method, which is a Lagrangian approach. The scour test cases in the paper are relatively simple. For more complicated problems, if there are objects interacting with the fluid phase and the bed, the moving mesh technique will not be appropriate. The interface between the object, water and bed is very complicated and changing with time. Simply moving the grid point along the interface will be not feasible. For such cases, the Eulerian approach (VOF or LSM) can be used to implicitly track the interface. This could provide new research direction in the scour problem and currently is being explored by the authors.

There is some limitation when using the mesh deformation approach to capture the interaction of many phases. The mesh deformation approach is hard to implement with the presence of interaction between moving objects and the bed or when the boundary movement is irregular. Also, when the amplitude of the boundary movement is big enough, the mesh may be highly distorted, and the deteriorated mesh quality will make the computation difficult to converge, eventually leading to unstable solutions. In order to avoid these problems, the dynamic mesh approach should be

used. In the dynamic mesh approach, mesh cells can be split or merged when necessary. However, when comparing them with mesh deformation, the dynamic mesh approach is more difficult. Combining these two approaches can be promising for scour problems where the scour pattern is complicated and the scour/deposition depth is very large.

6.2 Numerical Models for Liquefaction

Two different liquefaction mechanisms (momentary and residual liquefactions) are considered in this thesis.

6.2.1 Momentary Liquefaction

The numerical model in this paper can solve the coupling problem between waves, object (structure) and sea bed response. The wave induced shear stress and pore pressure in the soil is governed by the Biot consolidation equation. The free surface is modeled by the VOF method and the water wave is generated by numerical wave maker boundary conditions. Instead of using the finite element method to do stress analysis inside the bed material (which is the traditional method used in geotechniques), an iterative numerical scheme is proposed to solve the Biot consolidation equation using finite volume method. The new scheme shows a fast convergence rate as well as a high accuracy. The coupling between water waves and the sea bed is through pressure and stress condition on common boundaries. Two numerical tests of the proposed scheme is carried out. First, the numerical case tests the consolidation solver part of the numerical model. Good agreement with analytical results is obtained. The second case is a 3D test to study the interaction between the waves, the sea bed and the object. A box is half buried in the wave tank. More complicated geometries can be simulated as well. From the results, excessive pore pressure of the sea bed as well as the liquefaction potential can be analyzed.

For geotechnical problems, a realistic stress-strain constitutive relationship is one of the most important aspects for the ability of the numerical model to reproduce real situations. In this thesis,

the simple linear isotropic elastic model is used to describe the soil skeleton. More advanced and accurate constitutive models (such as variable elasticity, elasto-plastic model and visco-plastic model, etc.) can be easily incorporated in the current numerical code. The anisotropic effect can also easily come into the model since the code is based on the tensorial description of the equations and anisotropic tensors can be included inside the differential operators.

In the three-dimensional test case, the object is assumed to be at fixed position during the computation. This is not always true since when liquefaction occurs, the soil can no longer support the object and the object will move. Even without liquefaction, the object could rotate or slide under the influence of fluid force. All these make the problem extremely complicated and it is impossible to include all factors into the numerical model. However, by fixing the object in one position, it is possible to investigate the possibility of liquefaction and analyze the dynamics of the system. This could be useful for engineers to design structures and foundations to prevent damage under extreme conditions.

6.2.2 Residual Liquefaction

One-dimensional period-averaged residual pore pressure model is introduced. The governing equation for the residual pore water pressure is a diffusion equation with a source term which represents the generation of the pore pressure. Although this source term comes from the analytical derivation of the equation, it is given by experiments. Linear and nonlinear forms of the source term were proposed in the literature. For a nonlinear form of the source term, the governing equation can only be solved numerically while for a linear form of the source term, it can be solve both numerically and analytically. According to the relative depth d/L, the soil can be classified into three different regimes (shallow, finite depth, and deep soils). In each regime, the analytical solution for the shear stress is used for the source term. Based on the solutions given by Jeng et al. (2007), some errors are corrected in this thesis, and revised forms of the solutions are given.

For the deep soil model, the solution by Jeng et al. (2007) has an improper integral and is not easy to use. The difficulty to evaluate the solution numerically due to the singularities is illustrated

in this thesis with examples. Based on the form of the improper integral, an asymptotic solution is proposed. This asymptotic solution has a closed form and is easy to evaluate.

Besides an analytical approach, numerical solutions for the residual pore water pressure are also given. The results from the analytical solutions, the numerical solutions, and the asymptotic estimations are compared. Perfect agreement has been achieved between both. For the finite depth soil, the experimental data of Clukey et al. (1985) are used for validation. The proposed model predicts liquefaction fairly well.

Appendix A

Asymptotic Analysis of Eigenvalues

A.1 Eigen-systems When $u_\xi \neq 0$

The regular expansion is used to approximate the roots of Eqn. 2.27. Assume

$$\lambda = \lambda_0 + \epsilon\lambda_1 + O(\epsilon^2) \tag{A.1}$$

Substituting Eqn. A.1 into Eqn. 2.27 and expanding give

$$\left[\left(1 - \frac{1}{Fr^2}\right)\lambda_0 - 2\lambda_0^2 + 3\lambda_0^3\right] + \left[1 - \lambda_0 + k\lambda_1 - 4\lambda_0\lambda_1 + 3\lambda_0^2\lambda_1\right]\epsilon + O(\epsilon^2) = 0 \tag{A.2}$$

Equating the coefficients of like powers of ϵ gives

$$\left(1 - \frac{1}{Fr^2}\right)\lambda_0 - 2\lambda_0^2 + 3\lambda_0^3 = 0 \tag{A.3}$$

$$1 - \lambda_0 + k\lambda_1 - 4\lambda_0\lambda_1 + 3\lambda_0^2\lambda_1 = 0 \tag{A.4}$$

Solving these equations gives the eigenvalues as

$$\lambda^{(1)} = \frac{\epsilon}{\frac{1}{Fr^2} - 1} \tag{A.5}$$

$$\lambda^{(2)} = 1 + \frac{1}{Fr} + \frac{\epsilon}{2\left(\frac{1}{Fr} + 1\right)} \tag{A.6}$$

$$\lambda^{(3)} = 1 - \frac{1}{Fr} - \frac{\epsilon}{2\left(\frac{1}{Fr} - 1\right)} \tag{A.7}$$

The regular expansion breaks down when $Fr = 1$. The region of non-uniformity is determined by comparing the successive terms in the expansion (Nayfeh 1981). So the order of $1 - 1/Fr^2$ is

$$1 - \frac{1}{Fr} = O(\frac{\epsilon}{1 - \frac{1}{Fr}}) \tag{A.8}$$

i.e.

$$1 - \frac{1}{Fr} = O(\epsilon^{\frac{1}{2}})$$

Also since

$$1 + \frac{1}{Fr} = O(1)$$

then

$$1 - \frac{1}{Fr^2} = O(\epsilon^{\frac{1}{2}})$$

Let

$$1 - \frac{1}{Fr^2} = \sigma\epsilon^{\frac{1}{2}} \qquad \text{where} \quad \sigma = O(1)$$

In order to get the right expansion in near critical flow regime, it is assumed that

$$\lambda = \lambda_0 + \epsilon^m\lambda_1 + \cdots \qquad m > 0 \tag{A.9}$$

Substituting Eqn. A.9 into Eqn. 2.27 gives

$$\begin{aligned}\left[\lambda_0^3 + 3\lambda_0^2\epsilon^m\lambda_1 + 3\lambda_0\epsilon^{2m}\lambda_1^2 + \cdots\right] - 2\left[\lambda_0^2 + 2\lambda_0\epsilon^m\lambda_1 + \epsilon^{2m}\lambda_1^2 + \cdots\right] \\ + \left[\lambda_0\sigma\epsilon^{\frac{1}{2}} - \lambda_0\epsilon + \sigma\epsilon^{m+\frac{1}{2}}\lambda_1 - \lambda_1\epsilon^{m+1} + \cdots\right] + \epsilon = 0\end{aligned} \tag{A.10}$$

For the proper balancing of terms in Eqn. A.10, $m = 1/2$ is chosen. Equating the same powers of ϵ gives

$$O(1): \quad \lambda_0^3 - 2\lambda_0^2 = 0 \quad \Rightarrow \quad \lambda_0 = 0 \quad \text{or} \quad \lambda_0 = 2 \tag{A.11}$$

$$O(\epsilon^{\frac{1}{2}}): \quad 3\lambda_0^2\lambda_1 - 4\lambda_0\lambda_1 + \lambda_0\sigma = 0 \tag{A.12}$$

For $\lambda_0 = 0$, Eqn. A.12 is satisfied automatically and λ_1 should be calculated through higher order terms. For $\lambda_0 = 2$, Eqn. A.12 gives

$$\lambda_1 = -\frac{\sigma}{3\lambda_0 - 4} = -\frac{\sigma}{2}$$

$$O(\epsilon): \quad 3\lambda_0\lambda_1^2 - 2\lambda_1^2 - \lambda_0 + \sigma\lambda_1 + 1 = 0 \tag{A.13}$$

For $\lambda_0 = 0$, Eqn. A.13 gives

$$\lambda_1 = \frac{\sigma \pm \sqrt{\sigma^2 + 8}}{4}$$

So in the region of $1 - \frac{1}{Fr^2} = O(\epsilon^{\frac{1}{2}})$, the eigenvalues are

$$\lambda^{(1)} = 2 - \frac{\sigma}{2}\epsilon^{\frac{1}{2}} = \frac{3}{2} + \frac{1}{2Fr^2}$$

$$\lambda^{(2)} = \frac{\sigma + \sqrt{\sigma^2 + 8}}{4}\epsilon^{\frac{1}{2}} = \frac{1}{4}\left[1 - \frac{1}{Fr^2} + \sqrt{\left(1 - \frac{1}{Fr^2}\right)^2 + 8\epsilon}\right]$$

$$\lambda^{(3)} = \frac{\sigma - \sqrt{\sigma^2 + 8}}{4}\epsilon^{\frac{1}{2}} = \frac{1}{4}\left[1 - \frac{1}{Fr^2} - \sqrt{\left(1 - \frac{1}{Fr^2}\right)^2 + 8\epsilon}\right]$$

These eigenvalues are similar to those in Lyn and Altinakar (2002).

A.2 Eigen-systems When $u_\xi = 0$

There are two sub-cases. When $u_\xi = 0$ and $u_\eta \neq 0$, the four eigenvalues are 0, 0, $-\sqrt{gh + gkv_\eta^2}$, and $\sqrt{gh + gkv_\eta^2}$. The right eigenvector matrix is

$$R = \begin{bmatrix} -1 & 0 & \frac{h}{kv_\eta^2} & \frac{h}{kv_\eta^2} \\ 0 & 0 & \frac{-h\sqrt{gh+gkv_\eta^2}}{kv_\eta^2} & \frac{h\sqrt{gh+gkv_\eta^2}}{kv_\eta^2} \\ 0 & 1 & \frac{h}{kv_\eta} & \frac{h}{kv_\eta} \\ 1 & 0 & 1 & 1 \end{bmatrix} \tag{A.14}$$

and left eigenvector matrix is

$$L = \begin{bmatrix} -\frac{kv_\eta^2}{h+kv_\eta^2} & 0 & 0 & \frac{h}{h+kv_\eta^2} \\ -\frac{hv_\eta^2}{h+kv_\eta^2} & 0 & 1 & -\frac{hv}{h+kv_\eta^2} \\ \frac{kv_\eta^2}{2h+2kv_\eta^2} & -\frac{kv_\eta^2}{2h\sqrt{g\left(h+kv_\eta^2\right)}} & 0 & \frac{kv_\eta^2}{2h+2kv_\eta^2} \\ \frac{kv_\eta^2}{2h+2kv_\eta^2} & \frac{kv_\eta^2}{2h\sqrt{g\left(h+kv_\eta^2\right)}} & 0 & \frac{kv_\eta^2}{2h+2kv_\eta^2} \end{bmatrix} \tag{A.15}$$

When $u_\xi = 0$ and $u_\eta = 0$, the four eigenvalues are 0, 0, $-\sqrt{gh}$, and $\sqrt{gh}$. The right eigenvector matrix is

$$R = \begin{bmatrix} -1 & 0 & -\frac{1}{\sqrt{gh}} & \frac{1}{\sqrt{gh}} \\ 0 & 0 & 1 & 1 \\ 0 & 1 & 0 & 0 \\ 1 & 0 & 0 & 0 \end{bmatrix} \tag{A.16}$$

and the left eigenvector matrix is

$$L = \begin{bmatrix} 0 & 0 & 0 & 1 \\ 0 & 0 & 1 & 0 \\ -\frac{\sqrt{gh}}{2} & \frac{1}{2} & 0 & -\frac{\sqrt{gh}}{2} \\ \frac{\sqrt{gh}}{2} & \frac{1}{2} & 0 & \frac{\sqrt{gh}}{2} \end{bmatrix} \tag{A.17}$$

Appendix B

Analytical Solution of Pore Pressure Buildup in Deep Soil

Take Laplace transformation of Eqn. 5.34 with respect to ξ:

$$L\left(P(\xi, y)\right) = Q(s, y) = \int_0^\infty e^{-s\xi} U(\xi, y) d\xi$$

then Eqn. 5.34 becomes

$$sQ = Q_{yy} + \frac{1}{s} y e^{-y} \tag{B.1}$$

with boundary/initial conditions

$$Q(s, y = 0) = 0 \quad \text{and} \quad Q(s, \infty) = 0$$

Eqn. B.1 is a second order quasi-linear ODE with boundary conditions specified at $y = 0$ and $y = \infty$. The solution of the equation is

$$Q(s, y) = R(s, y) + V(s, y) \tag{B.2}$$

where

$$R(s, y) = \frac{ys - y - s}{s(s-1)^2} e^{-y} \quad \text{and} \quad V(s, y) = \frac{2}{s(s-1)^2} e^{\sqrt{s}y}$$

Taking inverse Laplace transformation of each term in Eqn. B.2 will give the final solution of $P(y, \xi)$.

Inverse Lapalace Transformation of $R(s,y)$

It is easy to do inverse Laplace transformation of $R(s,y)$.

$$L^{-1}\left(R(s,y)\right) = \frac{1}{2\pi i}\int_{\gamma-i\infty}^{\gamma+i\infty}\frac{ys-y-2}{s(s-1)^2}e^{-y}e^{s\xi}ds \tag{B.3}$$

$R(s,y)$ has a simple pole at $s=0$ and a doulbe pole at $s=1$. So the integral can be evaluated using Cauchy's residue theorem. Fig. B.1 shows the contour in the s-plane and the two poles. By Cauchy's residue theorem,

$$\int_{C_1} R(s,y)e^{s\xi}ds + \int_{C_R} R(s,y)e^{s\xi}ds = 2\pi i \mathrm{Res}_{s=s_k} R(s,y)e^{s\xi} \quad k=1,2 \tag{B.4}$$

Using Jordan's lemma, when $R \to +\infty$, $\int_{C_R} R(s,y)e^{s\xi}ds \to 0$. So the only contribution comes from the residues. Now let $R \to +\infty$,

$$\begin{aligned} L^{-1}\left(R(s,y)\right) &= \frac{1}{2\pi i}\int_{\gamma-i\infty}^{\gamma+i\infty}\frac{ys-y-2}{s(s-1)^2}e^{-y}e^{s\xi}ds \\ &= \mathrm{Res}_{s=s_k} R(s,y)e^{s\xi} \quad k=1,2 \end{aligned}$$

The residues at the two poles are calculated as following. For $s=0$, it is a simple pole and the function can be written as

$$R(s,y)e^{s\xi} = \frac{\Phi(s,y)}{s} \quad \text{where} \quad \Phi(s,y) = e^{-y}\frac{e^{s\xi}}{(s-1)^2}(ys-y-s) \tag{B.5}$$

So

$$\mathrm{Res}_{s=0} R(s,y)e^{s\xi} = \Phi(0) = e^{-y}(-y-2) \tag{B.6}$$

For $s=1$, it is a double pole and the function can be written as

$$R(s,y)e^{s\xi} = \frac{\Phi(s,y)}{(s-1)^2} \quad \text{where} \quad \Phi(s,y) = e^{-y}\frac{e^{s\xi}}{s}(ys-y-s) \tag{B.7}$$

So

$$\begin{aligned} \text{Res}_{s=1} R(s,y)e^{s\xi} &= \frac{\Phi'(1)}{1!} && \text{(B.8)} \\ &= e^{-y}\frac{e^{s\xi}(2+y-2s\xi-sy\xi+s^2y\xi)}{s^2}|_{s=1} && \text{(B.9)} \\ &= e^{-y}e^{\xi}(2+y-2\xi) && \text{(B.10)} \end{aligned}$$

Combine the previous results, then

$$L^{-1}\left(R(s,y)\right) = e^{-y}\left[-2-y+e^{\xi}(2+y-2\xi)\right] \qquad \text{(B.11)}$$

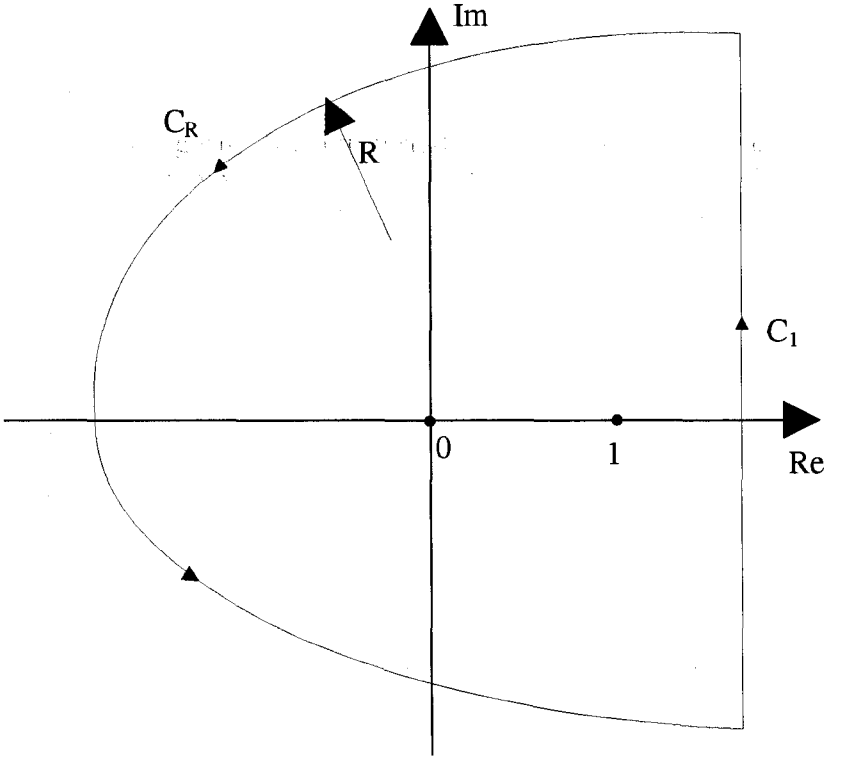

Figure B.1: Contour Integration Path around Two Poles for $R(s,y)$

Inverse Laplace Transformation of $V(s,y)$

The inverse Laplace transformation of V(s,y) is relatively complicated comparing to that of $R(s,y)$ since it involes the branch cut in the complex domain. $R(s,y)$ has a simple pole at $s=0$ and a double pole at $s=1$.It also needs to choose a branch cut for $\sqrt{s}$. For simplication, the branch cut is as the negative real axis. Fig. B.2 shows the contour and the branch cut.

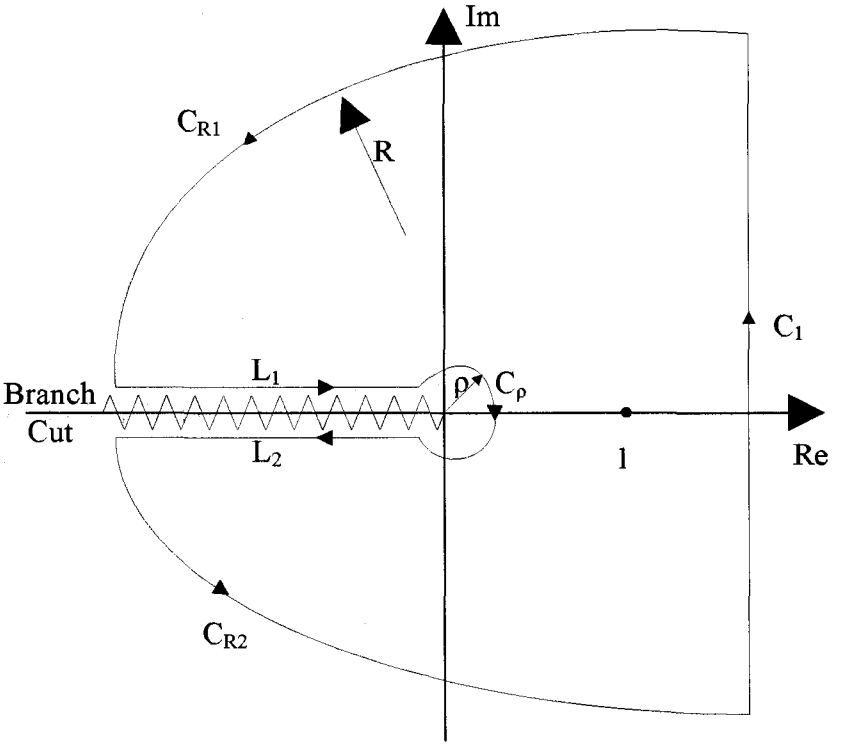

Figure B.2: Contour Integration Path around Two Poles and Branch Cut for $V(s,y)$

According to Cauchy's residue theorem, the contour integration becomes

$$\int_{C_1} + \int_{C_{R_1}} + \int_{L1} + \int_{C_\rho} + \int_{L_2} + \int_{C_{R_2}} = 2\pi i \mathrm{Res}_{s=s_k} R(s,y)e^{s\xi} \quad k=1,2 \tag{B.12}$$

Using Jordan's lemma, when $R \to +\infty$, $\int_{C_{R_1}} \to 0$ and $\int_{C_{R_2}} \to 0$. Now let's consider the paths of $L1$ and $L2$. On the complex plan, the complex number can be expressed as $s = re^{i\theta}$,

where r is the modulus and θ is the argument. Let

$$f(s,y) = V(s,y)e^{s\xi} = \frac{2}{s(s-1)^2}e^{s\xi-\sqrt{s}y} = \frac{2}{s(s-1)^2}e^{\left[\frac{1}{2}(\ln r+i\theta)\right]} \tag{B.13}$$

On $L1$, $\theta = \pi$, $s = re^{i\pi}$:

$$f(s,y) = \frac{2}{-r(r+1)^2}e^{-r\xi-i\sqrt{r}y} \tag{B.14}$$

On $L2$, $\theta = -\pi$, $s = re^{-i\pi}$:

$$f(s,y) = \frac{2}{-r(r+1)^2}e^{-r\xi+i\sqrt{r}y} \tag{B.15}$$

Then

$$\int_{L1} = \int_R^\rho -\frac{2}{r(r+1)^2}e^{-r\xi-i\sqrt{r}y}dr \tag{B.16}$$

$$= \int_\rho^R \frac{2}{r(r+1)^2}e^{-r\xi-i\sqrt{r}y}dr \tag{B.17}$$

$$= \int_\rho^R \frac{2}{r(r+1)^2}e^{-r\xi}\left[\cos\left(\sqrt{r}y\right) - i\sin\left(\sqrt{r}y\right)\right]dr \tag{B.18}$$

$$\int_{L2} = \int_\rho^R -\frac{2}{r(r+1)^2}e^{-r\xi+i\sqrt{r}y}dr \tag{B.19}$$

$$= \int_\rho^R -\frac{2}{r(r+1)^2}e^{-r\xi}\left[\cos\left(\sqrt{r}y\right) + i\sin\left(\sqrt{r}y\right)\right]dr \tag{B.20}$$

So, when $\rho \to 0$ and $R \to +\infty$

$$\int_{L1} + \int_{L2} = -4i\int_0^{+\infty} \frac{e^{-r\xi}}{r(r+1)^2}\sin\left(\sqrt{r}y\right)dr \tag{B.21}$$

and when $\rho \to 0$, the integration along the path C_ρ can also be evaluated using the Cauchy's residue theorem. The residue at $s = 0$ is calculated as following. The function $f(s)$ can be written

as

$$f(s) = \frac{\Phi(s)}{s} \quad \text{where} \quad \Phi(s) = \frac{2}{(s-1)^2} e^{s\xi - \sqrt{s}y} \tag{B.22}$$

So

$$\text{Res}_{s=0} = \Phi(0) = 2 \tag{B.23}$$

Then

$$\int_{C_\rho} = -2\pi i \text{Res}_{s=0} = -4\pi i \tag{B.24}$$

The residue at $s = 1$ is calculated as following. Since $s = 1$ is a double pole, the function $f(s)$ can be written as

$$f(s) = \frac{\Phi(s)}{(s-1)^2} \quad \text{where} \quad \Phi(s) = \frac{2}{s} e^{s\xi - \sqrt{s}y} \tag{B.25}$$

So

$$\text{Res}_{s=1} = \frac{\Phi'(1)}{1!} = -e^{-y+\xi}(2 + y - 2\xi) \tag{B.26}$$

Put all the terms together and after some manupilation, the inverse Laplace transformation of $V(s, y)$ can be written as

$$L^{-1}(V(s,y)) = 2 - e^{-y+\xi}(2 + y - 2\xi) - \frac{2}{\pi} \int_0^\infty \frac{e^{-r\xi}}{r(r+1)^2} \sin(\sqrt{r}y) dr \tag{B.27}$$

The final solution for $P(y, \xi)$ has the form

$$\begin{aligned} P(y,\xi) &= L^{-1}(R(s,y)) + L^{-1}(V(s,y)) & \text{(B.28)} \\ &= 2\left[1 - \left(\frac{y}{2} + 1\right) e^{-y} - \frac{1}{\pi} \int_0^\infty \frac{e^{-r\xi}}{r(r+1)^2} \sin\sqrt{r}y dr\right] & \text{(B.29)} \end{aligned}$$

which is the same as in Jeng et al. (2007). When time goes to infinity, the integral in equation 5.37 goes to zero since $e^{-r\xi}$ will be infinitesimally small. The final steady state solution is just the first part of equation 5.37 which is exactly the same as equation 5.36. The steady solution is plotted in Fig. B.3. The excessive pore pressure at the bed surface is always zero and the the excessive

pore pressure at infinite depth is 2.

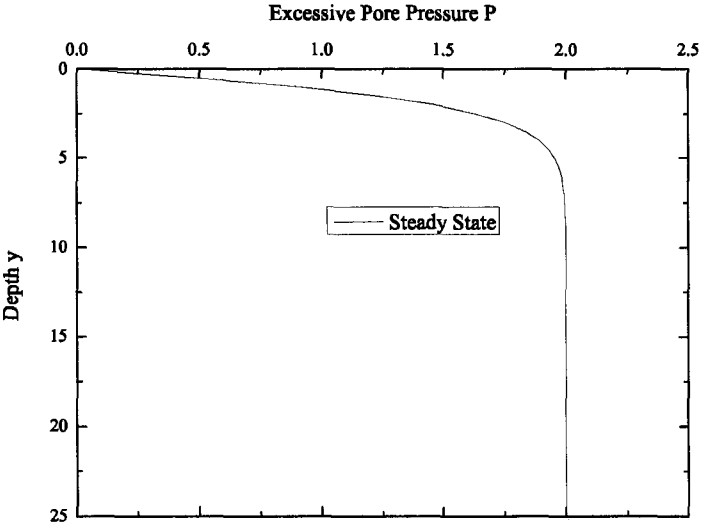

Figure B.3: Steady State Solution of the Excessive Pore Pressure for Deep Soil

References

A. Aliabadi, J. Abedi, B. Zellars, K. Bota, and A. Johnson. Simulation technique for wave generation. *Communications in Numerical Methods in Engineering*, 19:349–359, 2003.

K. Anastasiou and C. Chan. Solution of the 2d shallow water equations using the finite volume method on unstructured triangular meshes. *International Journal for Numerical Methods in Fluids*, 24:1225–1245, 1997.

E. Anderson, Z. Bai, C. Bischof, S. Blackford, J. Demmel, J. Dongarra, J. D. Croz, A. Greenbaum, S. Hammarling, A. McKenney, and D. Sorensen. *LAPACK User's Guide*. SIAM, Philadelphia, PA., 3 edition, 1999.

F. V. Beek and H. Wind. Numerical modeling of erosion and sedimentation around offshore pipelines. *Coastal Engineering*, 14:107–128, 1990.

R. Bennett and R. Dolan. Mine burial assessment. state of the art and science, technology, and modeling. Technical Report Technical Rep. No. SI-0099-05, Seaprobe, Inc., USA, 2001.

A. Bermudez and M. Vazquez. Upwind methods for hyperbolic conservtion laws with source terms. *Computers and Fluids*, 23(8):1049–1071, 1994.

M. Biot. General theory of three-dimensional consolidation. *Journal of Applied Physics*, 12(2): 155–164, 1941.

H. Breusers and A. Raudkivi. *Scouring*. IAHR Hydraulic Design Manual 2., A.A. Balkemn, Rotterdam, The Netherlands, 1991.

H. Breusers, G. Nicollet, and H. Shen. Local scour around cylindrical piers. *Journal of Hydraulic Research*, 15(3):211–252, 1977.

B. Brørs. Numerical modeling of flow and scour at pipelines. *Journal of Hydraulic Engineering*, 125(5):511–523, 1999.

Z. Cao, R. Day, and S. Egashira. Coupled and decoupled numerical modeling of flow and morphological evolution in alluvial rivers. *Journal of Hydrauic Engineering*, 128(3):306–321, 2002.

M. B. Cardenas and J. L. Wilson. Hydrodynamics of coupled flow above and below a sediment-water interface with triangular bedforms. *Advances in Water Resources*, 30:301–313, 2007.

Y. Cataño-Lopera. *Burial of Short Cylinders Induced by Local Scour and Bedform Migration Under Waves Plus Currents*. PhD thesis, University of Illinois at Urbana and Champaign, 2005.

A. Chan. User manual for diana-swandyne ii. Department of Civil Engineering, University of Birmingham, 1995.

S. S. Chatterjee and S. N. Ghosh. Submerged horizontal jet over erodible bed. *Journal of the Hydraulic Division*, 106(HY11):53–90, 1980.

S. S. Chatterjee, S. N. Ghosh, and M. Chatterjee. Local scour due to submerged horizontal jet. *Journal of Hydraulic Engineering*, 120(8):53–90, 1994.

L. Cheng, B. M. Sumer, and J. Fredsøe. Solutions of pore pressure buildup due to progressive waves. *International Journal of Numerical and Analytical Methods in Geomechanics*, 25(9): 885–907, 2001.

E. C. Clukey, F. H. Kulhawy, and P. L. F. Liu. *Laboratory and Field Investigation of Sediment Interaction*, pages 381–396. ASTM STP 883. American Society for Testing and Materials, Philadelphia, 1985.

Y. Cui and G. Parker. Linear analysis of coupled equations for sediment transport. In *Environmental and Coastal Hydraulics: Protecting the Aquatic Habitat - Proceedings of Theme B of the XXVII IAHR Congress*, pages 1256–1261, San Francisco, 1997.

Y. Cui, G. Parker, E. Thomas, E. James, and M. Annjanette. More on the evolution of bed material waves in alluvial rivers. *Earth Surface Processes and Landforms*, 30:107–114, 2005.

M. Darwish and F. Moukalled. Tvd schemes for unstructured grids. *International Journal of Heat and Mass Transfer*, 46:599–611, 2003.

P. De Alba, H. B. Seed, and C. K. Chan. Sand liquefaction in large-scale simple shear tests. *Journal of Geotechnical Division, ASCE*, 103:909–928, 1976.

R. G. Dean and R. A. Dalrymple. *Water Wave Mechanics For Engineers and Scientists*. World Scientific, 1991.

I. Demirdžić, S. Muzaferija, and M. Perić. Finite volume method for stress analysis in complex domains. *International Journal For Numerical Methods In Engineering*, 37:3751–3766, 1994.

I. Demirdžić, S. Muzaferija, and M. Perić. Benchmark solutions of some structural analysis problems using finite-volume method and multigrid acceleration. *International Journal For Numerical Methods In Engineering*, 40:1893–1908, 1997.

H. DeVriend. 2dh mathematical modeling of morphological evolutions in shallow water. *Coastal Engineering*, 11:1–27, 1987a.

H. DeVriend. Analysis of horizontally two-dimensional morphological evolutions in shallow water. *Journal of Geophysical Research*, 92(C4):3877–3893, 1987b.

S. Dey. Local scour at piers, part i: A review of development of research. *International Journal of Sediment Research*, 12(2):23–44, 1997.

J. Duan and S. Nanda. Two-dimensional depth-averaged model simulation of suspended sediment concentration distribution in a groyne field. *Journal of Hydrology*, 327:426–437, 2006.

B. Duc, T. Wenka, and W. Rodi. Numerical modeling of bed deformation in laboratory channel. *Journal of Hydraulic Engineering*, 130(9):894–904, 2004.

S. Dunn, P. Vun, A. Chan, and J. Damgaard. Numerical modeling of wave-induced liquefaction aournd pipelines. *Journal of Waterway, Port, Coastal, and Ocean Engineering*, 132(4):276–288, 2006.

F. Engelund and J. Fredsøe. A sediment transport model for straight alluvial channels. *Nordic Hydrology*, 7:293–306, 1976.

D. Farshi and S. Komaei. Discussion of "finite volume model for two-dimensional shallow water flows on unstructured grids". *Journal of Hydraulic Engineering*, 131(12):1147–1148, 2005.

M. Foda, J. Hunt, and H. Chou. A nonlinear model for the fluidization of marine mud by waves. *Journal of Geophysical Research*, 98(C4):7039–7047, 1993.

F. Gao, D. Jeng, and H. Sekiguchi. Numerical study on the interaction between non-linear wave, buried pipeline and non-homogeneous porous seabed. *Computers and Geotechincs*, 30:535–547, 2003.

M. H. García. *Sedimentation and Erosion Hydraulics*, chapter 6, Hydraulic Design Handbook. McGraw-Hill, Inc., 1999.

M. H. García and G. Parker. Entrainment of bed sediment into suspension. *Journal of Hydraulic Engineering*, 117(4):414–435, 1991.

B. Gatmiri. Response of cross-anisotropic seabed to ocean waves. *Journal of Geotechnical Engineering*, 118(9):1295–1314, 1992.

A. Grass. Sediment transport by waves and currents. Technical Report FL29, SERC London Center for Marine Technology, 1981.

M. T. Heath. *Scientific Computing: An Introductory Survey*. McGraw-Hill Companies, 1996.

C. W. Hirt and B. D. Nicholls. Volume of fluid (vof) method for dynamics of free boundaries. *Journal of Computational Physics*, 39(1):201–225, 1981.

J. Hudson and P. Sweby. Formulation for numericall approximating hyperbolic systems governing sediment transport. *Journal of Scientific Computing*, 19(1-3):225–252, 2003.

J. Hudson and P. Sweby. A high-resolution scheme for the equations governing 2d bed-load sediment transport. *International Journal for Numerical Methods in Fluids*, 47:1085–1091, 2005.

J. Hudson, J. Damgaard, N. Dodd, T. Chesher, and A. Cooper. Numerical approaches for 1d morphodynamic modelling. *Coastal Engineering*, 52:691–707, 2005.

R. I. Issa. Solution of the implicitly discretised fluid flow equations by operator-splitting. *Journal of Computational Physics*, 62(1):40–65, 1986.

H. Jasak. *Error Analysis and Estimation for the Finite Volume Method with Application to Fluid Flows*. PhD thesis, Imperial College of Science, Technology and Medicine, 1996.

H. Jasak and Z. Tuković. Automatic mesh motion for the unstructured finite volume method. *Transactions of FAMENA*, 30(6):1–18, 2007.

H. Jasak and H. Weller. Application of the finite volume method and unstructured meshes to linear elasticity. *International Journal For Numerical Methods In Engineering*, 48:267–287, 2000.

D. Jeng. Wave-indueced liquefaction potential at the tip of a breakwater: An analytical solution. *Applied Ocean Research*, 18:229–241, 1996.

D. Jeng. Soil response in cross-anisotropic seabed due to standing waves. *Journal of Geotechnical and Geoenvironmental Engineering*, 123(1):9–19, 1997.

D. Jeng and J. Hsu. Wave-indueced soil response in a nearly saturated sed-bed of finite thickness. *Géotechnique*, 46(3):427–440, 1996.

D. S. Jeng and Y. S. Lin. Wave-induced pore pressure around a buried pipeline in gibson soil: Finite element analysis. *International Journal for Numerical and Analytical Methods in Geomechanics*, 23:1559–1578, 1999.

D. S. Jeng and B. R. Seymour. Simplified analytical approximation for pore-water pressure buildup in marine sediments. *Journal of Waterway, Port, Coastal, and Ocean Engineering*, 133(4):309–312, 2007.

D. S. Jeng, B. R. Seymour, and J. Li. A new approximation for pore pressure accumulation in marine sediment due to water waves. *International Journal for Numerical and Analytical Methods in Geomechanics*, 31(1):53–69, 2007.

B. E. Lauder and D. B. Spalding. The numerical computation of turbulent flows. *Computer Methods in Applied Mechanics and Engineering*, 3(2):269–289, 1973.

R. LeVeque. Balancing source terms and flux gradients in high-resolution godunov methods: The quasi-steady wave-propagation algorithm. *Journal of Computational Physics*, 146:346–365, 1998.

R. W. Lewis and B. A. Schrefler. *The Finite Element Method in the Static and Dynamic Deformation and Consolidation of Porous Media*. John Wiley & Sons, second edition, 1998.

F. Li and L. Cheng. Prediction of lee-wake scouring of pipelines in currents. *Journal of Waterway, Port, Coastal, and Ocean Engineering*, 127(2):106–112, 2001.

D. Liang, L. Cheng, and F. Li. Numerical modeling of flow and scour below a pipeline in currents part ii. scour simulation. *Coastal Engineering*, 52(1):43–62, 2005.

X. Liu and M. García. Numerical simulation of local scour with free surface and automatic mesh deformation. In *Proceedings of World Environmental and Water Resource Congress*, Omaha, NE, 2006a.

X. Liu and M. García. Numerical simulation of sea bed response under waves with coupled solver of biot consolidation equations and free surface water flow. In *Proceedings of ISOPE PACOMS*, Dalian, China, 2006b.

X. Liu and M. García. Numerical investigation of seabed respone under waves with free-surface water flow. *International Journal of Offshore and Polar Engineering*, 17(2):97–104, 2007a.

X. Liu and M. García. Discussion of "divergence form for bed slope source term in shallow water equations" by a. valiani and l. begnudelli. *Journal of Hydraulic Engineering*, accepted, 2007b.

D. Lyn. Unsteady sediment-transport modeling. *Journal of Hydrauic Engineering*, 113(1):1–15, 1987.

D. Lyn and M. Altinakar. St. venant-exner equations for near-critical and transcritical flows. *Journal of Hydrauic Engineering*, 128(6):579–587, 2002.

O. Madsen. Wave-induced pore pressure and effective stresses in a porous bed. *Géotechnique*, 28 (4):377–393, 1978.

W. Magda. Wave-induced uplift force acting on a submarine buried pipeline: Finite element formulation and verification of computations. *Computers and Geotechincs*, 19(1):47–73, 1996.

S. Mayer and P. Madsen. Simulation of breaking waves in the surf zone using a navier-stokes slolver. In *International Conference in Coastal Engineering, Sydney*, 2000.

S. Mayer, A. Garapon, and L. S. Sorensen. A fractional step method for unsteady free-surface flow with application to non-linear wave dynamics. *International Journal For Numerical Methods in Fluids*, (28):293–315, 1998.

W. McDougal, Y. Tsai, and P.-F. Liu. Wave-induced pore water pressure accumulation in marine soils. *Journal of Offshore Mechanics and Arctic Engineering, ASME*, 111(1):1–11, 1989.

C. Mei and M. Foda. Wave-induced response in a fluid-filled poro-elastic solid with a free surface—a boundary layer theory. *Geophys. J. Roy. Astron. Soc.*, 66:597–631, 1981.

B. Melville. Pier and abutment scour: Integrated approach. *Journal of Hydraulic Engineering*, 123(2):125–136, 1997.

B. Melville and S. Coleman. *Bridge Scour*. Water Resources Publications, Fort Collins, Colorado, USA, 2000.

B. Melville and A. Sutherland. Design method for local scour at bridge piers. *Journal of Hydraulic Research*, 114(10):1210–1226, 1988.

T. Mioduszewski and S. Maeno. Experimental study of scouring process and flow behavior aournd a spur dike during the surge pass. In *Proceedings of the Thirteenth (2003) International Offshore and Polar Engineering Conference*, pages 858–863, Hnolulu, Hawaii, USA, May 2003. ISOPE.

A. Nayfeh. *Introduction to Perturbation Techniques*. John Wiley & Sons, 1981.

A. A. S. Neyshabouri, A. M. F. Da Silva, and R. Barron. Numerical simulation of scour by a free falling jet. *Journal of Hydraulic Research*, 41(5):533–539, 2003.

M. Nujić. Efficient implementation of non-oscillatory schemes for the computation of free-surface flows. *Jouranl of Hydraulic Research*, 33(1):101–111, 1995.

S. Okusa. Wave-induced stesses in unsaturated submarine sediments. *Géotechnique*, 35(4):517–532, 1985.

N. R. B. Olsen and M. C. Melaaen. Three-dimensional calculation of scour around cylinders. *Journal of Hydraulic Engineering*, 119(9):1048–1053, 1993.

N. R. B. Olsen and M. C. Melaaen. Three-dimensional numerical flow modeling for estimation of maximum local scour depth. *Journal of Hydraulic Research*, 36(9):579–590, 1999.

OpenCFD. Openfoam: The open source computational fluid dynamics (CFD) toolbox. http:://www.OpenFoam.org (Dec. 10, 2006), 2006.

G. Parker and M. H. García. *River, Coastal and Estuarine Morphodynamics: RCEM 2005*. Taylor & Francis Group, 2006.

S. V. Patankar. *Numerical Heat Transfer and Fluid Flow*. McGraw-Hill, 1981.

N. Rajaratnam. *Turbulent Jet*. Elsevier Scientific Publishing Company, 1976.

A. Raudkivi. Functional trends of scour at bridge piers. *Journal of Hydraulic Engineering*, 112 (1):1–13, 1986.

J. E. Richardson and V. G. Panchang. Three-dimensional simulation of scour-inducing flow at bridge piers. *Journal of Hydraulic Engineering*, 124(5):530–540, 1998.

W. Rodi. *Turbulence Models and Their Application in Hydraulics - A State of the Art Review*. International Association for Hydraulic Research, Delft, Balkema, 3 edition, 1993.

P. Roe. Approximate riemann solvers, parameter vectors and difference schemes. *Journal of Computational Physics*, 43:357–372, 1981.

P. Roe. Characteristic based schemes for the euler equations. *Ann. Rev. Fluid. Mech*, 18:337–365, 1986.

B. Rogers, M. Fujihara, and A. Borthwick. Adaptive q-tree godunov-type scheme for shallow water equations. *International Journal for Numerical Methods in Fluids*, 35:247–280, 2001.

B. Rogers, A. Borthwick, and P. Taylor. Mathematical balancing of flux gradient and source terms prior to using roe's approximate riemann solver. *Journal of Computational Physics*, 192:422–451, 2003.

A. Roulund, B. M. Sumer, J. Fredsøe, and J. Michelsen. Numerical and experimental investigation of flow and scour around a circular pile. *Journal of Fluid Mechanics*, 534:351–401, 2005.

T. Sakai, H. Gotoh, and T. Yamamoto. Block subsidence under pressure and flow. In *Proc. 24th Conference on Coastal Engineering (ICCE94)*, pages 23–28, Kobe, Japan, 1994.

H. Seed and J. Booker. Wave-induced pore pressure in relation to ocean floor stability of cohesionless soil. *Marine Geotechnology*, 3(2):123–150, 1978.

H. B. Seed. Evaluation of soil liquefaction effects on level ground during earthquake. In *Liquefaction Problems in Geotechnical Engineering*, pages 1–104. ASCE Annual Convention and Exposition, 1976.

H. B. Seed, P. O. Martin, and J. Lysmer. The generation and dissipation of pore water pressure during soil liquefaction. Technical Report Report EERC 75-26, College of Engineering, University of California, Berkeley, California, 1975.

J. A. Sethian. *Level Set Methods: Evolving Interfaces in Geometry, Fluid Mechanics, Computer Vision, and Material Science*. Cambridge Monographs on Applied and Computational Mathematics. Cambridge University Press, 1996.

J. D. Smith and S. McLean. Spatially averaged flow over a wavy surface. *Journal of Geophysical Research*, 83:1735–1746, 1977.

S.Soares-Frazão and Y. Zech. Dam break in channels with 90 ° bend. *Journal of Hydraulic Engineering*, 128(11):956–968, 2002.

B. M. Sumer and J. Fredsøe. Wave scour around a large verticle circular cylinder. *Journal of Waterway, Port, Coastal and Ocean Engineering*, 127(3):125–134, 2001.

B. M. Sumer and J. Fredsøe. *The Mechanics of Scour in the Marine Environment*. World Scientific Publishing, New Jersey,USA, 2002.

B. M. Sumer, J. Fredsøe, and N. Christiansen. Scour around a vertical pile in waves. *Journal of Waterway, Port, Coastal and Ocean Engineering*, 117(1):15–31, 1992.

B. M. Sumer, N. Christiansen, and J. Fredsøe. Influence of cross section on wave scour around piles. *Journal of Waterway, Port, Coastal and Ocean Engineering*, 119(5):477–495, 1993.

B. M. Sumer, J. Fredsøe, S. Christensen, and M. T. Lind. Sinking/floating of pipelines and other objects in liquefied soil under waves. *Coastal Engineering*, 38:53–90, 1999.

H. A. Taiebat. *Three Dimensional Liquefaction Analysis of Offshore Foundations*. PhD thesis, University of Sydney, 1999.

O. Ubbink and R. I. Issa. A method for capturing sharp fluid interfaces on arbitrary meshes. *Journal of Computatonal Physics*, 153:26–50, 1999.

A. Valiani and L. Begnudelli. Divergence form for bed slope source term in shallow water equations. *Journal of Hydraulic Engineering*, 132(7):652–665, 2006.

L. C. van Rijn. Sediment transport, part II: Suspended load transport. *Journal of Hydrualic Engineering*, 110(11):1613–1641, 1984.

H. G. Weller, G. Tabor, H. Jasak, and C. Fureby. A tensorial approach to computational continuum mechanics using object-oriented techniques. *Computers in Physics*, 12(6):620–631, 1998.

Wikipedia. Soil liquefaction — wikipedia, the free encyclopedia, 2007. `http://en.wikipedia.org/w/index.php?title=Soil_liquefaction&oldid=164144829` [Online; accessed 16-October-2007].

W. Wu. Depth-averaged two-dimensional numerical modeling of unsteady flow and nonuniform sediment transport in open channels. *Journal of Hydraulic Engineering*, 130(10):1013–1024, 2004.

T. Yamamoto. Wave-induced instability in seabed. In *Proc. ASCE Special Conference, Coastal Sediments '77*, volume 25, pages 898–913, Charleston, SC, 1977.

T. Yamamoto, H. Koning, H. Sellmeiher, and E. van Hijum. On the response of a poro-elastic bed to water waves. *Journal of Fluid Mechanics*, 87(1):193–206, 1978.

T. Yoon and S. Kang. Finite volume model for two-dimensional shallow water flows on unstructured grids. *Journal of Hydraulic Engineering*, 130(7):678–688, 2004.

M. Yuhi and H. Ishida. Simplified solutions for wave-induced response of anisotropic seabed. *Journal of Waterway, Port, Coastal, and Ocean Engineering*, 18(1):46–50, 2002.

J. Zhou, D. Causon, C. Mingham, and D. Ingram. The surface gradient method for the treatment of source term in the shallow-water equations. *Journal of Computational Physics*, 168:1–25, 2001.

J. Zhou, D. Causon, D. Ingram, and C. Mingham. Numerical solutions of the shallow water equations with discontinuous bed topograph. *International Journal for Numerical Methods in Fluids*, 38:769–788, 2002.

O. Zienkiewicz, A. Chan, M. Pastor, B. Schrefler, and T. Shiomi. *Computational Geomechanics with Special Reference to Earthquake Engineering*. Wiley, 1999.

Author's Biography

Xiaofeng Liu was born in the Jiangsu province of China in 1977. He graduated from Tsinghua University in 2000 with a bachelor's degree in hydraulic engineering. Then he enrolled the graduate school of Peking University, China, where he worked with Professor J.R. Ni on the problem of dyke break and flooding of the Yellow river. During the graduate study there, he receieved several awards incluing Guanghua and Wusi fellowships. He got his master of science degree with honor from Peking University in 2003. Since then, Xiaofeng moved to to Champaign, Illinois, to begin his Ph.D. study in the department of civil and environmental engineering. He worked with professor Marcelo H. García as a research assistant. His main work is to conduct numerical model development and simulations. Following the completion of his Ph.D., Xiaofeng will start to work as a postdoc in the Hydrosystems Lab, UIUC.